# ROLL CHARACTERISTICS AND SHAPE OPTIMIZATION OF THE FREE-TO-ROTATE TAIL-FINS ON A CANARD-CONTROLLED MISSILE

A THESIS SUBMITTED TO
THE GRADUATE SCHOOL OF NATURAL AND APPLIED SCIENCES
OF
MIDDLE EAST TECHNICAL UNIVERSITY

BY

ERHAN FEYZİOĞLU

IN PARTIAL FULFILLMENT OF THE REQUIREMENTS
FOR
THE DEGREE OF MASTER OF SCIENCE
IN
AEROSPACE ENGINEERING

OCTOBER 2014

Approval of the thesis

**ROLL CHARACTERISTICS AND SHAPE OPTIMIZATION OF THE FREE-TO-ROTATE TAIL-FINS ON A CANARD-CONTROLLED MISSILE**

submitted by **ERHAN FEYZİOĞLU** in partial fulfillment of the requirements for the degree of **Master of Science in Aerospace Engineering Department, Middle East Technical University** by**,**

Prof. Dr. Gülbin Dural _______________
Dean, Graduate School of **Natural and Applied Sciences**

Prof. Dr. Ozan Tekinalp _______________
Head of Department, **Aerospace Engineering**

Prof. Dr. İsmail Hakkı Tuncer _______________
Supervisor, **Aerospace Engineering Dept., METU**

**Examining Committee Members:**

Prof. Dr. Nafiz Alemdaroğlu _______________
Aerospace Engineering Dept., METU

Prof. Dr. İsmail Hakkı Tuncer _______________
Aerospace Engineering Dept., METU

Prof. Dr. Serkan Özgen _______________
Aerospace Engineering Dept., METU

Assoc. Prof. Dr. Sinan Eyi _______________
Aerospace Engineering Dept., METU

Emrah Gülay, M.Sc. _______________
Senior Engineer, ROKETSAN

**Date: 23/10/2014**

**I hereby declare that all the information in this document has been obtained and presented in accordance with academic rules and ethical conduct. I also declare that, as required by these rules and conduct, I have fully cited and referenced all material and results that are not original to this work**.

Name, Last name : Erhan FEYZİOĞLU

Signature :

# ABSTRACT

## ROLL CHARACTERISTICS AND SHAPE OPTIMIZATION OF THE FREE-TO-ROTATE TAIL-FINS ON A CANARD-CONTROLLED MISSILE

Feyzioğlu, Erhan
M.S., Department of Aerospace Engineering
Supervisor: Prof. Dr. İsmail Hakkı Tuncer

October 2014, 81 Pages

In this thesis, a numerical investigation of roll motion characteristics and planform optimization of free-to-rotate tail fins are performed. Steady and unsteady, asymmetric flows due to the aileron deflection in canard fins are computed by solving the Reynolds-Averaged Navier-Stokes (RANS) solutions with FLUENT. Instantaneous unsteady aerodynamic loads and the moment of inertia of the tail fins are used to evaluate the angular displacement of the tail fins. The rotary grid motion is then implemented by a User-Defined-Function (UDF) developed. The unsteady solution provides the roll motion history and the final steady roll rate of the free-to-rotate tail fins. The numerical methodology is first validated on two test cases for which the experimental data are available. A gradient based planform optimization is then performed on the free-to-rate tail fins in order to minimize the roll rate while not allowing any reduction in the total normal force. The gradient vector of the objective function and the line search along the gradient vector are performed by discrete evaluations. The optimum tail fin planform reduces the roll rate of the tail fins by about 6% and increases the normal force by about 4%.

Keywords: Induced Roll Moment, Free-To-Rotate Tail Fins, Canard-Controlled Missile, Tail Shape Optimization, Gradient Based Optimization

# ÖZ

## KANARD KONTROLLÜ FÜZEDE SERBEST DÖNEN KUYRUĞUN YUVARLANMA DÖNÜ KARAKTERİSTĞİ VE KUYRUĞUN ŞEKİL OPTİMİZASYONU

Feyzioğlu, Erhan
Yüksek Lisans, Havacılık ve Uzay Mühendisliği Bölümü
Tez Yöneticisi: Prof. Dr. İsmail Hakkı Tuncer

Ekim 2014, 81 Sayfa

Bu tezde, serbest dönen kuyruğun yuvarlanma dönü karakteristiği sayısal olarak incelenmiş ve kuyruğun şekil optimizasyonu yapılmıştır. Durağan ve zamana bağlı, kanard yuvarlanma sapma açılarından kaynaklanan simetrik olmayan akışın Reynolds-Averaged Navier-Stokes (RANS) denklemleri ile çözümleri FLUENT ile gerçekleştirilmiştir. Kuyruk yüzeylerinin yuvarlanma yönündeki açısal yer değiştirmesini hesaplamak için kuyruk yüzeylerine etki eden anlık aerodinamik yükler ve kuyrukların atalet momenti değeri kullanılmıştır. Kullanıcı-Tanımlı-Fonksiyon (UDF) geliştirilerek bu açısal yer değiştirme çözüm ağına uygulanmıştır. Serbest dönen kuyruğun zamana göre dönü hareketi ve sabit son dönü hızı zamana bağlı çözümler ile elde edilmiştir. Kullanılan sayısal yöntemler öncelikle denek taşı modelleri ile doğrulanmış ve var olan deney verileri ile kıyaslanmıştır. Toplam normal kuvvet değerinde azalma olmadan kuyrukların dönü hızlarını azaltmaya yönelik serbest dönen kuyruk için gradyan tabanlı şekil optimizasyonu yapılmıştır. Her bir optimizasyon adımı için amaç fonksiyonunun gradyan yönü ve bu yöndeki adım uzunluğu hesaplamaları ayrı ayrı yapılmıştır. Optimum kuyruk şekli yuvarlanma dönü hızını yaklaşık %6 azaltmış ve normal kuvveti yaklaşık %4 arttırmıştır.

Anahtar Kelimeler: İndirgenmiş Yuvarlanma Momenti, Serbest Dönen Kuyruk, Kanard Kontrollü Füze, Kuyruk Şekil Optimizasyonu, Gradyan Tabanlı Optimizasyon

*To My Family*

## ACKNOWLEDGEMENTS

I wish my deepest gratitude to my supervisor Prof. Dr. İsmail Hakkı Tuncer for his guidance, advice, criticism and encouragements throughout the thesis.

I also would like to thank my colleagues in Aerodynamics Division of ROKETSAN for all their help and support during the thesis.

I am very thankful to my wife Mrs. Zehragül Feyzioğlu, my mother Sevilcan Güler and my brother Mr. Ersin Feyzioğlu for their help and motivation. Without them this work would not be completed.

I want to express my best wishes to Mr. Batuhan Nasuhbeyoğlu, Mr. Mustafa Can, Mr. Oral Akman and Mr. İskender Kayabaşı for their friendship and support during this study.

**TABLE OF CONTENTS**

## LIST OF FIGURES

FIGURES

# LIST OF TABLES

TABLES

## LIST OF SYMBOLS

| | |
|---|---|
| Roll Angle of Tail Fins | $\theta$ |
| Roll Rate of Tail Fins | $\omega$ |
| Angle of Attack | $\alpha$ |
| Moment of Inertia | $I_{xx}$ |
| Axial Force Coefficient | $C_A$ |
| Normal Force Coefficient | $C_N$ |
| Pitch Moment Coefficient | $C_m$ |
| Roll Moment Coefficient | $C_m$ |

# CHAPTER 1

# INTRODUCTION

Canard-controlled missiles are commonly used by designers. These missiles have induced roll problem generated by the canard tip vortices. For years, the idea of free-to-rotate tail fins has been used by designers of missile as a solution to induced roll moment. NASA and its predecessor, NACA, tested a number of roll-control devices as part of their aerodynamic research program. Some tests were conducted with missile airframes having free-to-rotate tail fins, not only to stabilize the missile longitudinally but also eliminate unwanted induced rolling moments that were generated by the various roll controls under investigation. In this section, the induced roll phenomenon and its effects on canard-controlled missiles are introduced. Also the previous studies performed about the free-to-rotate tail fins are mentioned.

## 1.1 Canard-Controlled Missile

Canard fins are attractive candidates for aerodynamic control of guided missiles for several reasons. For aerodynamic designers, canard effectiveness increases with increasing angle-of-attack. Hinge moment of canard fins is generally smaller than the hinge moment of the tail fins since canard fins have usually smaller chord length. Moreover, transonic stability is reduced by using canard fins. For system designers, canard fins are placed near the inertial measurement unit (IMU) and flight computer in order to eliminate the need to route cables to rear of the airframe. There is no need to package the control systems around the motor part.

Since the canard induced vortices impinging on both the body and the tail fins, the aerodynamic characteristics of the canard-body-tail (CBT) configuration are complicated. These vortices are beneficial when performing an in-plane pitch maneuver. The vortices from the canard fins are represented in Figure 1-1.

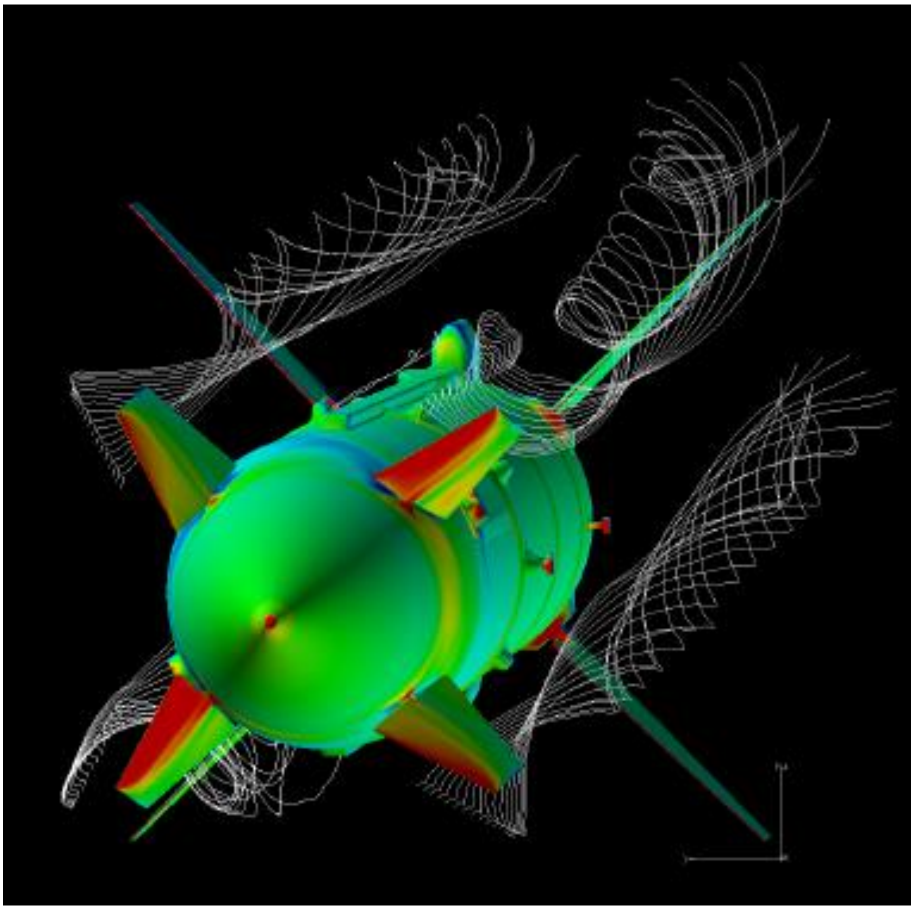

Figure 1-1 Canard Roll Coupling [1]

However, these vortices can induce roll coupling during roll and yaw maneuver. This situation stems from the circulation generated by the canard fins at incidence to the freestream. This phenomenon is called as induced roll [2]. The representation of this phenomenon is shown in Figure 1-2 for aileron deflection, and is shown in Figure 1-3 for rudder deflection of canard fins.

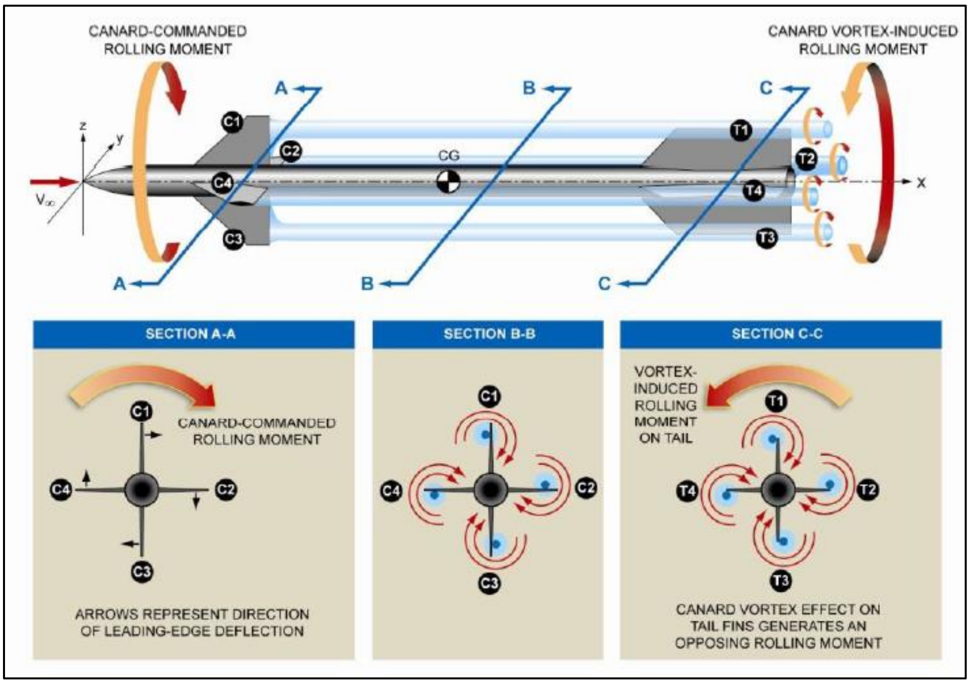


Figure 1-2 Canard Roll Coupling [3]

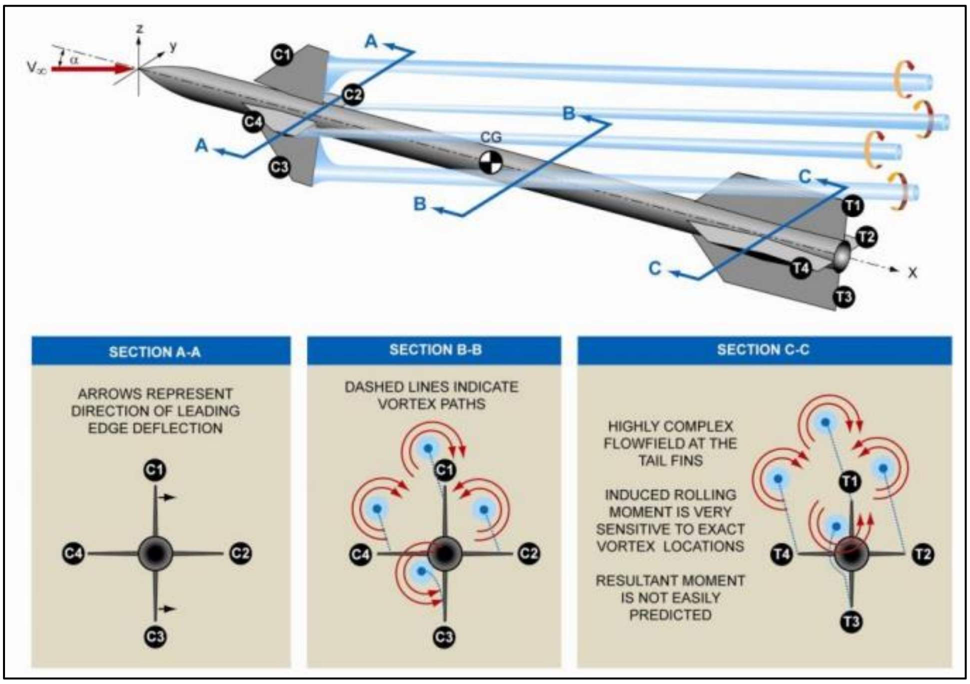


Figure 1-3 Canard Yaw Coupling [3]

The main solution to this phenomenon is to use free-to-rotate system for tail fins.

## 1.2 Free-To-Rotate Tail Fins

The most effective method for decoupling the canard fins and tail fins is the introduction of a bearing that will allow the tail fins to spin freely under the influence of the aerodynamic forces [2]. An example of missile having free-to-rotate tail fins is shown in Figure 1-4.

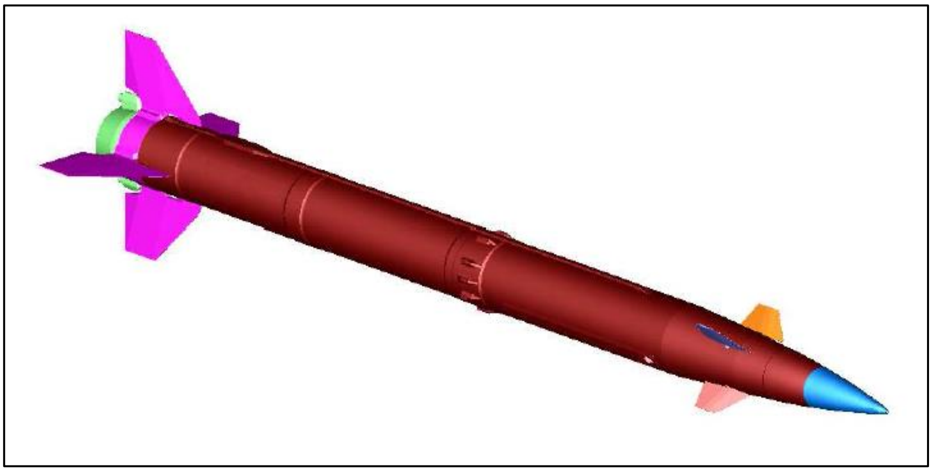

Figure 1-4 Example of a Missile with Free-To-Rotate Tail Fins [1]

## 1.3 Literature Survey

The canard controlled missiles have been preferred by missile aerodynamic designers. However, there occurs roll control problem that should be deal with while designing a canard controlled missile with tail fins. One of the solutions to this phenomenon is to use free-to-rotate tail fins. There are many experimental and numerical studies about airframes having free-to-rotate tail fins from 1950s to today.

The first studies about the induced roll problem were performed by the experimental tools since the Computational Fluid Dynamics (CFD) tools for these years were challenging due to the unsteadiness of the problem. Blair [4] was investigated both fixed and free-to-rotate tail fins on canard controlled missile by experiment. By this study, it was concluded that the lift-curve-slope of both fixed and free-to-rotate configurations were same and at low angles of attacks both configurations had same longitudinal stability level. For the free-to-rotate tail configuration at low angles of attacks, conventional roll control was provided with no-control reversal and induced roll due to yaw control and model roll angle was reduced.

In 1983, Blair and their colleagues [5] studied about the effect of the tail-fin span on roll characteristics of a canard-controlled missile by experiment. According to this study, the canard fins were effective roll-control devices throughout the test Mach numbers (1.6 to 3.5), model angles-of-attack (-4° to 18°) and model roll-angles (0° and 26.57°) for the reduced tail-span configurations. Increasing the tail fin span resulted in a reduction of canard roll control at low angles of attack. Induced rolling moment was created in the opposite direction to those created by the canard fins since the complex flow fields created by the deflected canard fins pass very close to the tail fins. For the tail fins having span longer than span of canard fins, the induced roll was large enough to counteract the canard roll. This produced negligible total model rolling moment, or rolling moment which was opposite to the desired (roll reversal). However, at the higher angles of attack, roll control was increased by increasing tail fins span.

Blair [6] studied the tail brake torque for free-to-rotate tail-fins in 1985. The electronic/electromagnetic brake system provided arbitrary tail-fin brake torques with continuous measurements of tail-to-mainframe torque and tail roll rate. The free-to-rotate tail afterbody was mounted on a set of low-friction ball bearings and was coupled to an electromagnet by a free-floating torque brake disc, which made up part of the magnetic path. The low-cost bearings with some friction could allow satisfactory aerodynamic stability and control characteristics while reducing adverse induced roll effects and maintaining low tail fin roll rates. For the free-to-rotate tail configuration, the induced rolling moment coefficient due to canard yaw control increased and the canard roll control decreased with increases in brake torque, which simulated bearing friction torque.

With the data obtained by experimental studies, aerodynamic fast prediction tools were commonly used for unsteady problems. Lesieutre and his colleagues [7] was aimed at investigating free-to-rotate tail fin configurations using both engineering-level and intermediate-level aerodynamic prediction codes. In the paper, the rolling tail characteristics were estimated based on static characteristics and calculated roll damping characteristics. In this investigation, the codes were used to estimate the static roll characteristics of the tail section under the influence of asymmetric canard vortices arising from roll and yaw control deflections; estimate the roll damping characteristics of the tail section as a function of angle of attack, and estimates the roll rate of the free-to-rotate tail section as a function of angle of attack. The rolling moment was difficult to predict because it was dominated by the canard and body shed vortices influencing the tail fins. This was the classical induced roll effect seen on canard-controlled missiles. For these configurations, the induced tail fin rolling moment opposed the direct canard control and actually caused the overall rolling moment to oppose the intent of the canard deflection. In general, the predicted aerodynamic characteristics were in good to excellent agreement with the experimental data and provided insight into understanding the nonlinear characteristics of missiles with free-to-rotate tail sections.

With increasing computer power, the unsteady problems started to be solved by CFD methods. Murman and Aftosmis [8] detailed the missile geometry under consideration, important features of the computational mesh, and the numerical method used for the simulations. The numerical investigations first concentrated on the flow field at an angle of attack of 4°, where the canard/tail interactions were strongest, and the spin rate of the tail was expected to be highest. Steady-state simulations of the missile with the fins fixed at various azimuths around the missile axis established a zero-spin-rate baseline. Dynamic simulations were then performed with an imposed spin rate on the tail. An iterative process was used to determine the spin rate which predicted a zero spin-averaged torque on the tail. These fixed spin rate simulations were compared with free-to-spin simulations obtained using a coupled CFD/6-Degre-of-Fredom (6-DOF) approach. Since the flow conditions in the work were supersonic (M = 1.6), the geometry upstream of the tail section was static, and the tail section had horizontal and vertical symmetry, the flow field within the tail section was periodic every 90° of spin. This periodicity was confirmed by the initial dynamic simulations. As such, it was only necessary to simulate the motion of the tail section through 90 °of rotation (after the initial transient). The trends of the spinning tail section with angle of attack variation were examined by simulating angles of attack of 0° and 12°, both with the tail held fixed and spinning. The rotation rate of the tail section was not known a priori. In order to determine the "natural" roll rate of the tail section, the rate at which the spin averaged rolling moment on the tail was zero, an iterative process is used. First, it was assumed that the tail rotation rate was low enough that the variation of spin-averaged tail rolling moment with rotation rate was linear. A fixed rotation rate was then imposed on the tail, which was intended to be a reasonable guess. The resulting spin-averaged tail rolling moment from this simulation were then fit with a straight line to determine the predicted natural roll rate of the tail section. A second dynamic simulation was then performed at the natural roll rate in order to confirm the prediction. The simulation with the natural rotation rate provided nearly zero spin-averaged tail rolling moment. As the canard vortices, canard downwash, and wind vector did not change when the tail spins, the variation of tail rolling moment with rotation angle was similar for all simulations, however shifted as the rotation rate was increasing. This implied that the rotation of the tail section provided minor dynamic effects, and these effects wash downstream without influencing the aerodynamic loads. This was especially true with a fixed spin rate as there was no acceleration of the tail section. When the velocity of the tail section balanced the outer flow effects, a stable spin rate was found. Since the variation in tail rolling moment is self-similar with fixed spin rates, it was unnecessary to compute the entire cycle at the initial guess. Once the increment between the static and initial guess is known, i.e. after the transient portion of the cycle had been computed, this increment could simply be applied to the static spin-average to obtain the spin-average at the initial guess. The forced-spin tail was an approximation to the actual rotation of the tail section. The actual motion would respond to the aerodynamic forces as it spun and increase or decrease the spin-rate accordingly. In order to assess the efficiency and accuracy of the forced-spin approximation, simulations with a free-to-spin tail were performed using the coupled CFD / 6-DOF method. The 6-DOF motion was constrained to only allow rotation about the longitudinal axis of the missile body, effectively limiting this to a 1-DOF simulation. In order to make performance predictions, the spin-averaged forces and moments of the dynamic configuration were required. While one static configuration did closely predict the dynamic spin averaged loads, this was fortuitous, and different canard settings or flow conditions would behave differently. The dynamic curves were shifted up and to the right from the static curve, and maintain the shape basic shape. This self-similarity was due to the lack of dynamic effects. The tail provided a “restoring” moment opposite to the effect the canards provide ahead of the center of mass. When the tail was free to spin, this restoring moment was reduced as the tail moves in response to the aerodynamic forces. From this point of view, the free-spinning tail behaved as if it was an equivalent static tail of smaller size. Hence the increment between the static and dynamic simulations was in the direction the canards were forcing the body to rotate, in this case nose up and starboard. This large variation in tail spin rate was caused by the torque being applied over longer time duration at this lower spin rate, and indicated that a forced-spin simulation at a fixed rate was not a good approximation for the actual motion at this angle of attack if the tail was spinning. Note that even though the static results indicated a statically-stable tail orientation, the mean tail rotation rate still increased. The large variation in tail spin rate implied that the simulation contained large dynamic effects.

Nygard [1] studied the work to demonstrate the utility of Chimera overset grid methods for missiles with freely spinning tailfins. The results showed that each force as a function of roll angle was not very sensitive to rotational speed. This applied to the rest of the forces and moments as well, except for the rolling moment. So if the approximate roll-rate was known, this fixed roll-rate would give results with acceptable accuracy. If the static computations were used to approximate time-averaged results, several cases with the tailfins fixed at different roll-angles should be averaged. The computed results were in fair agreement with experiments, but there was currently one unresolved significant difference in direction for the total force vectors. The Chimera overset gird method had been successfully applied to a geometrically complex missile with freely spinning tailfins.

## 1.4 Aim of the Thesis

Aim of the thesis is to assess roll characteristics of the free-to-rotate tail fins on a canard-control missile by RANS solutions with FLUENT and optimize the planform of the tail fins in order to minimize roll rate of the free-to-rotate tail fins by gradient based method. This provides better roll control characteristics on the missile. The aim at lowering the roll rate of the free-to-rotate tail fins is to obtained lower roll rate on the forebody of the missile. Lower roll rate of the forebody is a requirement for the control and guidance system operations. The torque transmitted to the forebody is proportional to the roll rate of the free-to-rotate tail fins. Therefore, the roll rate of the forebody of the missile is decreased if the roll rate of the free-to-rotate tail fins is decreased.

FLUENT is used in order to solve steady and unsteady RANS equations. Grids are generated by GAMBIT and TGRID. The method is validated with the test case models, which are Tandem-Control-Missile (TCM) and Modified-Tandem-Control Missile (M-TCM). The results are compared with experimental data. With the validated numerical methods gradient based optimization of the planform of the free-to-rotate tail fins is performed.

# CHAPTER 2

# METHODOLOGY

In this chapter, governing equations for RANS solutions and gradient based optimization method with line search algorithm will be introduced. Turbulence models used in this study will be discussed. Method of gradient based steepest descent optimization will be mentioned. Moreover, the line search algorithm will be explained. Objective function used in optimization process will be defined as a function of normal force and roll rate of the free-to-rotate tail fins. Finally, flow chart of this study is represented.

## 2.1 Solution of Reynolds-Averaged Navier-Stokes (RANS) Equations

High computer power and time are required to solve Navier-Stokes equations. Recent computer technology is inadequate to solve complex Navier-Stokes equations. Therefore, it is necessary to use simplified Navier-Stokes equations. Thus, Reynolds-Averaged Navier-Stokes equations, which take into account the viscous effects in a simpler way, are used in the numerical simulations. The simulations are performed using FLUENT. Equations used in RANS solutions are represented [9].

The conservation of mass, or continuity, equation is given as

$$\frac{\partial \rho}{\partial t} + \frac{\partial}{\partial x_i}(\rho \cdot u_i) = 0 \tag{2.1}$$

The conservation of momentum equations are given as

$$\frac{\partial}{\partial t}(\rho u_i) + u_j \frac{\partial}{\partial x_j}(\rho u_i) = -\frac{\partial p}{\partial x_i} + \frac{\partial}{\partial x_j}\tau_{ij} + \rho g_i \quad (2.2)$$

The stress tensor, $\tau_{ij}$, is given as

$$\tau_{ij} = \mu\left(\frac{\partial u_i}{\partial x_j} + \frac{\partial u_j}{\partial x_{ji}}\right) + \delta_{ij}\,\lambda\,\nabla\cdot\vec{v} \quad (2.3)$$

Dynamic viscosity term $\mu$ is calculated by using Sutherland's law in order to take into account the effect of temperature on dynamic viscosity. The equation is

$$\mu = \frac{1.45T^{\frac{3}{4}}}{T+110}10^{-6} \quad (2.4)$$

The equation of thermal energy is given as

$$\frac{\partial(\rho h)}{\partial t} + \frac{\partial}{\partial x_i}(\rho h u_i) = \frac{\partial}{\partial x_i}(k\frac{\partial T}{\partial x_i}) + S \quad (2.5)$$

In order to equalize the number of unknowns to the number of equations, the equation of state is stated is used by assuming air is an ideal gas. The equation of state is

$$p = \rho RT \quad (2.6)$$

Stagnation state properties should also be calculated in order to characterize the compressible flow. For constant heat capacity, the equations are used

$$\frac{P_o}{P} = \left(1 + \frac{\gamma - 1}{2} M^2\right)^{\gamma/(\gamma-1)} \tag{2.7}$$

$$\frac{T_o}{T} = 1 + \frac{\gamma - 1}{2} M^2 \tag{2.8}$$

## 2.2 Turbulence Modeling

Turbulent flows are much more irregular and intermittent in contrast with laminar flow, and turbulence typically develops as instability of laminar flow. For a real fluid, these instabilities result from the interactions of the non-linear inertial terms and the viscous terms contained in the Navier-Stokes equations, which are very complex since turbulence is rotational, three-dimensional, and time-dependent [10].

A turbulence model is defined as a set of equations (algebraic or differential) which determine the turbulent transport terms in the mean flow equations and thus close the system of equations. Turbulence models are based on hypotheses about the turbulent processes and require empirical input in the form of model constants or functions; they do not simulate the details of the turbulent motion, but only the effect of turbulence on the mean flow behavior.

Since all turbulent flows are transient and three-dimensional, the engineer is generally forced to develop methods for averaged quantities to extract any useful information. The most popular method for dealing with turbulent flows is Reynolds averaging which provides information about the overall mean flow properties. The main idea behind Reynolds time-averaging is to express any variable, $\theta(x,t)$, which is a function of time and space, as the sum of a mean and a fluctuating component as given by

$$\emptyset(x,t) = \overline{\emptyset(x,t)} + \emptyset'(x,t) \tag{2.9}$$

### 2.2.1 Spalart-Allmaras Turbulence Model

The Spalart-Allmaras model is a relatively simple one-equation model that solves a modeled transport equation for the kinematic eddy (turbulent) viscosity. This embodies a relatively new class of one-equation models in which it is not necessary to calculate a length scale related to the local shear layer thickness. The Spalart-Allmaras model was designed specifically for aerospace applications involving wall-bounded flows and has been shown to give good results for boundary layers subjected to adverse pressure gradients. It is also gaining popularity for turbomachinery applications [9].

### 2.2.2 Realizable k-ε Turbulence Model

The realizable k-ε model is a relatively recent development and differs from the standard k-ε model in two important ways:

1) The realizable k-ε model contains a new formulation for the turbulent viscosity.

2) A new transport equation for the dissipation rate, ε, has been derived from an exact equation for the transport of the mean-square vorticity fluctuation.

The term "realizable" means that the model satisfies certain mathematical constraints on the Reynolds stresses, consistent with the physics of turbulent flows. Neither the standard k-ε model nor the RNG k-ε model is realizable.

An immediate benefit of the realizable k-ε model is that it more accurately predicts the spreading rate of both planar and round jets. It is also likely to provide superior performance for flows involving rotation, boundary layers under strong adverse pressure gradients, separation, and recirculation [9].

### 2.2.3 Shear-Stress Transport (SST) k-ω Turbulence Model

The shear-stress transport (SST) k-ω model was developed by Menter to effectively blend the robust and accurate formulation of the k-ω model in the near-wall region with the free-stream independence of the k-ε model in the far field. To achieve this, the k-ε model is converted into a k-ω formulation. The SST k-ω model is similar to the standard k-ω model, but includes the following refinements:

1) The standard k-ω model and the transformed k-ε model are both multiplied by a blending function and both models are added together. The blending function is designed to be one in the near-wall region, which activates the standard k-ω model, and zero away from the surface, which activates the transformed k-ε model.

2) The SST model incorporates a damped cross-diffusion derivative term in the ω equation.

3) The definition of the turbulent viscosity is modified to account for the transport of the turbulent shear stress.

4) The modeling constants are different.

These features make the SST k-ω model more accurate and reliable for a wider class of flows (e.g., adverse pressure gradient flows, airfoils, transonic shock waves) than the standard k-ω model. Other modifications include the addition of a cross-diffusion term in the ω equation and a blending function to ensure that the model equations behave appropriately in both the near-wall and far-field zones [9].

## 2.3 Optimization Method

The optimization method for minimizing the roll rate of the tail fins is the gradient based steepest descent method with line search algorithm [11]. Gradient based and stochastic methods are both used in literature for design problems. Although gradient based methods do not guarantee to find the global optimum, for the unsteady analyses, which take a lot of time to solve, gradient based methods are quite successful if optimization is started with a logical initial point. The gradient based steepest descent algorithm and line search algorithm are represented in this part.

### 2.3.1 Gradient Based Steepest Descent Algorithm

The optimization problem is to minimize the objective function, $f(x)$, which is differentiable. If $x = \bar{x}$ is a given point, $f(x)$ can be approximated by its linear expansion,

$$f(\bar{x} + d) \approx f(\bar{x}) + \nabla f(\bar{x})^T d \tag{2.10}$$

if $d$ is small, i.e., if $\|d\|$ is small. If the approximation in the above expression is good, it is wanted to choose $d$ so that the inner product $\nabla f(\bar{x})^T d$ is as small as possible. Let us normalize $d$ so that $\|d\|$ = 1. Then among all directions $d$ with norm $\|d\|$ = 1, the direction

$$\bar{d} = \frac{-\nabla \mathrm{f}(\bar{x})}{\|\nabla \mathrm{f}(\bar{x})\|} \tag{2.11}$$

makes the smallest inner product with the gradient $\nabla \mathrm{f}(\bar{x})$. This fact follows from the following inequalities:

$$\nabla f(\bar{x})^T d \geq -\|\nabla \mathrm{f}(\bar{x})\| \|d\| = \nabla f(\bar{x})^T \left( \frac{-\nabla \mathrm{f}(\bar{x})}{\|\nabla \mathrm{f}(\bar{x})\|} \right) = \nabla f(\bar{x})^T \bar{d} \tag{2.12}$$

from this reason the un-normalized direction:

$$\bar{d} = -\nabla \mathrm{f}(\bar{x}) \tag{2.13}$$

is called the direction of steepest descent at the point $-\nabla \mathrm{f}(\bar{x})$.

### 2.3.2 Line Search Algorithm

Suppose that $f(x)$ is a continuous differentiable convex function, and that is wanted to solve:

$$\bar{\alpha} := \arg\min_{\alpha} f(\bar{x} + \alpha \bar{d}) \tag{2.14}$$

where $\bar{x}$ is current iterate, and $\bar{d}$ is the current direction generated by an algorithm that seeks to minimize $f(x)$. Suppose further that $\bar{d}$ is a descent direction of $f(x)$ at$x = \bar{x}$, namely:

$$f(\bar{x} + \epsilon\bar{d}) < \mathrm{f}(\bar{x}) \tag{2.15}$$

for all $\epsilon > 0$ and sufficiently small. Let

$$h(\alpha) := f(\bar{x} + \alpha\bar{d}), \tag{2.16}$$

where $h(\alpha)$ is a convex function in the scalar variable $\alpha$, and the problem is to solve for

$$\bar{\alpha} := \arg\min_{\alpha} h(\,\alpha)\,. \tag{2.17}$$

Therefore a value $\bar{\alpha}$ is sought for which

$$h'(\bar{\alpha}) = 0. \tag{2.18}$$

## 2.4 Free-To-Rotate Tail Fins Performance Parameters

Free-to-rotate tail fin performance parameters, which are roll angle and roll rate, mainly determine the performance of free-to-rotate tail fins. Roll angle and roll rate of the free-to-rotate tail fins give us the roll motion history of the tail fins.

### 2.4.1 Roll Angle of Tail Fins

Roll angle of the tail fins, $\theta_{tail}$, is the angle between the tail fins and vertical axis when viewed from back. Roll angle defines the path of the roll motion of tail fins for 1-DOF unsteady solutions. One revolution of the tail fins corresponds to 360° of roll angle. For the numerical solutions the roll angle at a given time is the integral of discretized displacements from initial time value to this time.

### 2.4.2 Roll Rate of Tail Fins

Roll rate of the tail fins, $\omega_{tail}$, is the time derivative of the roll angle of the tail fins in 1-DOF unsteady solutions.

$$\omega_{tail} = \dot{\theta}_{tail} \tag{2.19}$$

## 2.5 Geometric Parameters

In this part, the geometric parameters used in the optimization process are mentioned. Throughout the optimization process the geometric parameters are modified according to the gradient vector direction obtained by the disturbance on these parameters. Moreover, moment of inertia value, which determines the damping characteristics of the free-to-rotate tail, changes according to the change in the geometric parameters of the tail planform.

### 2.5.1 Planform of Tail Fins

The geometric parameters of the tail fins are leading edge sweep angle ($\Lambda_{LE}$), trailing edge sweep angle ($\Lambda_{TE}$), tip chord length ($c_{tip}$), root chord length ($c_{root}$), span length (b), wedge angles and thickness of profile. Among these parameters three parameters, which are leading edge sweep angle, tip chord length and span length, are used for the optimization process. By changing these three parameters trailing edge sweep angle automatically changes. This means that trailing edge sweep angle is a free parameter. Root chord length, wedge angles and thickness of profile are set to be constant. The representative planform shape of the tail fin and parameters used in optimization process are shown in Figure 2-1.

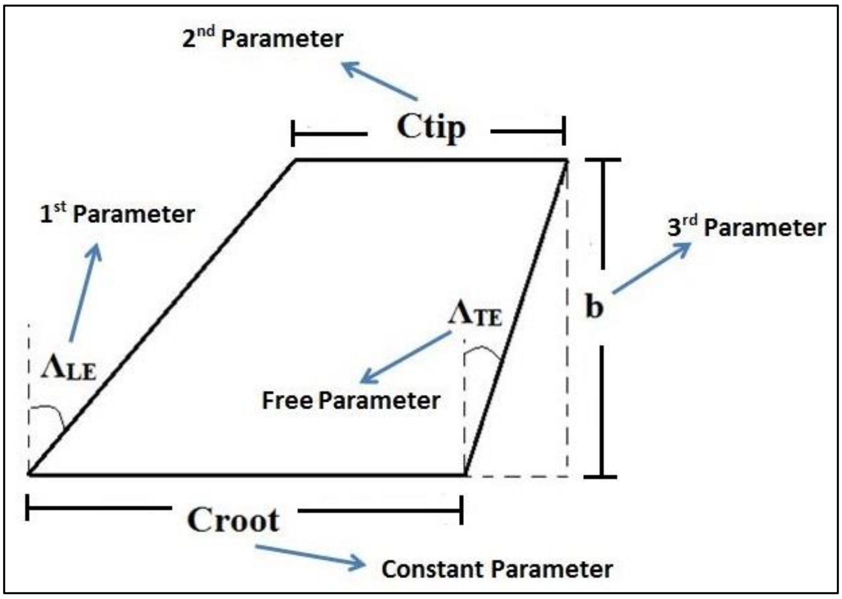

Figure 2-1 Planform shape of the tail fins and Parameters

In order to compare the geometric parameters with each other, the parameters are set to values between 0 and 1 by assuming logical limits for these parameters.

The sweep angle at leading edge ($\Lambda_{LE}$) is assumed a value between 0° and 30° and the value is non-dimensionalized by dividing to 30°. The span of the tail fin (b) and the tip chord of the tail fin are assumed to be a value smaller than 100 mm and these two parameters, $\Lambda_{LE}$ and b, are non-dimensionalized by dividing to 100 mm.

### 2.5.2 Moment of Inertia of Tail Fins

Moment of inertia is the one of the most effective parameter for the roll characteristics of the free-to-rotate tail fins. The parameter determines the displacement in roll direction under the moment in roll direction. The relation can be expressed as,

$$M_x = I_{xx} * \ddot{\theta} \tag{2.20}$$

where $M_x$ is the moment in roll direction, $I_{xx}$ is the moment of inertia, and $\ddot{\theta}$ is the derivative of roll rate.

$$I_{xx} = \int r^2 dm \tag{2.21}$$

where r is the radial distance to the axis of rotation and m is the mass.

The moment of inertia values of the tail fin geometries are obtained by SolidWorks program [12].

The moment of inertia is dependent on the material and there is no information about the material in the experiment report for the test case models. However, mainly two materials are used in wind tunnel testing, which are steel and aluminum. Aluminum is mainly preferred for the fuselage of the missile and also for the fins for subsonic testing. Since the forces on the fins in supersonic testing are very high, steel is generally preferred by the wind tunnel testers [13].

## 2.6 Objective Function

Objective function, which is aimed to be minimized in the optimization process, represents mainly the roll rate of the tail fins and the change in normal force on the missile surfaces. The purpose is to minimize the roll rate of the tail fins with no dramatic change in normal force.

In general objective function is calculated by weighted sum of multiple objectives;

$$f(\vec{X}) = \sum_{i=1}^{n} w_i . f_i(\vec{X}) \tag{2.22}$$

where $\vec{X}$ is the variable vector, $w_i$ is the weight factor of the objective $i$. There are two objectives used in this study. These are roll rate of the free-to-rotate tail fins and percentage of the change in normal force coefficient. The objective function is,

$$f(\omega_{tail}\,, \Delta\, C_N) = \frac{1}{2}\left( \frac{\omega_{tail}}{1\ 000} + \begin{cases} \dfrac{\Delta\, C_N(\ \%)}{10\ 000} & if\ \Delta\, C_N(\%) > 3 \\ \dfrac{\Delta\, C_N(\%)}{1\ 000} & if\ \ \Delta\, C_N(\%) < -1 \\ 0 & otherwise \end{cases} \right) \tag{2.23}$$

The roll rate value of the tail fins is divided by 1000 in order to obtain a value between 0 and 1 by assuming the roll rate value is lower than 1000. And this value is weighted by 0.5 in the objective function. The percentage of change in the normal force coefficient is powered by 4, and then divided by 10 000 if the normal force decreases and divided by 1 000 if the normal force increases. This is due to give more restriction to decrease in normal force coefficient. And this value is weighted by 0.5 in the objective function. The objective value as a function of change in normal force coefficient and the corresponding roll rate to this objective value are represented in Figure 2-2. It can be seen in the figure that the decrease in $C_N$ by 5% can be tolerated by decrease in roll rate by 600 rpm in order to obtain same objective value. On the other hand, the increase in $C_N$ by approximately 9% can be tolerated by decrease in roll rate by 600 rpm in order to obtain same objective value.

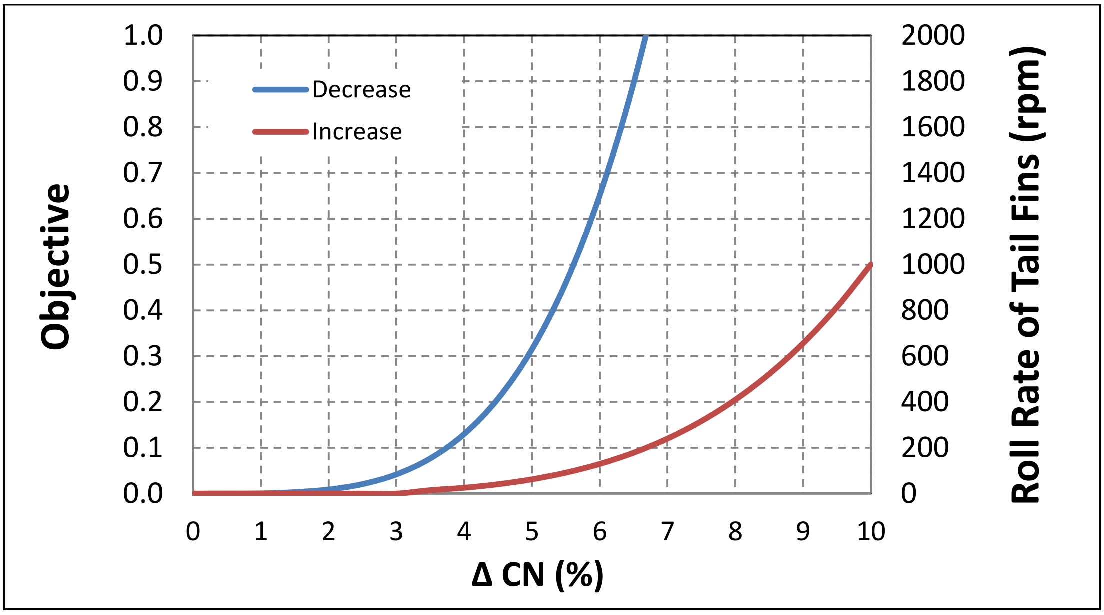


Figure 2-2 Objective as a Function of Change in Normal Force Coefficient

## 2.7 Flow Chart for the Optimization

Flow chart for the optimization design is given in Figure 2-3. First, initial geometry for the optimization process is decided and disturbance on the optimization parameters are applied to the initial geometry. Steady solutions are performed to obtain normal force data and unsteady solutions are performed to obtain roll rate data. Then, objective values are calculated for the initial geometry and the disturbed geometries. According to the derivatives of the objective values to the optimization parameters, gradient vector is obtained. Then in the gradient vector direction a line search algorithm is applied. The objective values of the models for the line search are calculated by performing steady and unsteady analyses. The model which has the minimum objective value in the line search process is the model which is the output of the first optimization step and the initial model for the second optimization step. The same procedure is applied to this model. The process is terminated when the objective value is converged.

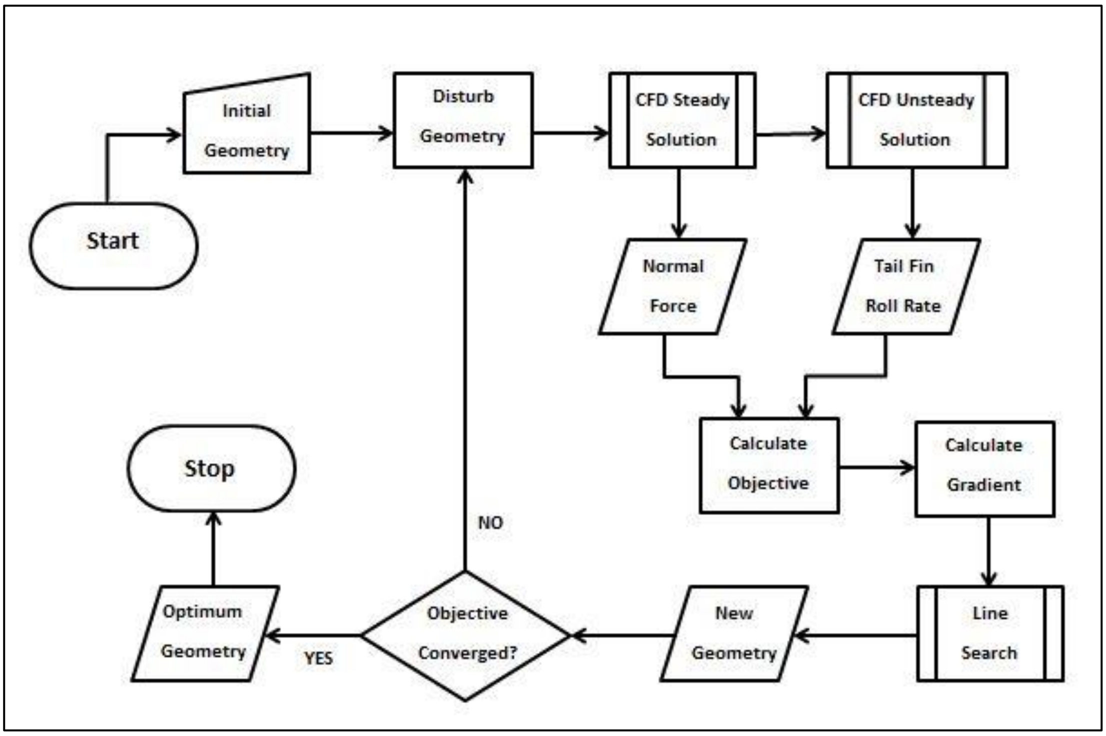


Figure 2-3 Flow Chart for the Optimization Problem

# CHAPTER 3

# VALIDATION STUDIES

In this part, the validation of numerical methodology to simulate free-to-rotate tail fin is represented. For validation study, two test case models, which are Tandem-Control-Missile (TCM) and Modified-Tandem-Control-Missile (M-TCM), are investigated by steady and unsteady RANS solutions with FLUENT and the results of these solutions are compared with experimental data.

TCM is one of the most used missile model in wind tunnel testing for aerodynamic researches by NASA. There are various modified versions of this model. Since the experimental data of M-TCM model is more comprehensive and extensive compared to standard TCM model, M-TCM model is chosen as the first test case model in validation analyses. Furthermore, grid independence and turbulence model studies are conducted for M-TCM model.

## 3.1 Modified Tandem Control Missile (M-TCM) Test Case

M-TCM model has a canard-body-tail (CBT) configuration. The model was a cruciform missile configuration that consisted of a remote-controlled canard forebody with pointed tangent ogive nose and a cylindrical body that incorporated an electronic/electromagnetic braking system [6]. This braking system was interfaced with a tail-fin afterbody that was either fixed or free-to-rotate. The tests were performed in the low-Mach-number test section of the Langley Unitary Plan Wind Tunnel, which is a variable-pressure, continuous-flow facility. The tests were conducted at Mach numbers of 1.70, 2.16, and 2.86. The nominal angle of attack range was -4° to 18° and at a Reynolds number of $6.6 \times 10^6$ per meter. Details of TCM model are shown in Figure 3-1 and details of the canard and tail fins are shown in Figure 3-2 (dimensions in millimeters).

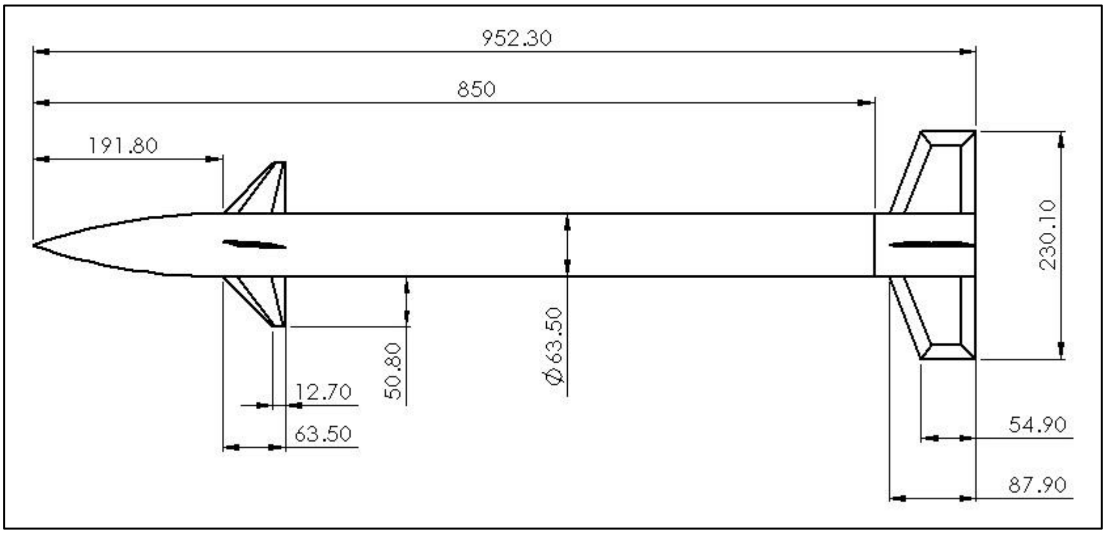


Figure 3-1 Geometry of M-TCM [6]

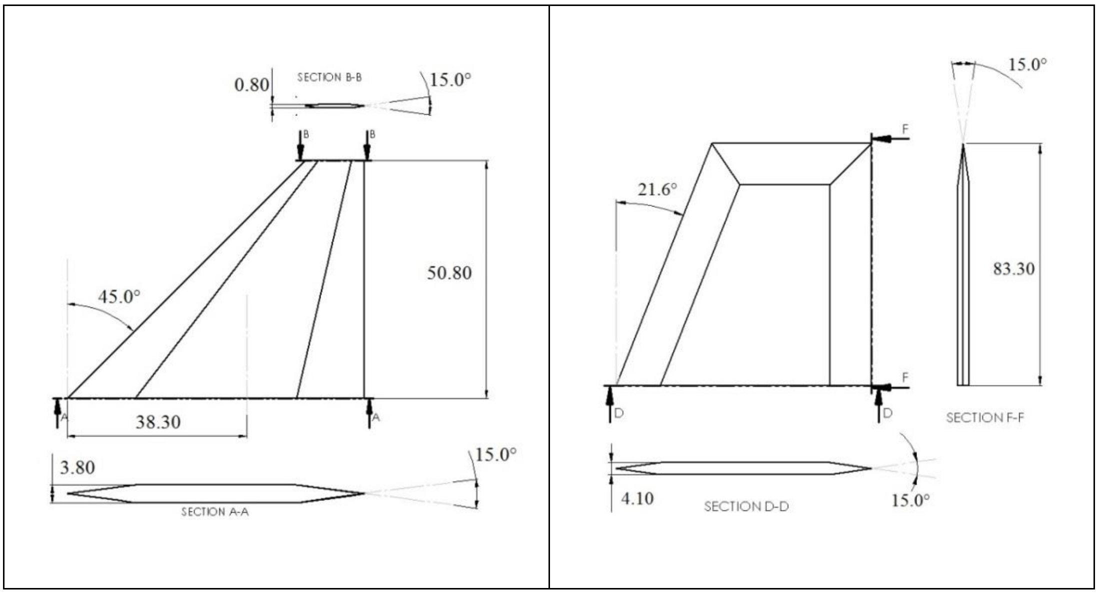


Figure 3-2 Geometry of Canard (left) and Tail (right) Fins [6]

### 3.1.1 Solid Model

The solid model is created by GAMBIT. The solid model is shown in Figure 3-3.

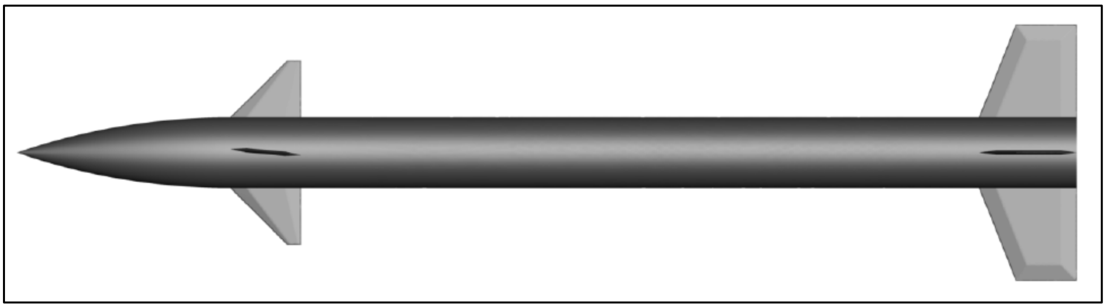

Figure 3-3 Solid Model of M-TCM

Each horizontal canard fins are deflected by 5° such that clockwise roll moment occurs on missile when viewed from base. Vertical canard fins are not deflected. The aileron deflections in canard fins are represented in Figure 3-4.

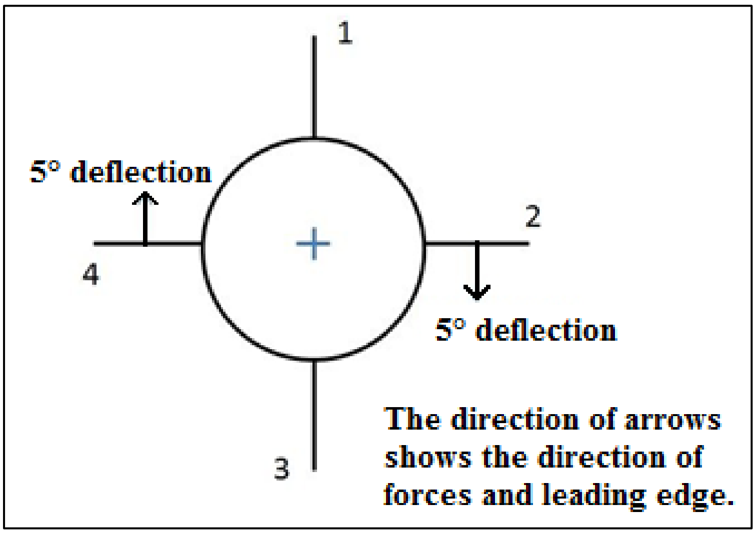


Figure 3-4 Deflection in Canard Fins of M-TCM (viewed from base)

Two cylindrical fluid domains are created, one of them is for fixed parts of the model and the other one is for the rotating parts of the model. The fixed fluid domain starts behind 15 model lengths from the model nose, ends 25 model lengths far from the model base; and the radius of this domain is 15 model lengths. The rotating fluid domain starts 13.6 model diameters from the model nose, ends 1.5 model diameters from the model base; and the radius of this domain is 6.7 model diameters. The fixed and rotating fluid domains are show in Figure 3-5.

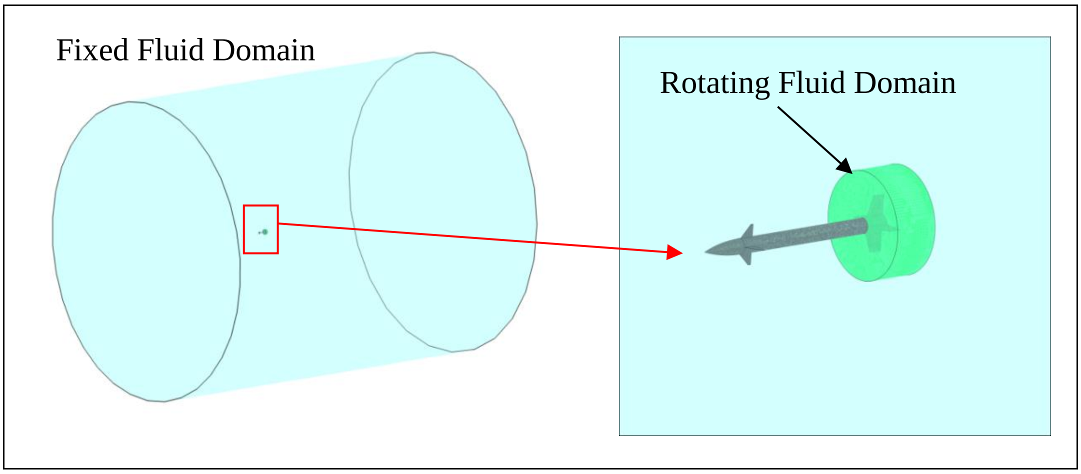


Figure 3-5 Fixed and Rotating Fluid Domains

### 3.1.2 Grid Generation

Unstructured triangular surface grids and tetrahedral volume grids are generated by GAMBIT. The growing rate is limited for surface grid to 1.1 and for volume grid to 1.15. Over the wall surfaces 25 prismatic layers are created in order to capture the boundary layer flow successfully by Tgrid. For the turbulence models used in this study, the $y^+$ value for the wall surfaces should be around 1. And this criterion is taken into account while generating grid. The grid size is decreased in the locations where flow might change direction. The surface and volume mesh are given in Figure 3-6.

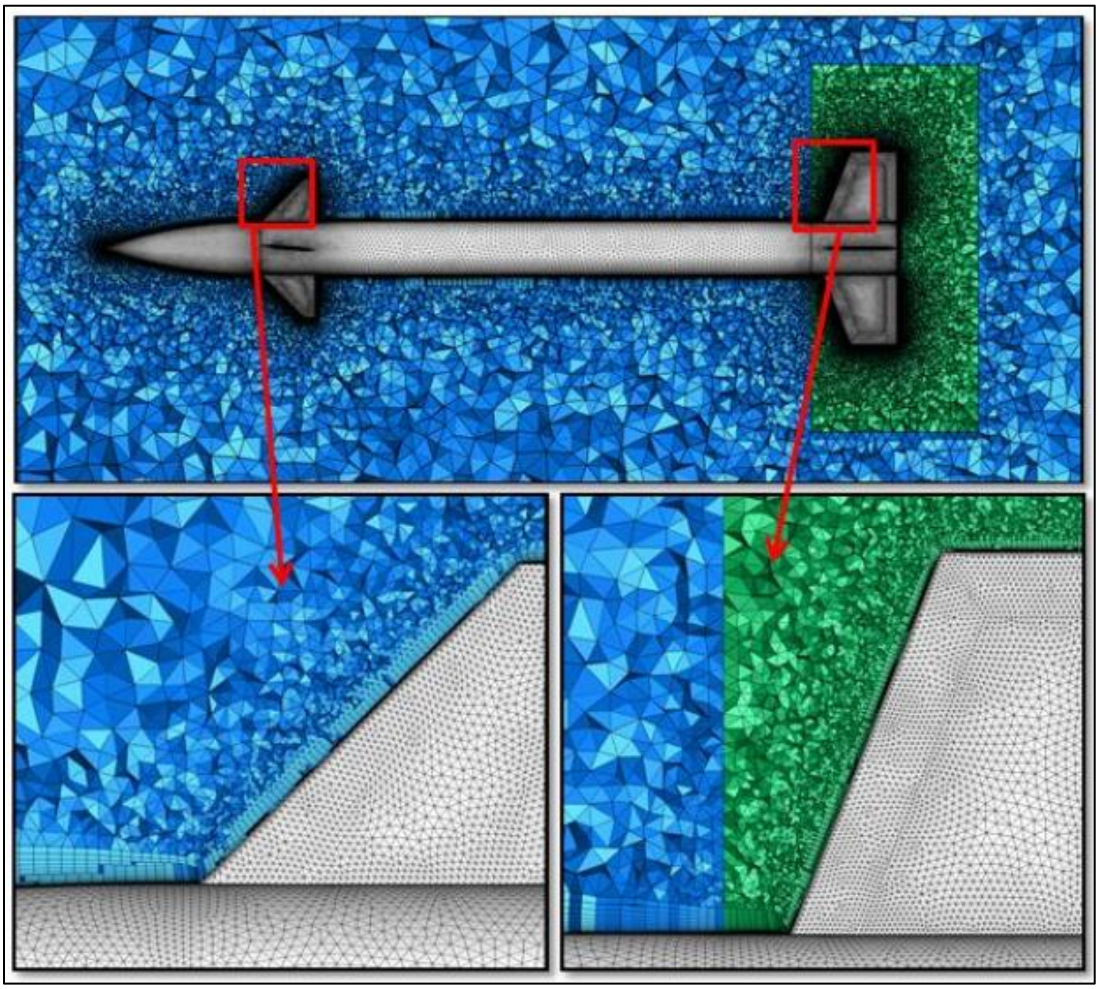

Figure 3-6 Surface and Volume Grids

For Mach number of 2.86 and angle of attack of 0°, the $y^+$ value distribution over the wall surfaces is represented in Figure 3-7.

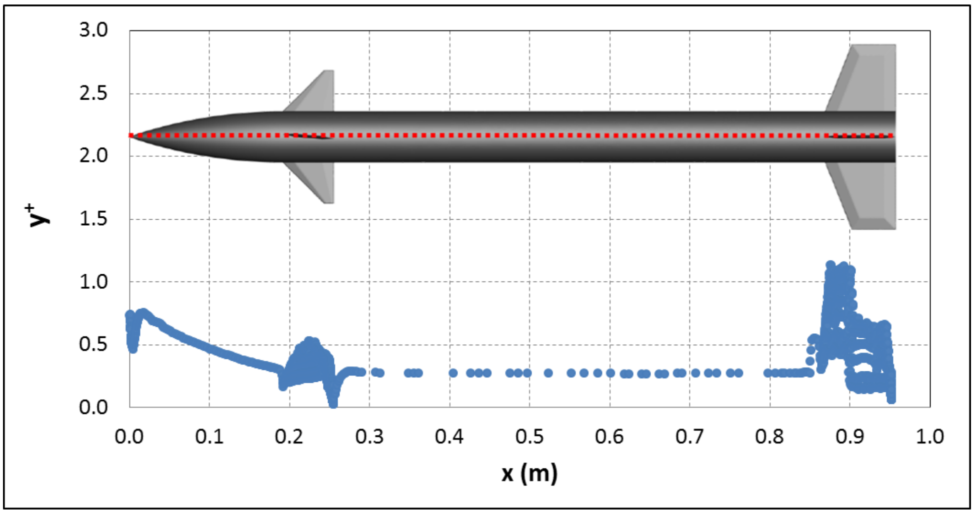


Figure 3-7 y+ Values over the Wall Surfaces

### 3.1.3 Boundary Conditions

The model surfaces are defined as no-slip wall boundary condition. The outer surfaces of fixed fluid domain are defined as pressure far field boundary condition with constant freestream static pressure, static temperature and velocity. The surfaces between the fixed and rotating fluid domains are defined as interface boundary condition to give mesh rotation during 1-DOF unsteady solution. The applied boundary conditions are shown in Figure 3-8.

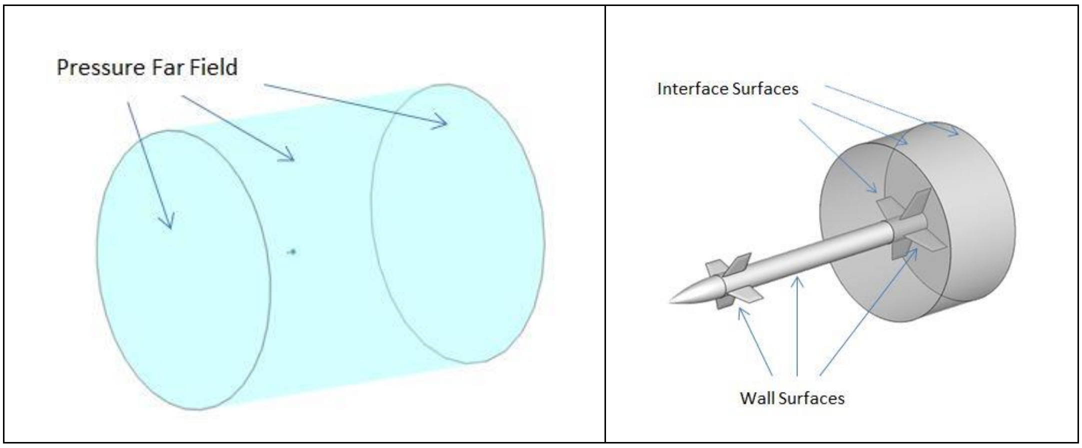


Figure 3-8 Boundary Conditions

### 3.1.4 Steady Analyses Results

First the steady analyses are performed with FLUENT. The aim is to validate the results of the fixed tail configuration by comparing experimental data [6]. Mesh independence and turbulence model studies are performed for the axial force and roll moment coefficients since these two parameters are more related with the roll characteristics of the model. Then normal force coefficient and location of the center of pressure are compared with wind tunnel test data. Mach number of 2.86 is chosen for the analyses.

Properties of freestream flow are given in Table 3-1.

Table 3-1 Fluid Properties (M-TCM)

| | |
|---|---|
| **Mach Number** | 2.86 |
| **Reynolds Number** | $6.6 \times 10^{6}\ m^{-1}$ |
| **Fluid Type** | Air |
| $\mathbf{P_{static,\infty}}$ | 3114.2 Pa |
| $\mathbf{T_{static,\infty}}$ | 123.3 K |
| $\boldsymbol{\rho_{,\infty}}$ | $0.08798\ kg/m^{3}$ |

### 3.1.5 Mesh Independence and Turbulence Model Study

In order to determine the most suitable grid and turbulence model, mesh independence and turbulence model studies are conducted.

#### 3.1.5.1 Mesh Independence Study

A grid sensitivity study is carried out in order to be sure about independence of the grid and to save time for analyses. Three different grids are examined which are coarse (3,238,026 cells), medium (7,449,726 cells) and fine (12,655,197 cells) meshes. These three grids are represented in Figure 3-9 and Figure 3-10.

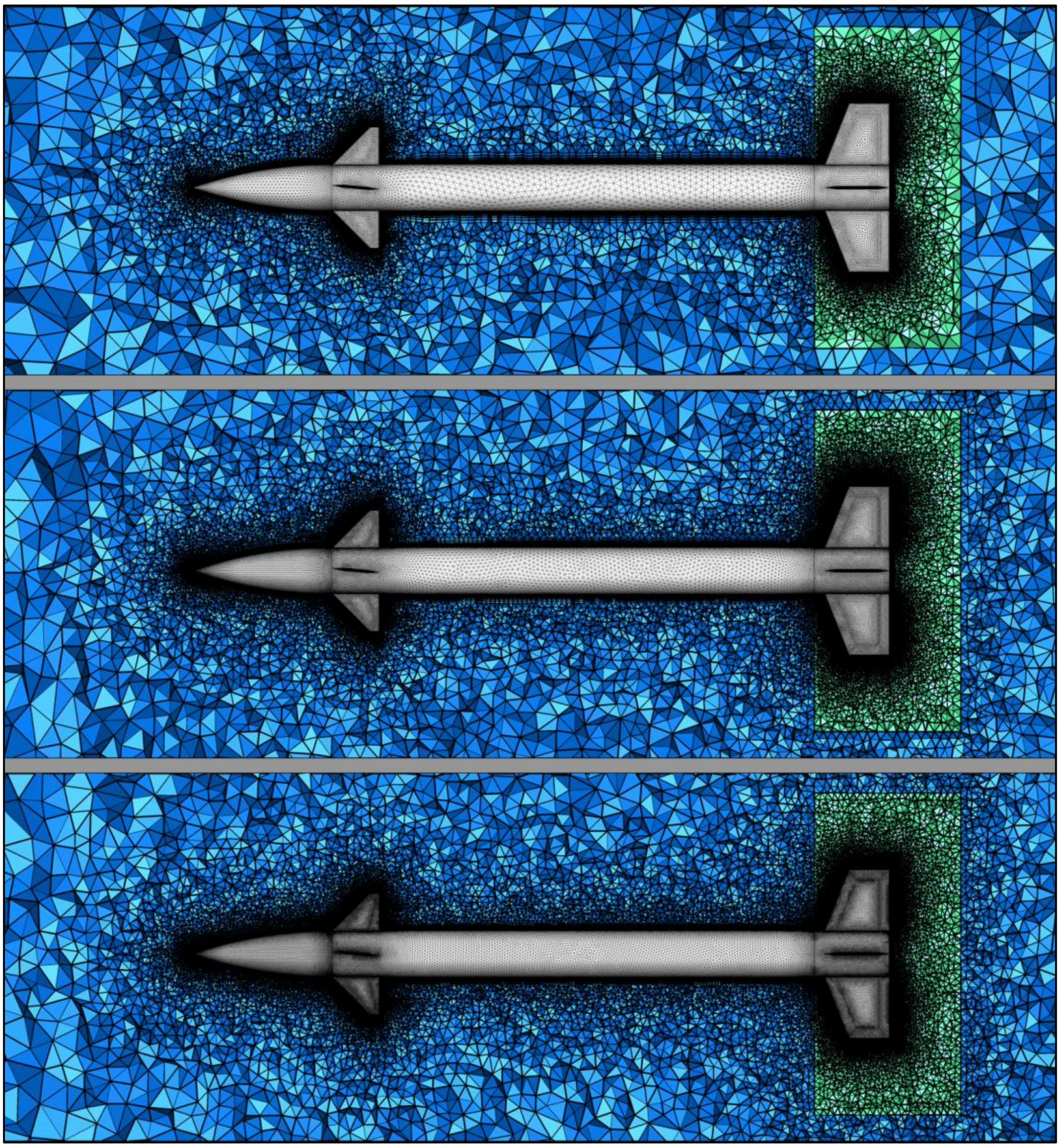

Figure 3-9  Grids for Grid Convergence (top:coarse; middle:medium; bottom:fine)

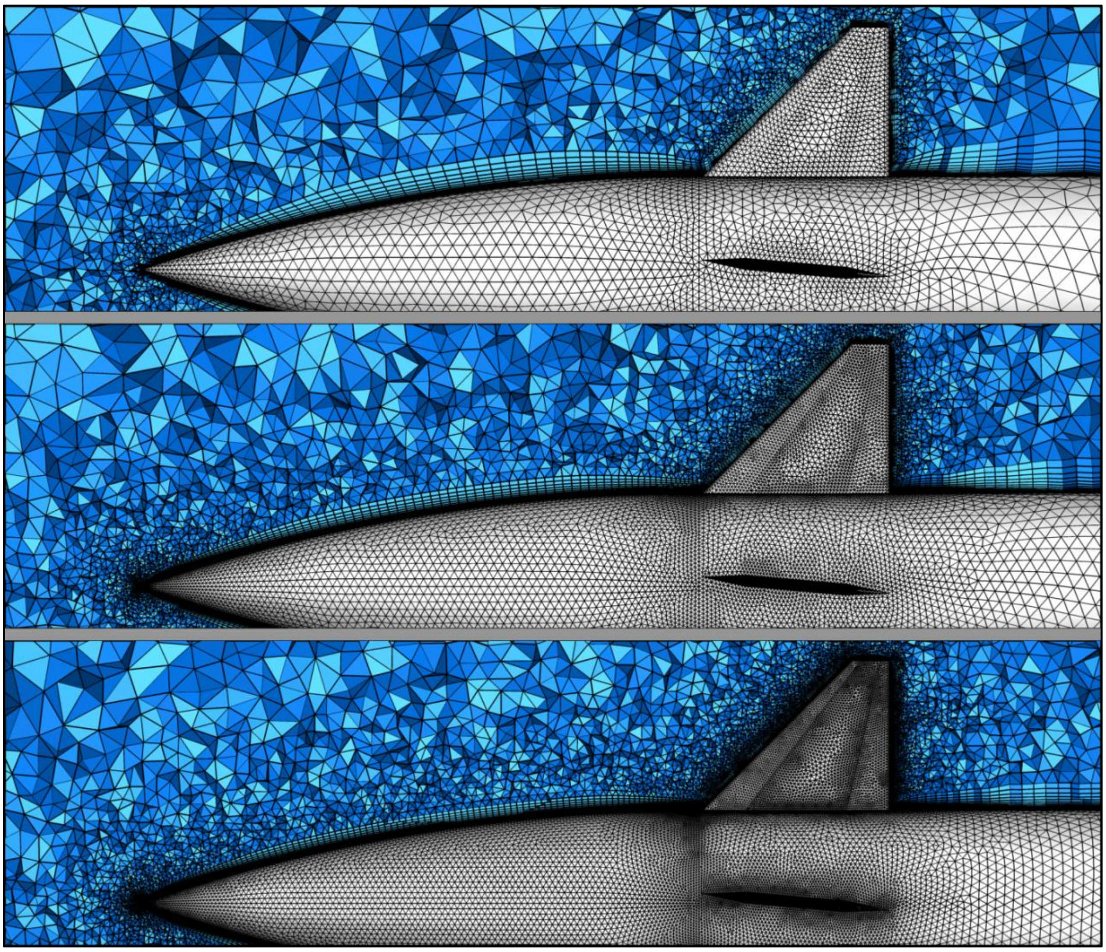

Figure 3-10  Forebody Grids for Grid Convergence (top:coarse; middle:medium;bottom:fine)

For mesh convergence analyses, SST k-ω turbulence model is used. The effect of mesh quality on axial force and roll moment coefficients is represented in Figure 3-11 and Figure 3-12, respectively. It can be seen in the figures that the suitable grid is the medium grid and this grid is used for the rest of the analyses in the thesis in order to save both time and computer power.

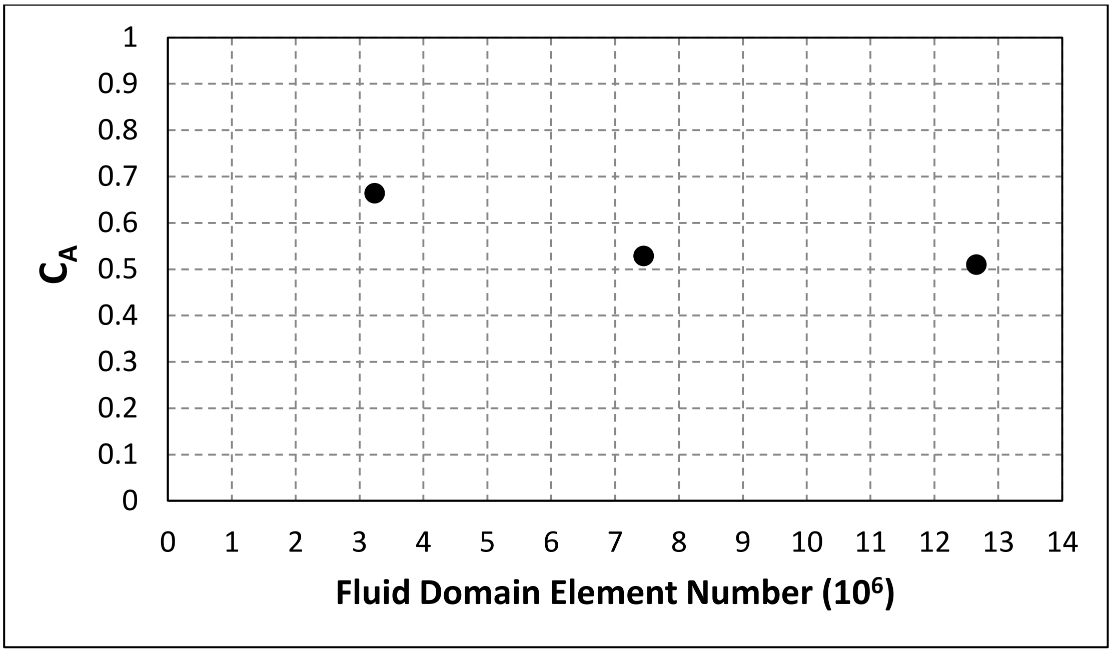


Figure 3-11 Axial Force Coefficient for Different Mesh Quality (M-TCM)

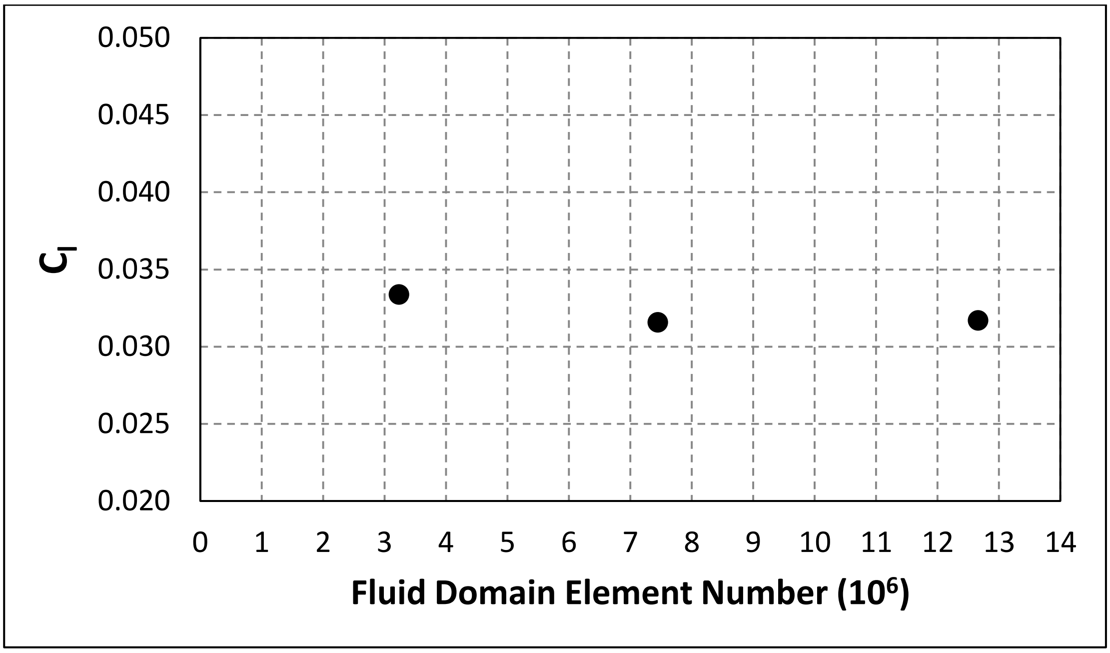


Figure 3-12 Roll Moment Coefficient for Different Mesh Quality (M-TCM)

#### 3.1.5.2 Turbulence Model Selection Study

Three different turbulence models, which are Spalart-Allmaras, Realizable k-ε and SST k-ω, are analyzed and compared with the experimental data [6]. The results are shown in Figure 3-13 and Figure 3-14. According to the figures, although these three turbulence models gives similar results for the rolling moment coefficient, SST k-ω model gives the best result for the axial force coefficient compared to experimental data. Therefore, SST k-ω turbulence model is used for the rest of the analyses.

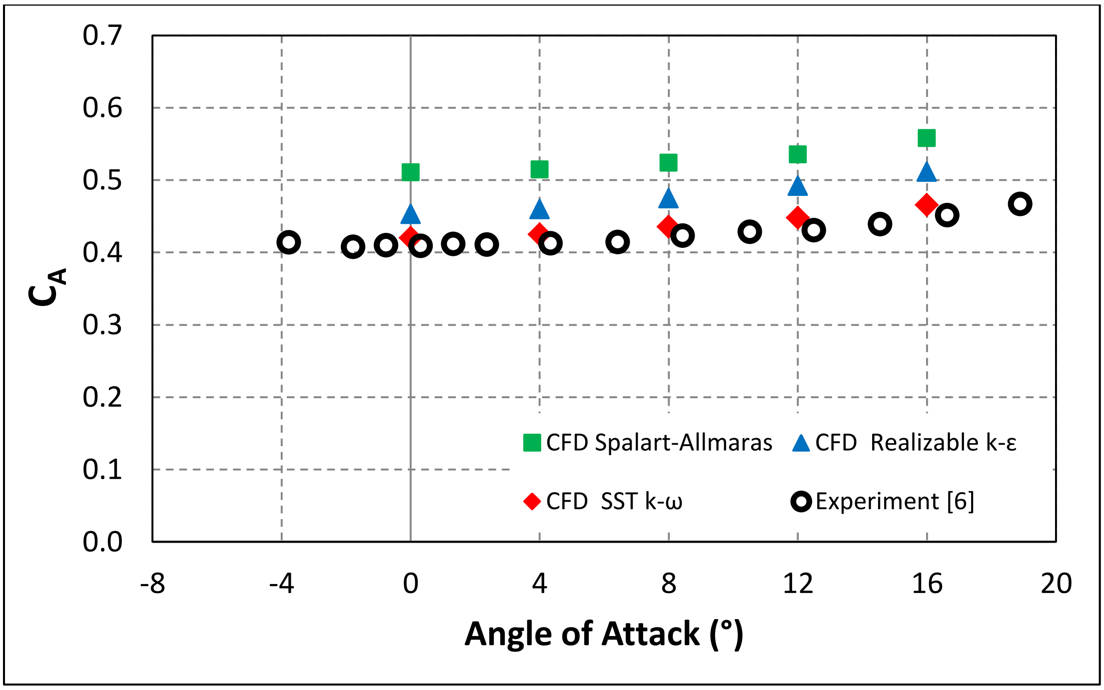


Figure 3-13 Axial Force Coefficient for Different Turbulence Model (M-TCM)

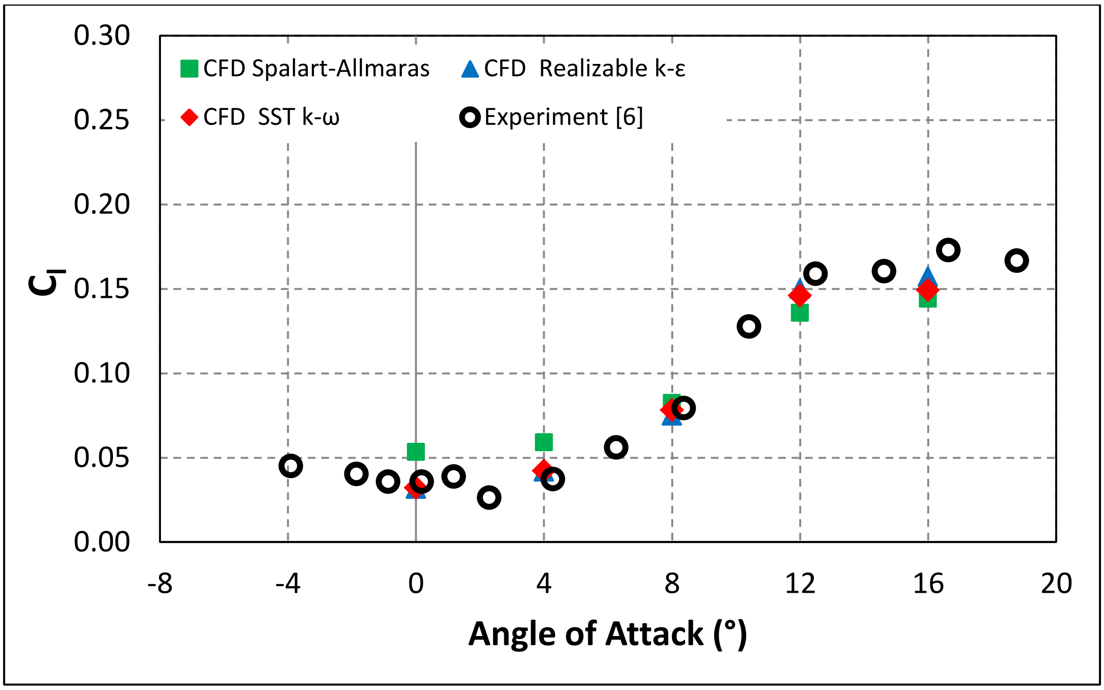


Figure 3-14 Roll Moment Coefficient for Different Turbulence Model (M-TCM)

### 3.1.6 Normal Force and Center of Pressure

Using the medium mesh and SST k-ω turbulence model, the normal force coefficient and location of center of the pressure are compared with test data, in Figure 3-15 and Figure 3-16, respectively. It can be seen in the figures that the normal force coefficient and the location of center of pressure are good agree with the experimental data.

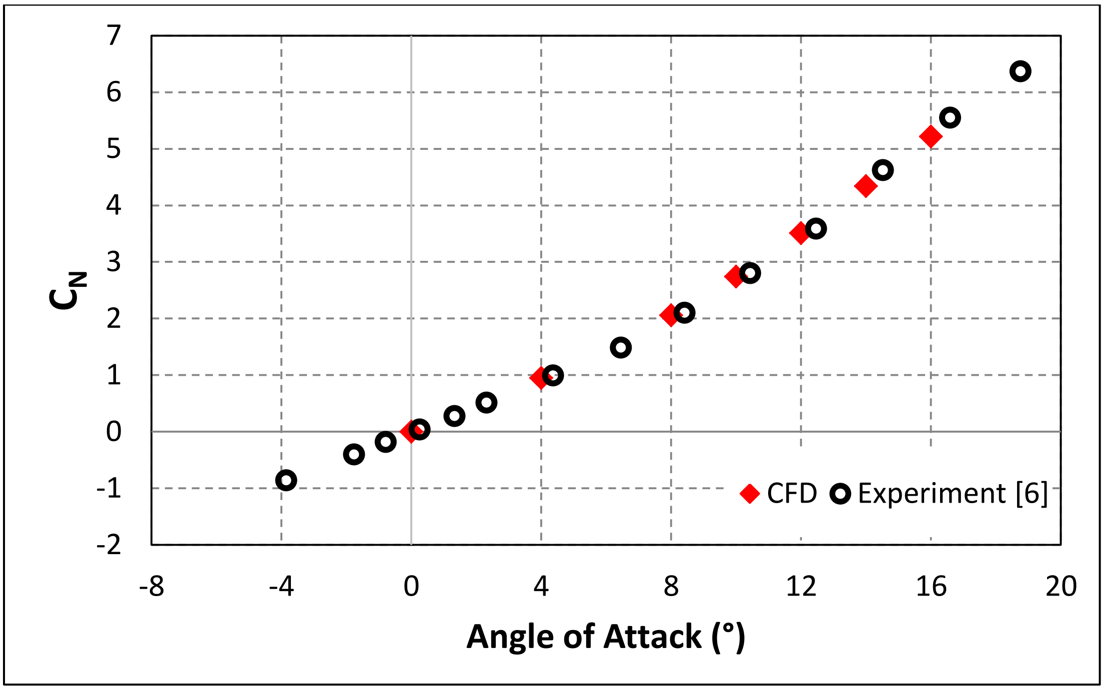


Figure 3-15 Comparison of Normal Force Coefficient (M-TCM)

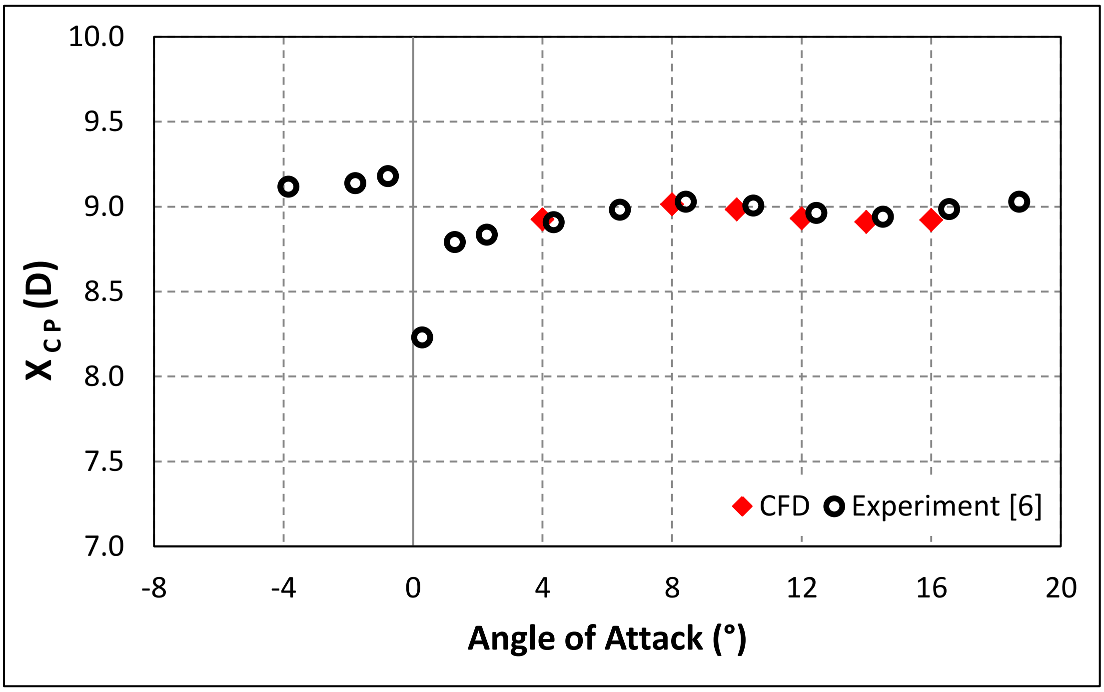


Figure 3-16 Comparison of Location of Center of Pressure (M-TCM)

### 3.1.7 Unsteady Analyses Results

The results of the steady analyses are in good agreement with the experimental data. Then, unsteady analyses are performed to compare the roll rate data of the free-to-rotate tail fins with experimental data.

For unsteady analyses, only roll rotation of the missile is allowed to be free. The translations in x, y and z - direction, and rotations in yaw and pitch motion are restricted to be zero by a UDF developed. The UDF is given in Appendix B.

The results of the roll rate of the free-to-rotate tail fins are represented in Figure 3-17. It can be said that the roll rate data of the free-to-rotate tail fins obtained by unsteady analyses are consistent with the experimental data. For the angle of attack of 10° the tails fins stop rolling and this situation is called aero-roll-lock. From this angle of attack the tail fins are not affected by the vortices arising from canard fins.

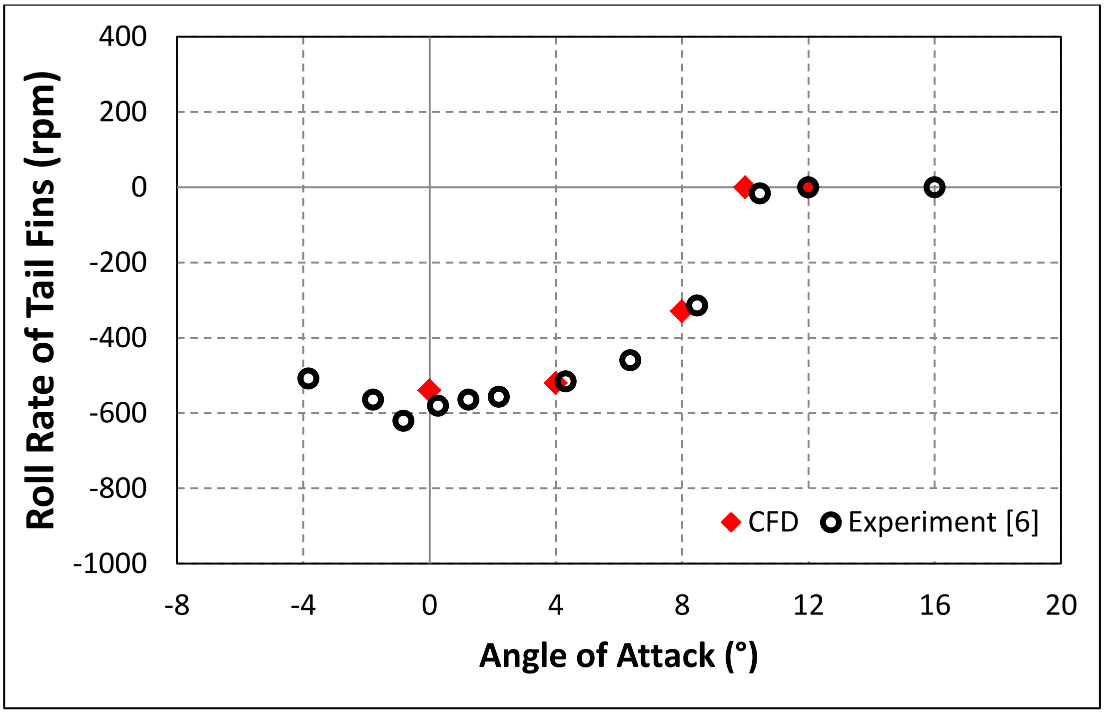


Figure 3-17 Comparison of Roll Rate of Tail Fins (M-TCM)

The roll moment coefficient of the free-to-rotate tail fins as a function of time is represented in Figure 3-18. Between the time values of 0 and 0.4 s, there is a transient region. After the transient region the solution is converged and the mean of the rolling moment coefficient converges to zero as predicted. This means that the induced roll moment is eliminated. The oscillations in the rolling moment coefficient repeats with an interval of 90° of tail roll angle. The four oscillations correspond to one rotation of tail fins set.

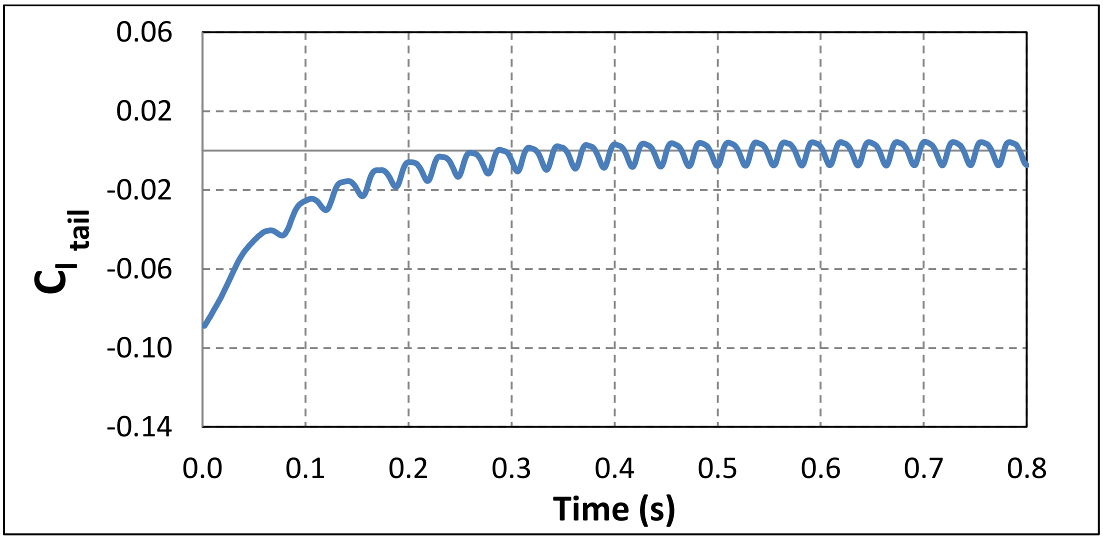


Figure 3-18 Rolling Moment Coefficient for Free-To-Rotate Tail Fins (M-TCM)

## 3.2 Tandem Control Missile (TCM) Test Case

Tandem Control Missile (TCM) was a cruciform missile configuration that consisted of a cylindrical body with canards, aft tail fins, and a tangent ogive nose [4]. The canards and tail fins had slab cross sections with beveled leading and trailing edges. In order for the model to have a free-rolling tail-fin assembly, the tail-fin afterbody was mounted on a set of low-friction ball bearings and was free to rotate through 360°. The canards were deflected to provide roll control and yaw control. The tail fins were not deflected and the tail-fin assembly had no braking system. The tests were performed in the low-Mach-number test section of the Langley Unitary Plan Wind Tunnel, which is a variable-pressure, continuous-flow facility. The tests were conducted at Mach numbers of 1.70, 2.16, 2.36 and 2.86. The nominal angle-of-attack range was -4° to 18° at a model (canard) roll angle of 0° and at a Reynolds number of 6.6 x $10^6$ per meter [4]. Details of the model are shown in Figure 3-19 and details of the canard and tail fins are shown in Figure 3-20 (dimensions in inches).

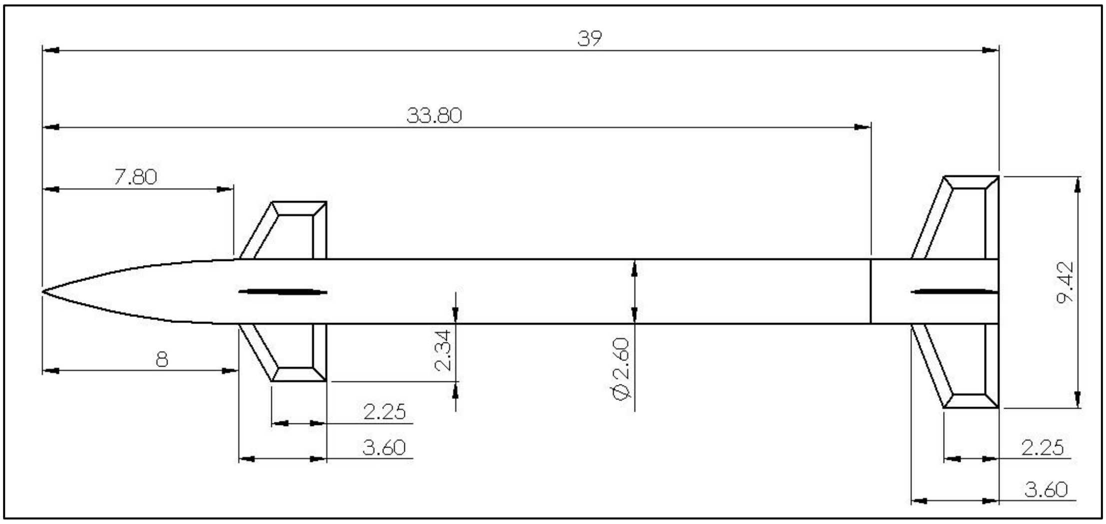


Figure 3-19 Geometry of TCM [4]

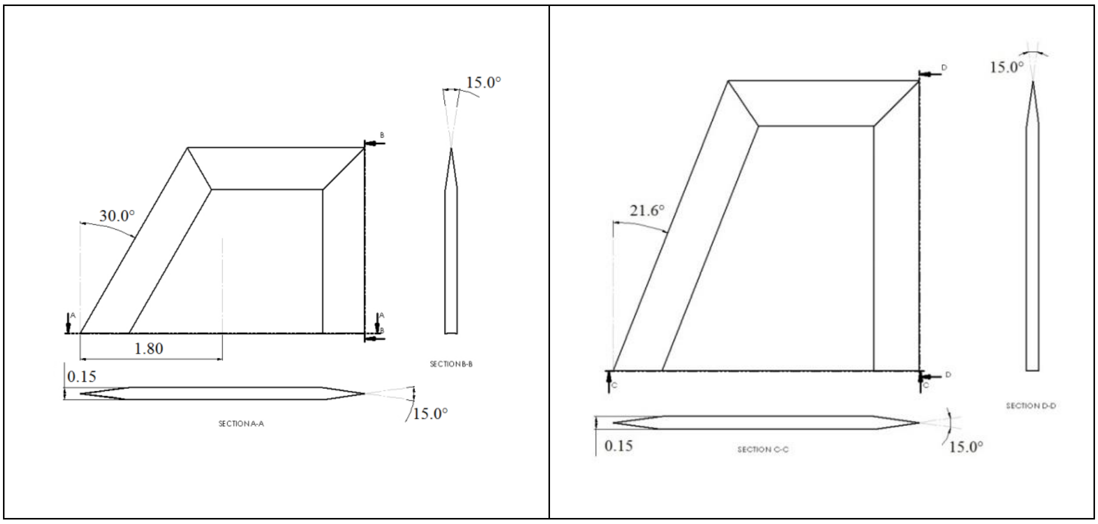


Figure 3-20 Geometry of Canard (left) and Tail (right) Fins [4]

### 3.2.1 Solid Model

The solid model is created by using GAMBIT. The solid model is shown in Figure 3-21.

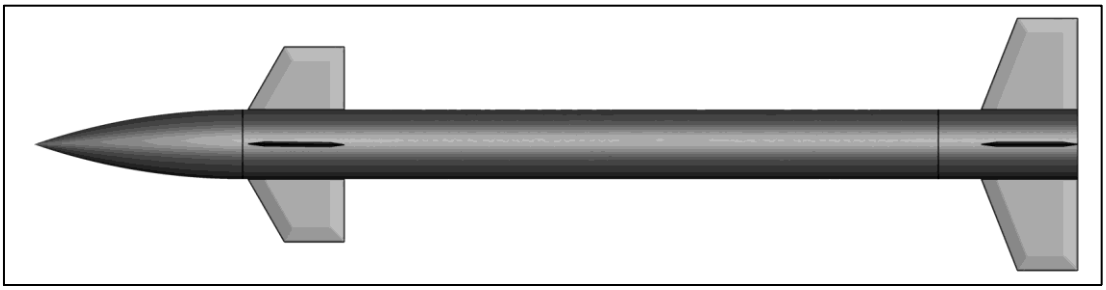

Figure 3-21 Solid Model of TCM

Each horizontal canard fins are deflected by 0.5° such that clockwise roll moment occurs on missile when viewed from back. Vertical canard fins are not deflected. The aileron deflections in canard fins (when viewed from base) are represented in Figure 3-22.

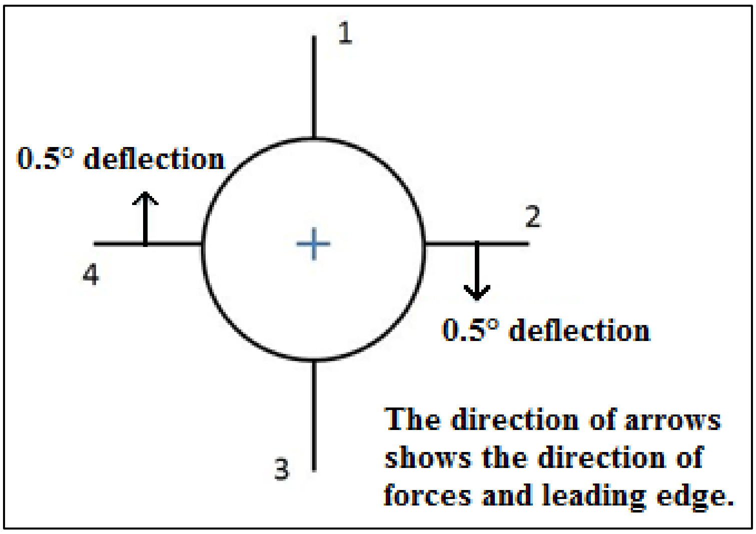


Figure 3-22 Deflection in Canard Fins of TCM (viewed from base)

### 3.2.2 Grid Generation

The grid generation procedure of TCM test case is the same with the procedure introduced in part 3.1.2.

### 3.2.3 Boundary Condition

The applied boundary conditions to TCM test case is the same with the procedure introduced in part 3.1.3.

### 3.2.4 Steady Analyses Results

Steady analyses of TCM test case are performed and the axial force, normal force and pitch moment coefficients are compared with experimental data. For the analyses Mach number of 2.16 is chosen.

Properties of freestream flow are given in Table 3-2.

Table 3-2 Fluid Properties (TCM)

| | |
|---|---|
| **Mach Number** | 2.16 |
| **Reynolds Number** | $6.6 \times 10^{6}$ $m^{-1}$ |
| **Fluid Type** | Air |
| $\mathbf{P_{static,\infty}}$ | 6431.7 Pa |
| $\mathbf{T_{static,\infty}}$ | 168.1 K |
| $\boldsymbol{\rho_{,\infty}}$ | 0.13325 $kg/m^{3}$ |

Axial force coefficient of TCM test case is represented by comparing with experimental data in Figure 3-23. For axial force coefficient the base part is not included into calculations. Normal force and pitch moment coefficient of TCM test case are represented by comparing with experimental data in Figure 3-24 and Figure 3-25, respectively.

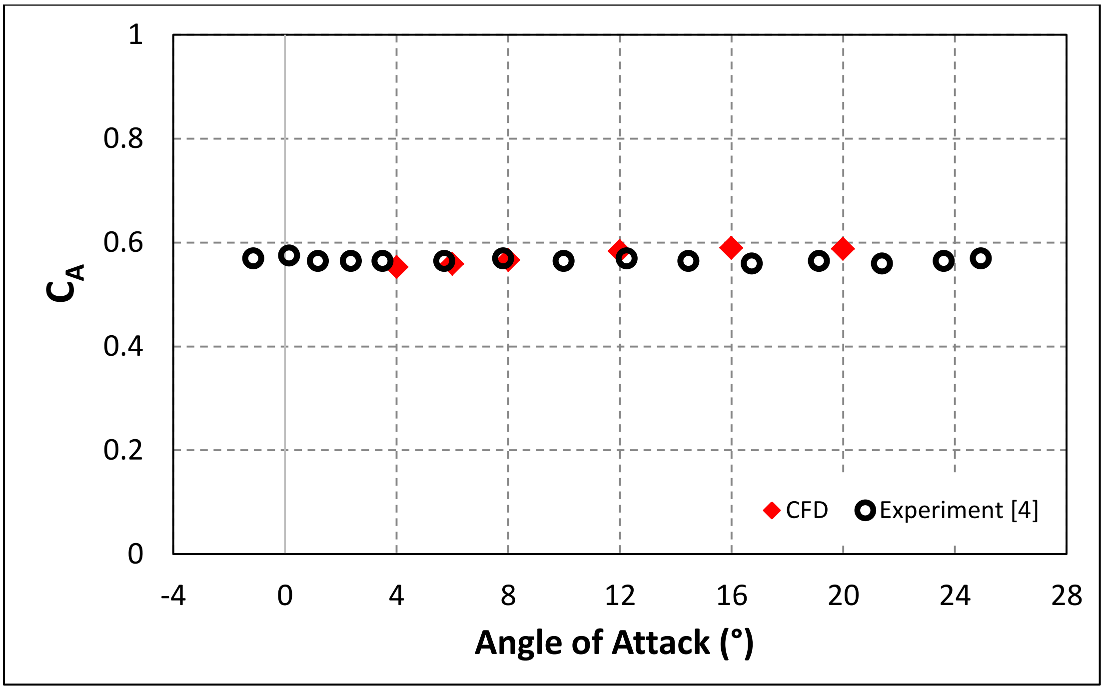


Figure 3-23 Comparison of Axial Force Coefficient (TCM)

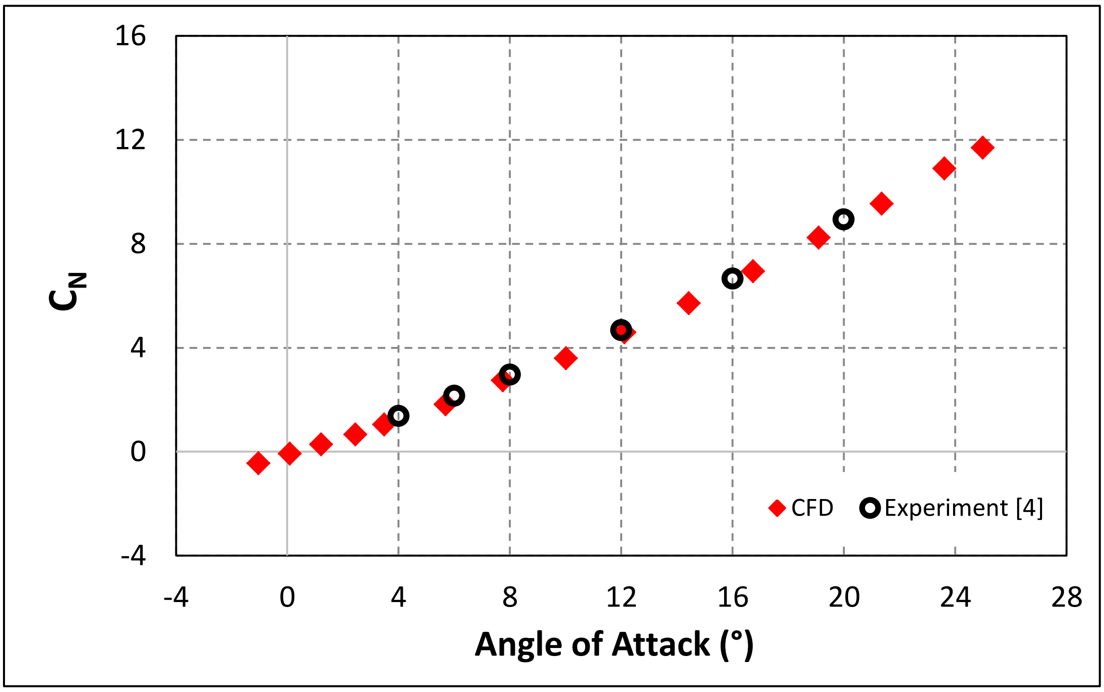


Figure 3-24 Comparison of Normal Force Coefficient (TCM)

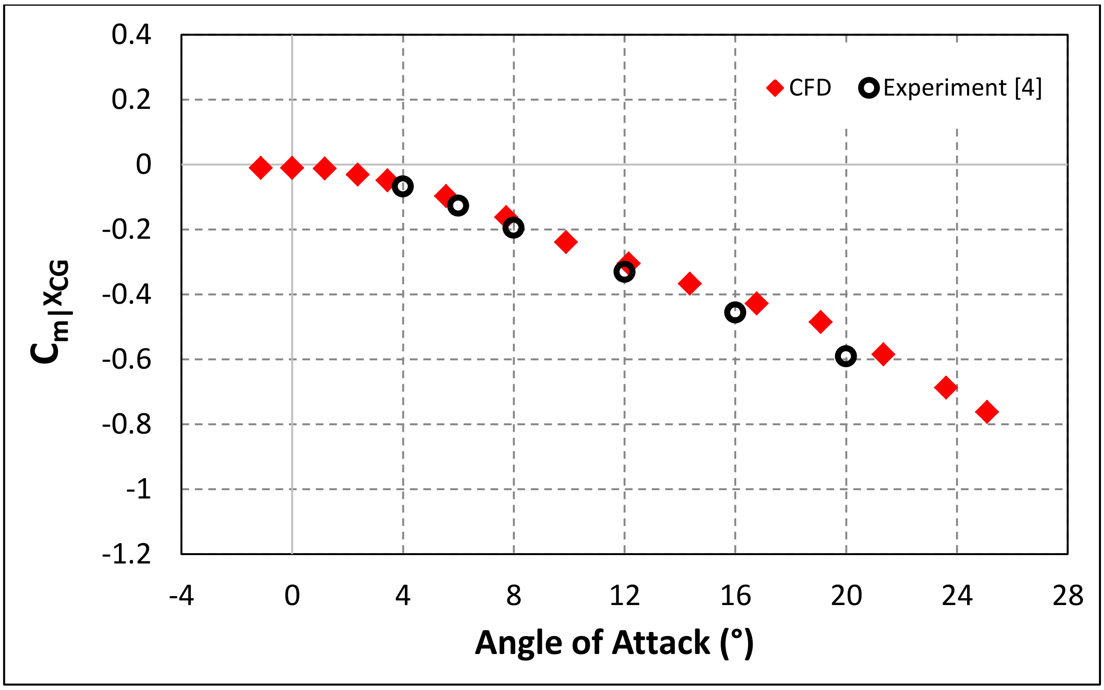


Figure 3-25 Comparison of Pitching Moment Coefficient (TCM)

### 3.2.5 Unsteady Analyses Results

After validating that the static coefficients are good agreement with experimental data, unsteady analyses are performed and compared with experimental data in

The results of the steady analyses are in good agreement with the experimental data. Then, unsteady analyses are performed to compare the roll rate data of the free-to-rotate tail fins with experimental data. The results of the roll rate of the free-to-rotate tail fins are represented in Figure 3-26.

It can be said that the results are suitable with experimental data up to angle of attack of 8°; however, from this angle of attack the results are not close to experimental data. The wind tunnel tests were performed in 1970s; therefore, there would be unclearness during tests. In the tunnel report, there are some contradictions related to test results.

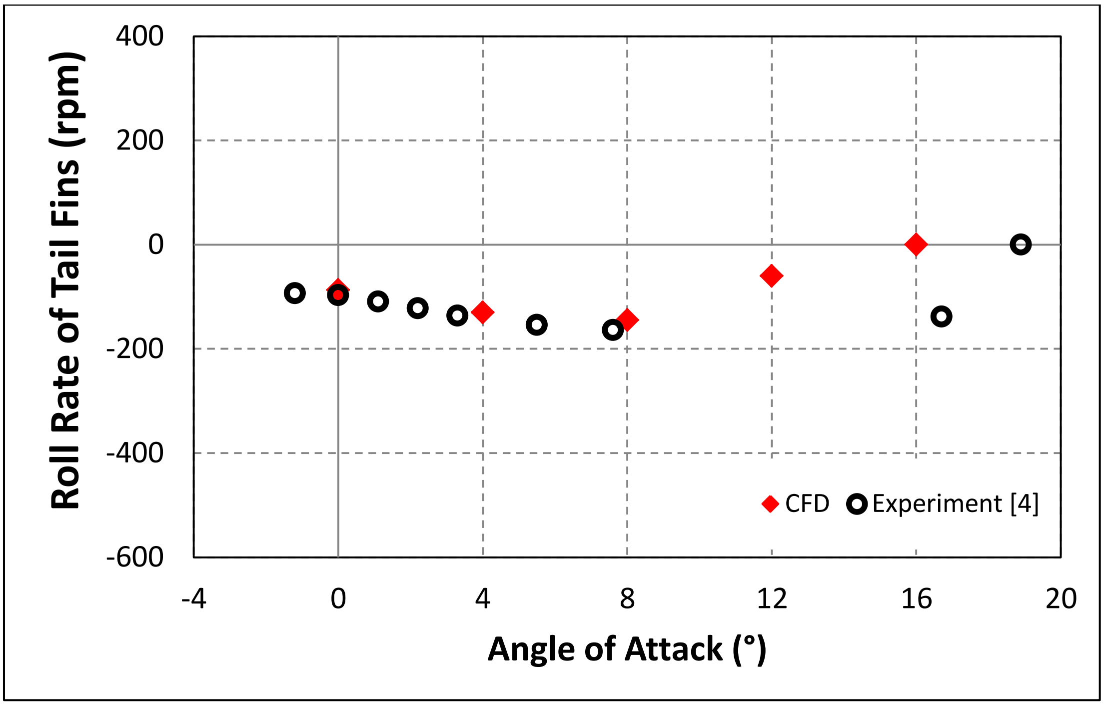


Figure 3-26 Comparison of Roll Rate of Tail Fins (TCM)

## 3.3 Effect of Moment of Inertia on Roll Rate of Tail Fins

In order to study the effect of moment of inertia on the roll rate of tail fins, unsteady analyses for the angle of attack of 4° are performed with different four moment of inertia values. The moment of inertia value of tail fins of M-TCM model is taken as $I_{XX}$ and additional three moment of inertia value are obtained by multiplying with 0.6, 1.5 and 2. The results are represented in Figure 3-27. It can be seen in the figure that after the transient region the roll rate of the tail fins are convergence to almost the same value for these four moment of inertia values.

The analyses are performed for different angles of attack and the results are represented in Figure 3-28. It is seen in the figure that if the moment of inertia value increases, the angle of attack where aero-roll-lock start increases. The reason can be explained that the moment of inertia is a damping for deceleration of the tail fins.

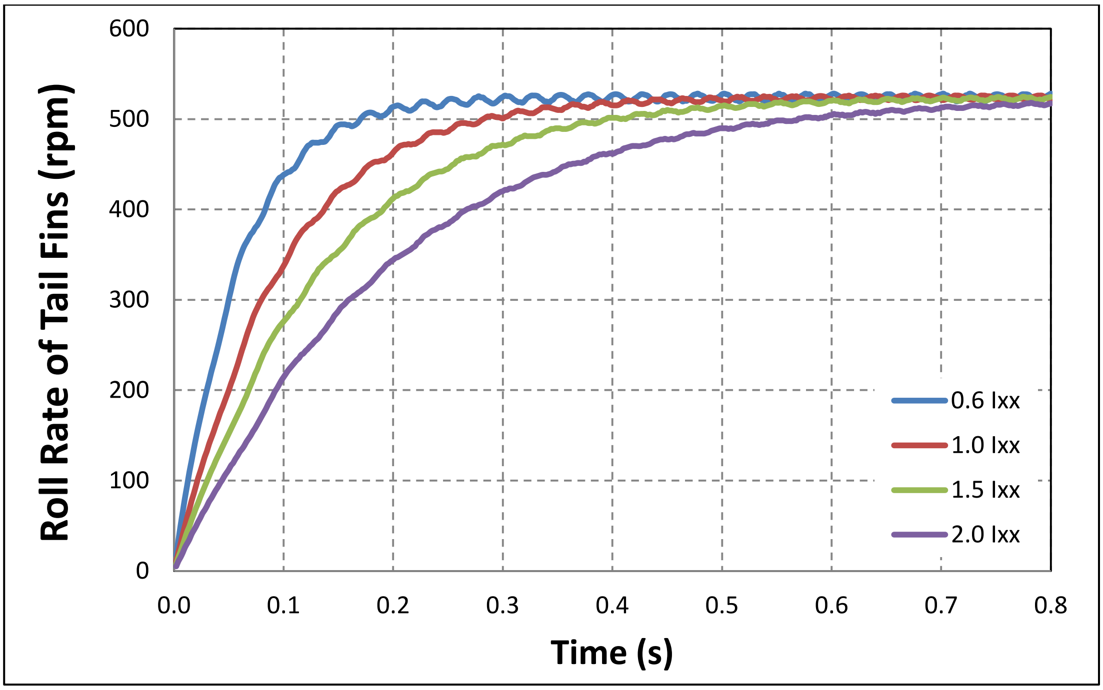


Figure 3-27 Effect of Moment of Inertia on Roll Rate of Tail Fins (M-TCM)

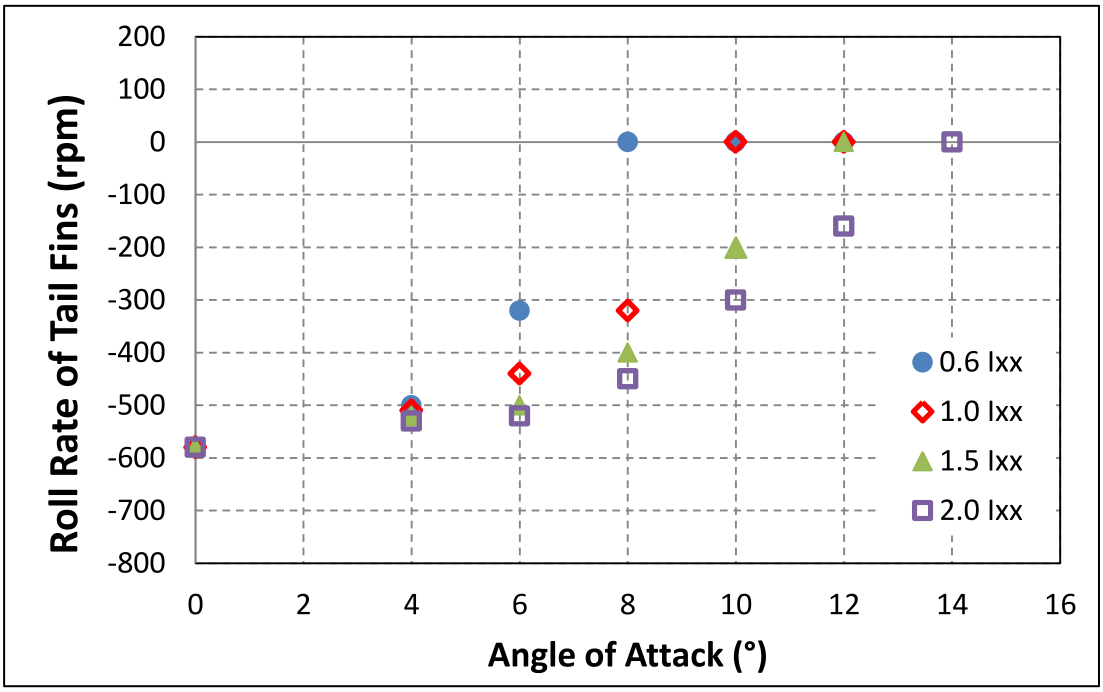


Figure 3-28 Effect of Moment of Inertia for Different Angles of Attack (M-TCM)

# CHAPTER 4

# OPTIMIZATION STUDIES

In this part, the planform optimization process of the free-to-rotate tail fins is studied. M-TCM test case model is chosen as the base model for optimization process. The initial model for the free-to-rotate tail fins is chosen as a rectangular planform which gives same lift curve slope with the tails of M-TCM test case model. At each optimization step, gradient vector is obtained by disturbing the optimization parameters and line search algorithm is applied in this gradient vector direction. The validated CFD methods for steady and unsteady analyses are used to solve the models obtained throughout the optimization process with FLUENT. Results of the optimum planform of the free-to-rotate tail fins are compared with the results of the initial rectangular tail planform and tail planform of M-TCM model.

## 4.1 Geometric Limitations for Tail Fins

The location and length of the root chord are kept constant throughout the optimization process. The sweep angle on the leading edge is restricted to be a positive value. And the back sweep angle at trailing edge is set to be a free parameter under the effect of leading edge sweep angle, tip chord and span length.

## 4.2 Initial Geometry for Optimization

Considering tail fins of M-TCM model are the optimized shape by the roll rate minimization, a rectangular fin geometry which satisfies the same normal force coefficient is searched by iterative analyses. The analyses are performed for the angles of attacks of 4° and 8°. The parameters of the tails of original and rectangular tail fin are given in Table 4-1 and the solid models of these two models are given in Figure 4-1.

Table 4-1 M-TCM and Initial Tail Parameters

| | $\Lambda_{LE}$ | $C_{tip}$ | b | $C_{N@\alpha=4°}$ | $C_{N@\alpha=8°}$ |
|---|---|---|---|---|---|
| **M-TCM Tail Fin** | 21.6° | 54.9 mm | 83.3 mm | 0.947 | 2.057 |
| **Rectangular Tail Fin** | 0.0° | 87.9 mm | 70.0 mm | 0.944 | 2.059 |

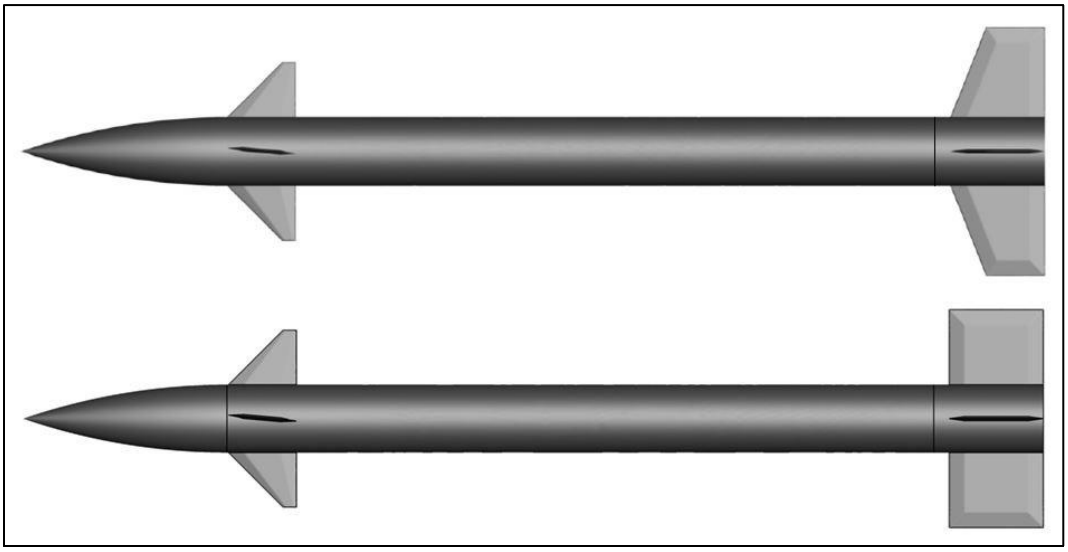

Figure 4-1 Solid Models of M-TCM and Initial Geometry for Optimization

## 4.3 Optimization Analyses

Since both the roll rate of the tail fins and the normal force coefficient of the tail fins are critical for the optimization, angle of attack of 4° is chosen as the design point. The reasons for this design point are,

- The roll rate characteristics of the free-to-rotate tail fins are very similar between 0° and 4°.
- The lift-curve slopes of the tail fins are generally constant for low angle of attack (e.g. 4°).

Considering the minimum grid size and numerical errors in mathematical calculations the disturbance in geometrical parameters should not be too small; moreover, the disturbance in geometrical parameters should not be too large in order not to calculate wrong gradient vector and also not to pass the minimum point. Analyses are performed for the initial geometry with different geometrical disturbances to determine suitable range of the disturbance in geometrical parameters.

The effect of the amount of disturbance in the leading edge sweep angle is represented in Figure 4-2. From the figure it can be said that the disturbance in leading edge sweep angle should be between 0.1 and 0.34.

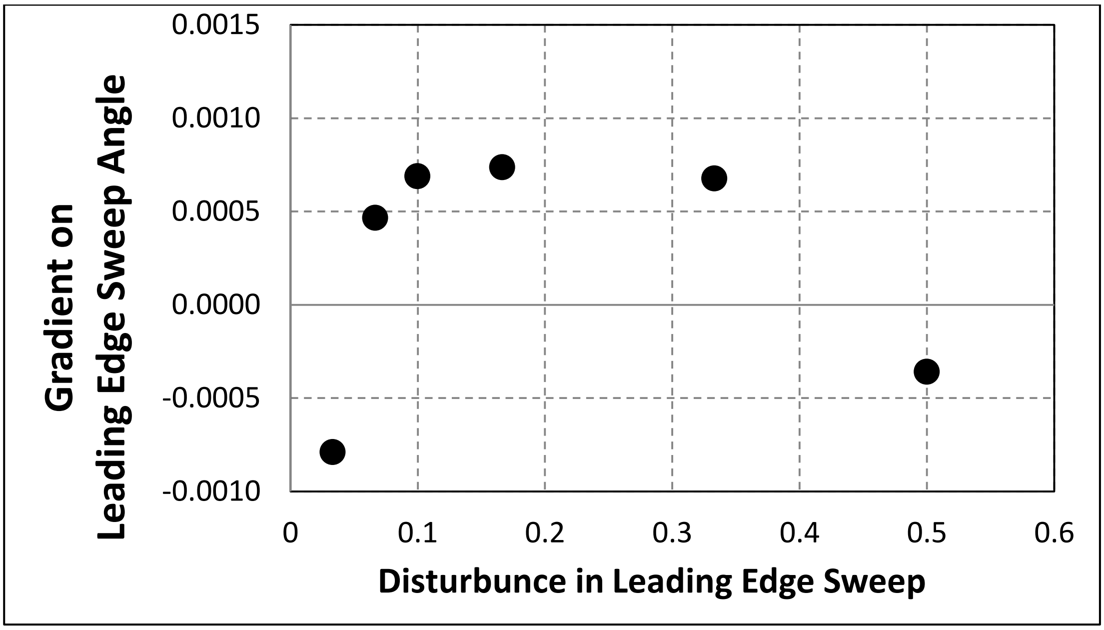


Figure 4-2 Effect of Leading Edge Sweep Angle Disturbance on Gradient

Similarly the effect of the amount of disturbance in the tip chord length and the span length are represented in Figure 4-3 and Figure 4-4, respectively.

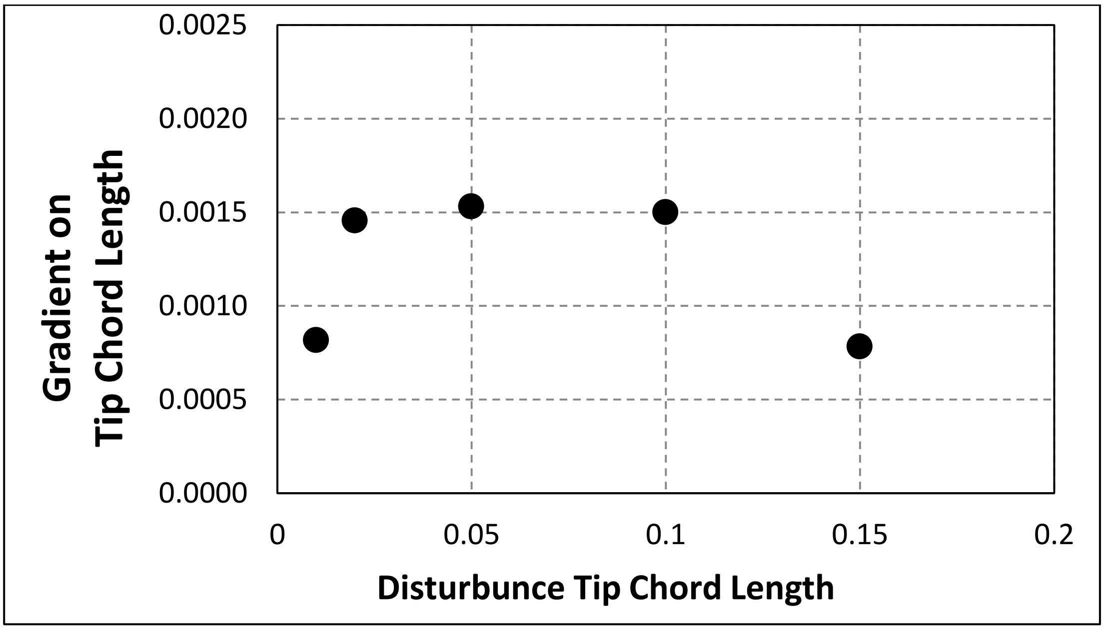


Figure 4-3 Effect of Tip Chord Length Disturbance on Gradient

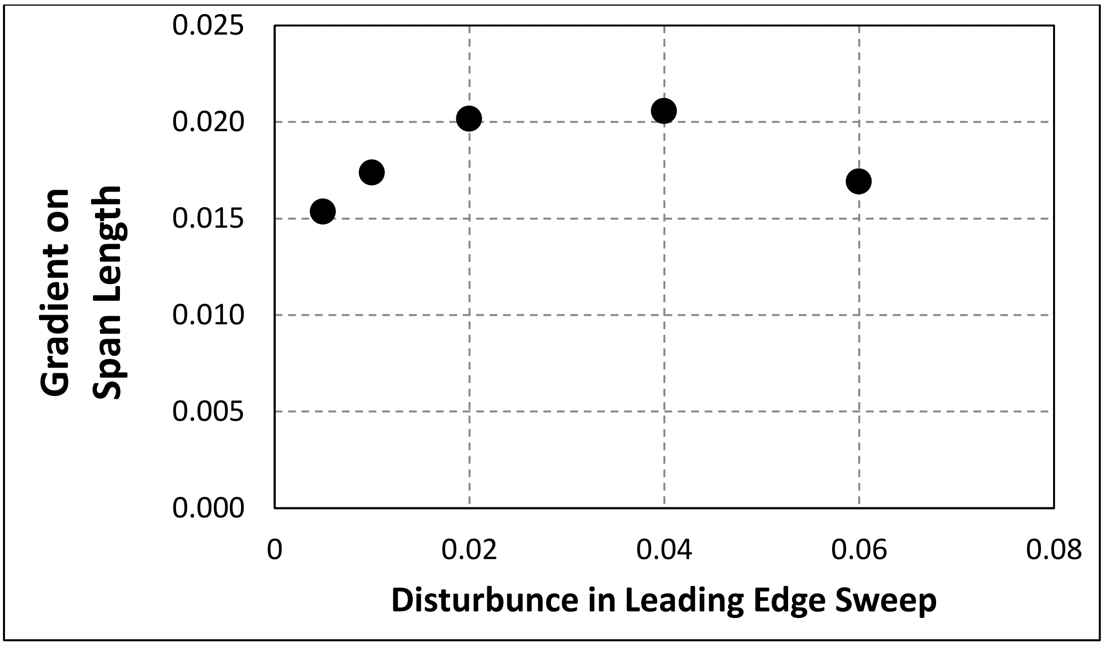


Figure 4-4 Effect of Span Length Disturbance on Gradient

From the figures it can be said that the disturbance in tip chord length should be between 0.05 and 0.1, and the disturbance in span length should be between 0.02 and 0.04. Throughout the optimization process these limits are taken into account.

First optimization step is represented in Table 4-2. The geometry number is notated such that 'G' means 'geometry', 'P' means 'parameter number' and 'S' means 'scale number in gradient direction'.

Table 4-2 Gradient Vector Calculation for Optimization Step 1

| Optimization Step 1 | | | | | | | | | |
|---|---|---|---|---|---|---|---|---|---|
| | **Geo** | **Delta** | **$\Lambda_{LE}$** | **Ctip** | **b** | **RPM** | **ΔCN (%)** | **OBJ** | **GRAD** |
| | **G0** | | 0.000 | 0.879 | 0.700 | 664.4 | 0.00 | **0.33222** | |
| **$\Lambda_{LE}$** | **G1-P1** | 0.333 | 0.333 | 0.879 | 0.700 | 660.0 | -0.37 | **0.32998** | 0.000676 |
| **Ctip** | **G1-P2** | 0.100 | 0.000 | 0.979 | 0.700 | 654.5 | 1.82 | **0.32724** | 0.001500 |
| **b** | **G1-P3** | 0.040 | 0.000 | 0.879 | 0.740 | 609.8 | 2.83 | **0.30491** | 0.020552 |

After obtaining the gradient vector from the change in objective function for the disturbed geometries, set of analyses are performed in this gradient direction to determine the biggest step size in this direction. For an example, the line search algorithm of the first step in optimization process is shown in Figure 4-5.

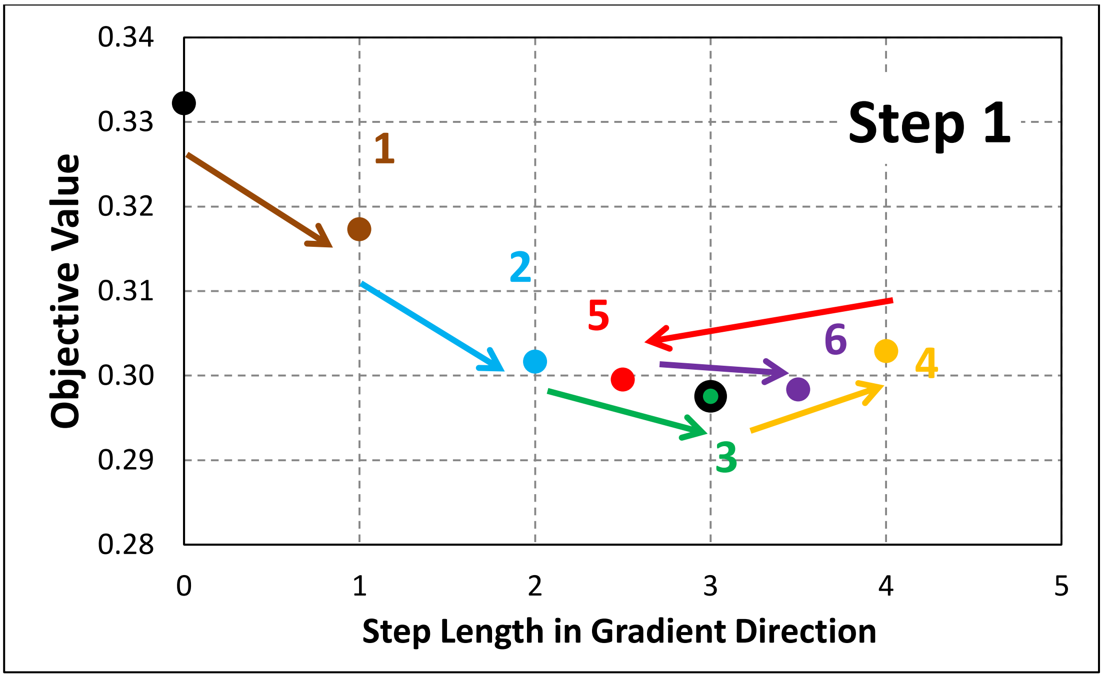


Figure 4-5 Line Search in Gradient Direction for Optimization Step 1

Firstly, step lengths of 1, 2, 3 and 4 are analyzed and the objective values are represented. It is seen that objective value is decreasing throughout the points 1, 2 and 3. However, the objective value increases for the point 4. The point 5, the mid-point between point 2 and 3, is analyzed. Since the objective value at point 5 is still higher than the one of point 3; the point 6, the mid-point between point 3 and 4, is analyzed. The objective value at point 6 is still higher and it can be said that the maximum step length is 3.The geometry obtained from the first optimization step is G1-S3 since the minimum objective value is obtained by applying 3 step length in gradient direction. Geometry G1-S3 is the geometry which is going to be disturbed in the second optimization step. The gradient calculations and line search procedure are repeated until the objective value is converged. The gradient vector calculations and line search studies for other optimization steps are given in Appendix A.

The parameters at the last optimization step are represented in Table 4-3.

Table 4-3 Optimum Geometry at Optimization Step 6

| Geo | $\Lambda_{LE}$ | Ctip | b | RPM | $\Delta C_N$ (%) | OBJ |
|---|---|---|---|---|---|---|
| **G6-S6** | 0.466 | 0.683 | 0.854 | 485.2 | 4.32 | **0.26002** |

The geometrical change in the shape of tail fin compared with initial tail fin is represented in Figure 4-6.

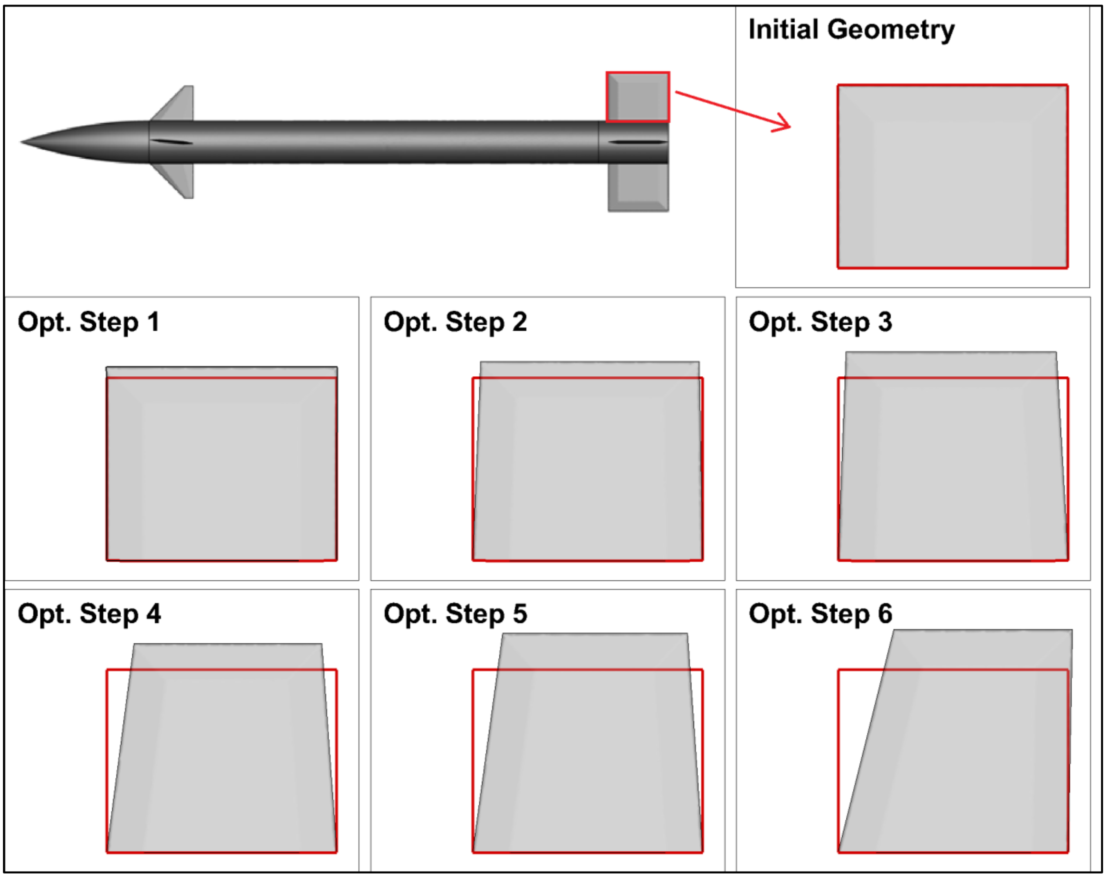


Figure 4-6 Tail Fin Planform Shapes throughout Optimization Steps

The optimum tail fin geometry is compared with the tail fin at test case and initial tail fin in Figure 4-7.

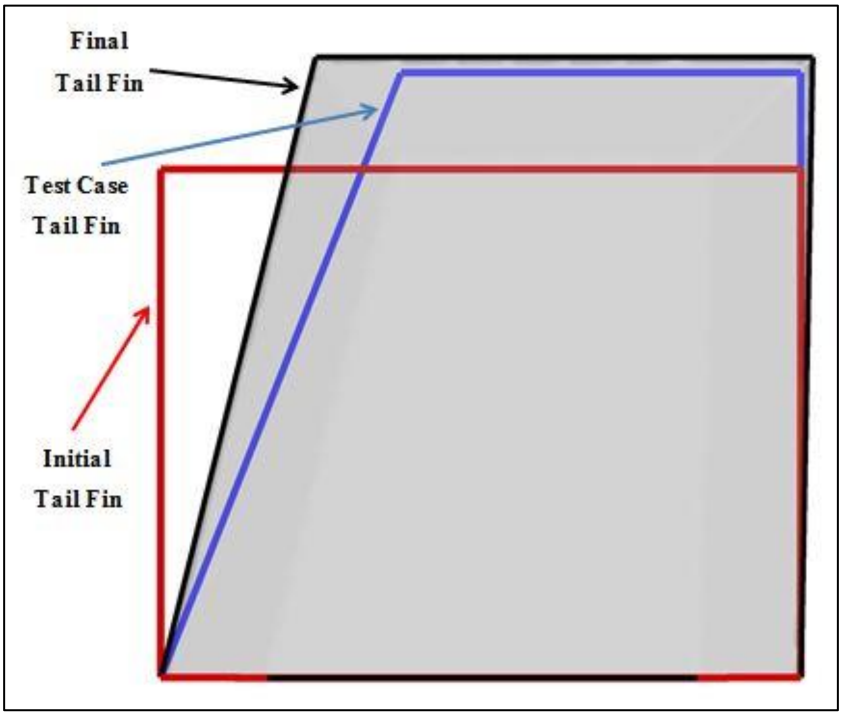


Figure 4-7 Comparison of Tail Fin Model with Test Case Tail Fin Model

The objective values throughout the optimization steps are represented in Figure 4-8. Since the objective value at the fifth and sixth optimization steps are close, the optimization process assumed to be converged and terminated. After six optimization steps, the objective value is decreased by 22% compared to the initial rectangular tail fin geometry as seen in Figure 4-8.

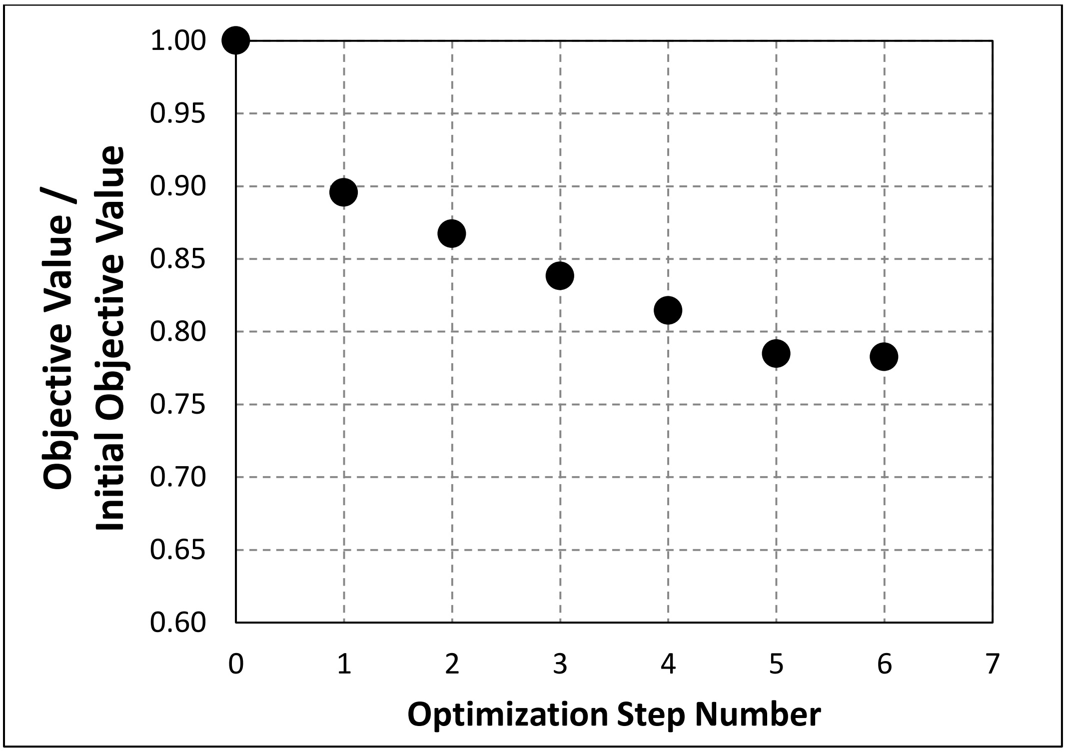


Figure 4-8 Objective Values at the Optimization Steps

Objective function includes the effects of both the roll rate of the tail fins and the change in the normal force. The roll rate values (divided by initial value) of the tail fins at the six optimization steps are represented in Figure 4-9. It can be seen that the roll rate of the tail fins is decreased by 27% compared to the initial rectangular tail fin geometry. And the normal force (divided by initial value) of the model at the six optimization steps are represented in Figure 4-10. It can be seen that the normal force is increased by approximately 4.5% compared to the initial rectangular tail fin geometry and M-TCM test case geometry.

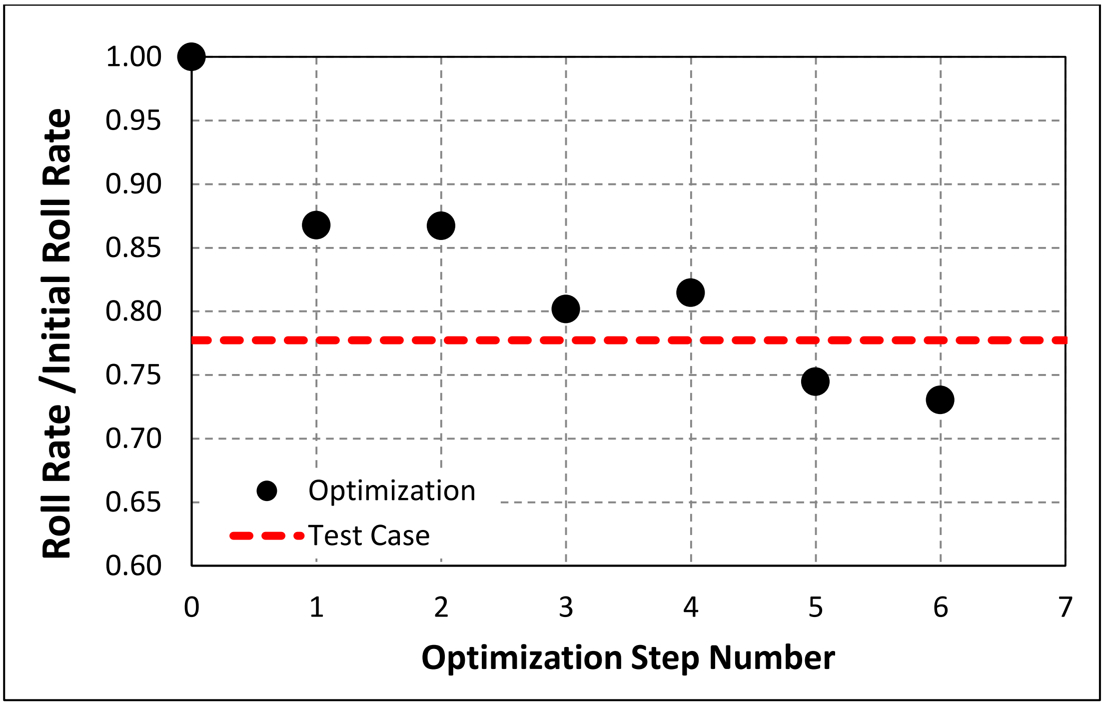


Figure 4-9 Roll Rate Values of Tail Fins at the Optimization Steps

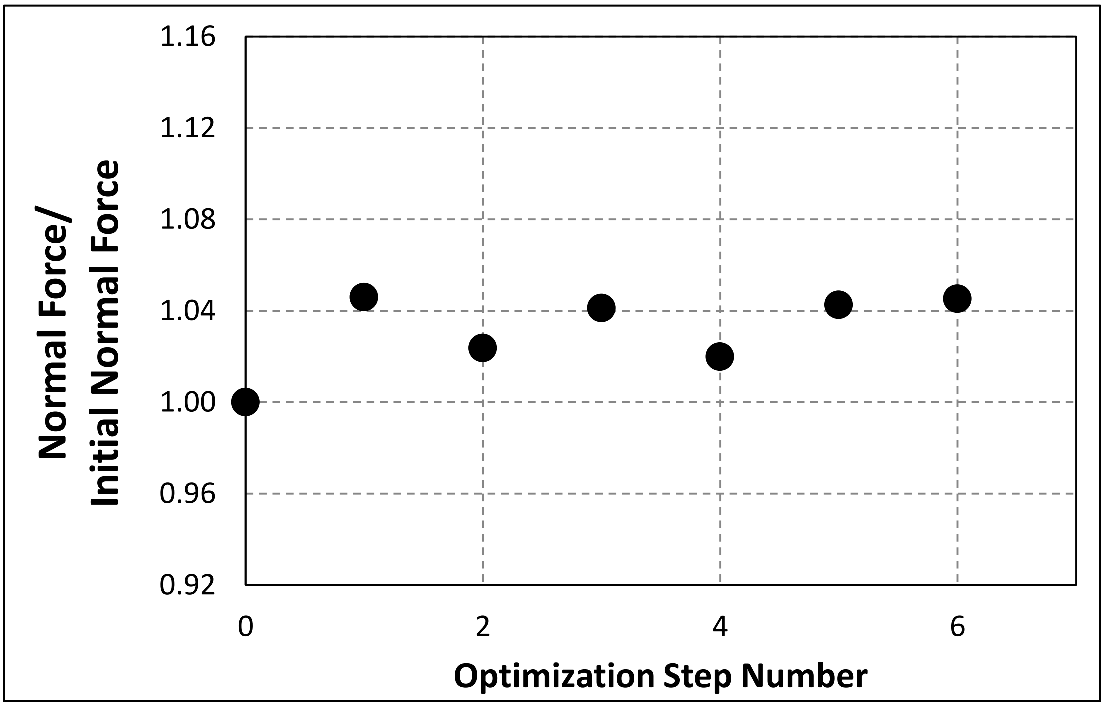


Figure 4-10 Normal Force Values of Tail Fins at the Optimization Steps

The axial force coefficients of the models are calculated throughout the optimization steps. The axial force coefficients are given in Figure 4-11. It can be seen in the figure that the axial force coefficient values are lower than the one of M-TCM test case model. The change in the moment of inertia value is shown in Figure 4-12.

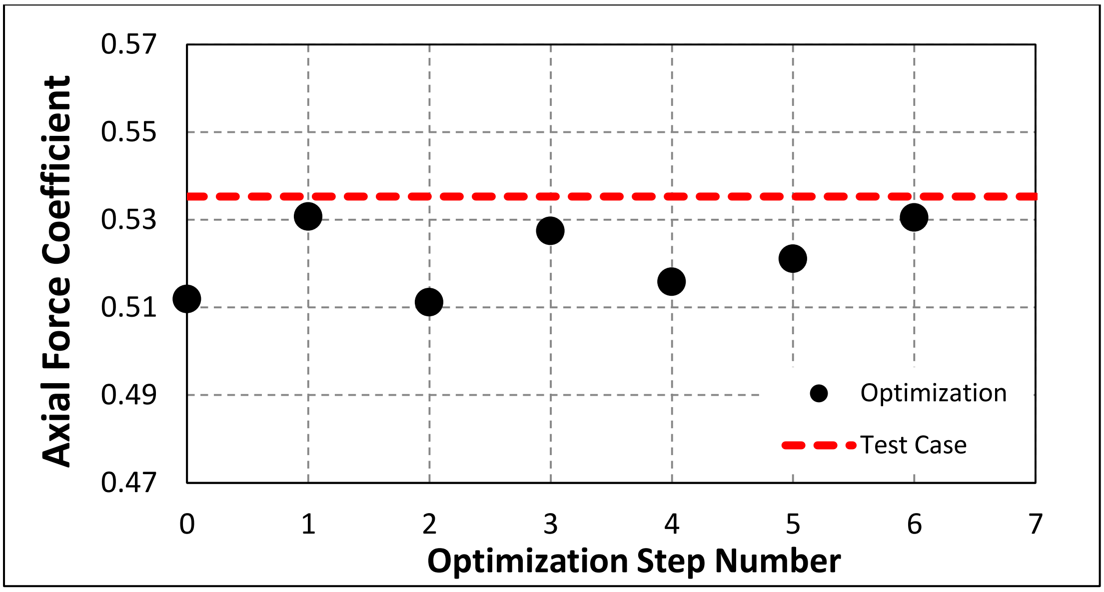


Figure 4-11 Axial Force Coefficient Values of Tail Fins at the Optimization Steps

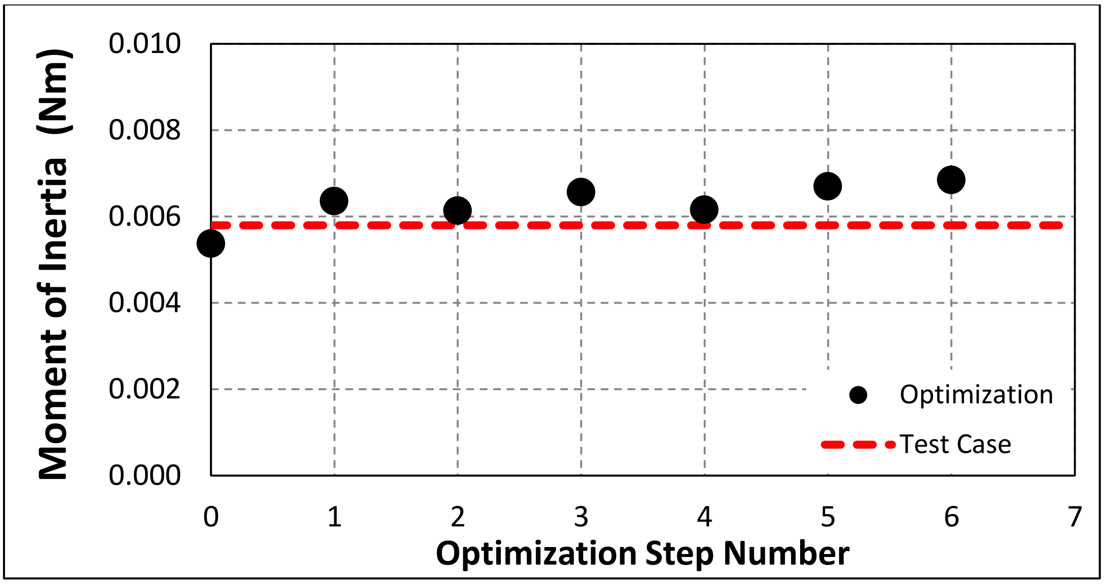


Figure 4-12 Moment of Inertia Values of Tail Fins at the Optimization Steps

The change in geometric parameters of the tail fins throughout the optimization steps are represented in Figure 4-13, Figure 4-14, Figure 4-15 and Figure 4-16.

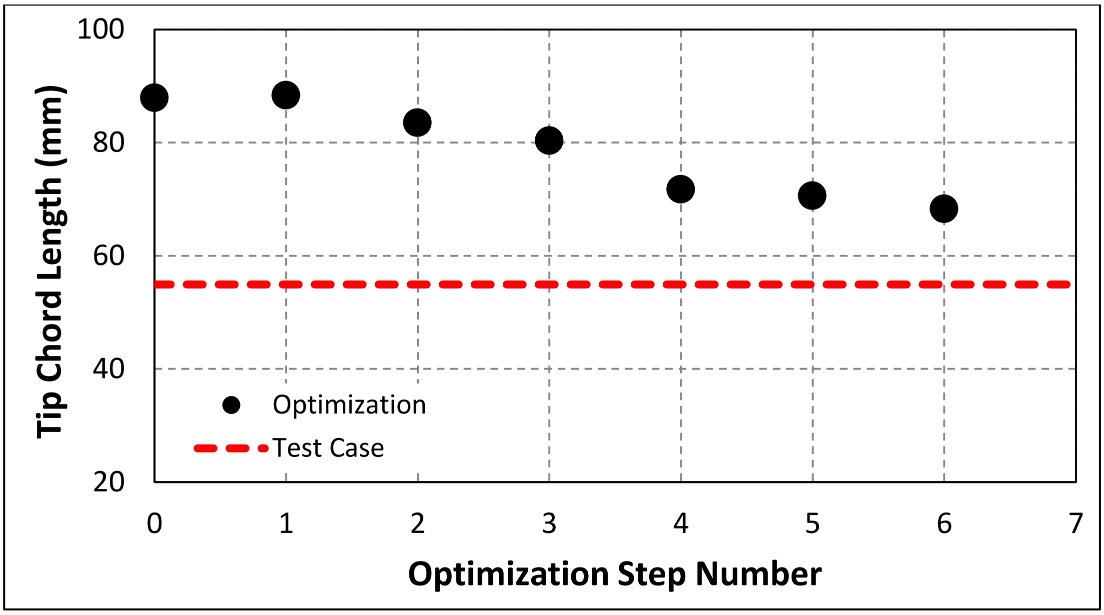


Figure 4-13 Change in Tip Chord Length at the Optimization Steps

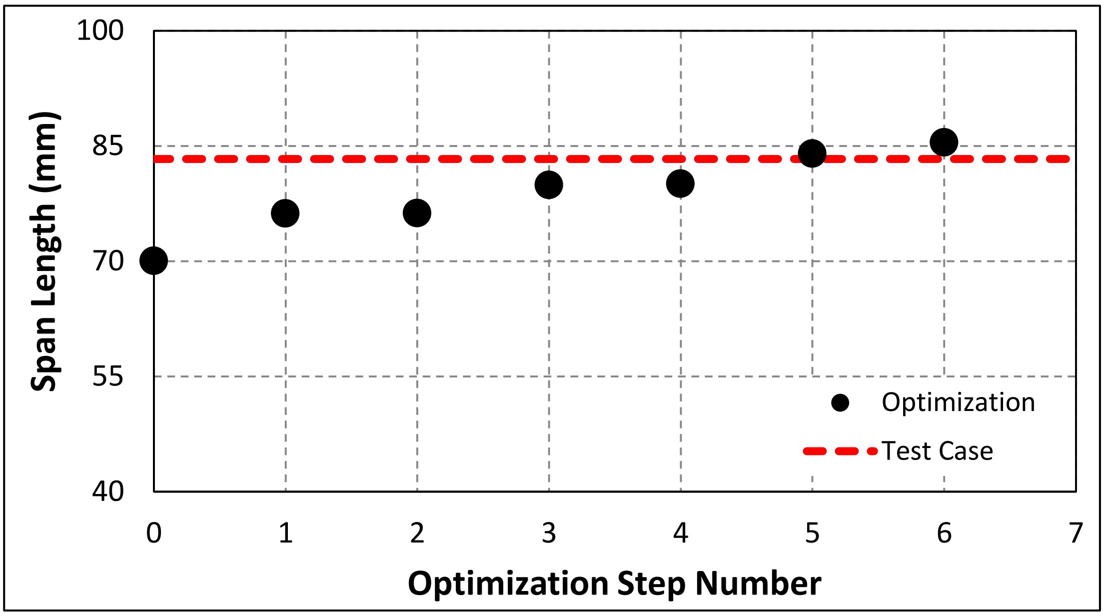


Figure 4-14 Change in Tip Chord Length at the Optimization Steps

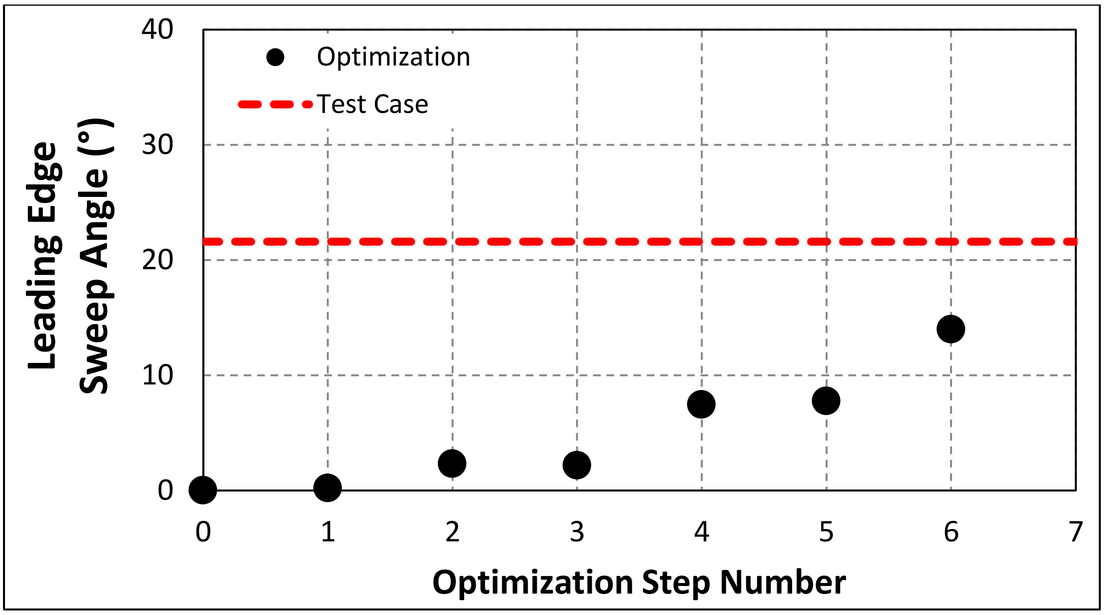


Figure 4-15 Change in Leading Edge Sweep Angle at the Optimization Steps

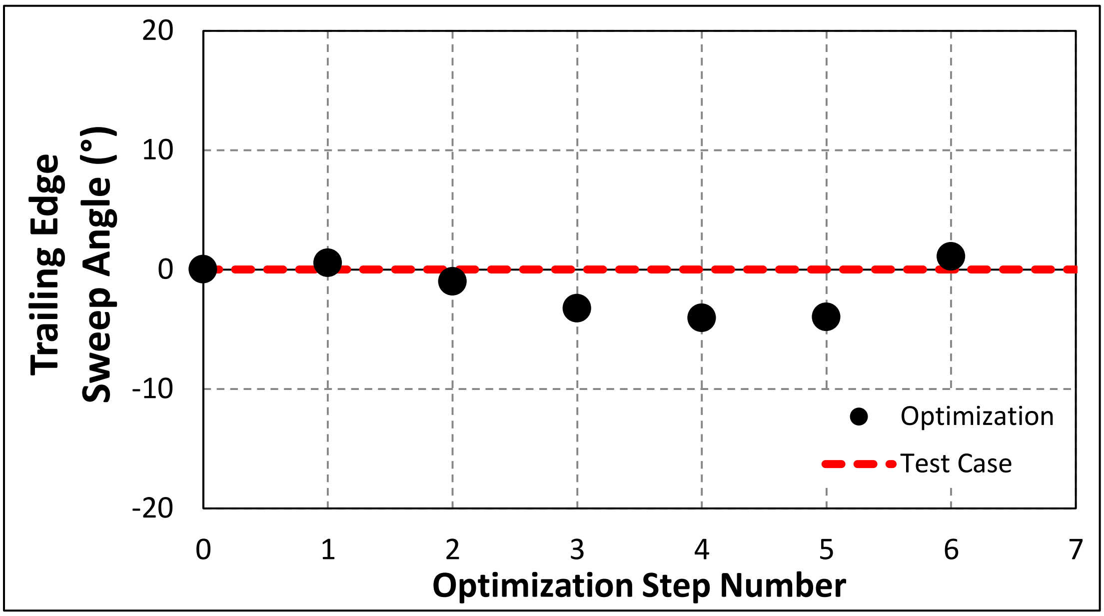


Figure 4-16 Change in Leading Edge Sweep Angle at the Optimization Steps

From the figures it can be seen that the geometric parameters approach to the one of M-TCM test case. It is most possible that in the design of the tail fins in M-TCM the interaction between canard fin and tail fin is taken into account.

The convergence histories of the roll rate of the free-to-rotate tail fins for the initial, optimum and test case model are represented in Figure 4-17.

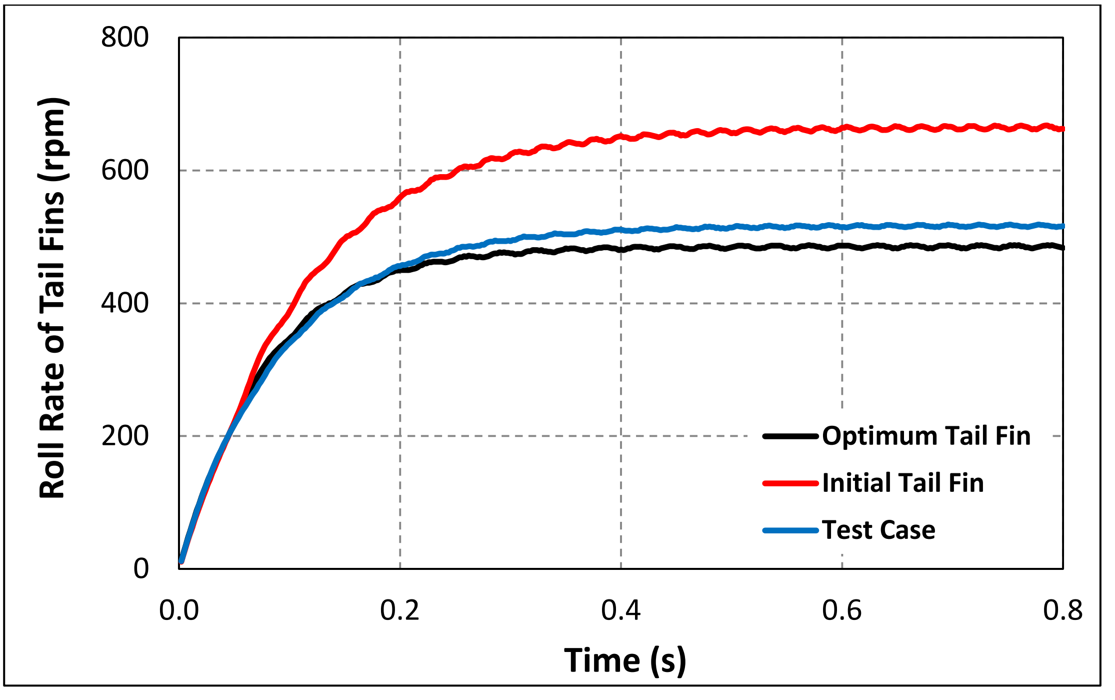


Figure 4-17 Convergence History of Roll Rate of Tail Fins

The roll motion of the tail fins repeats itself in 90° - period. The roll orientation of the initial and optimum tail fins in 90 ° - periods is represented in Figure 4-18.

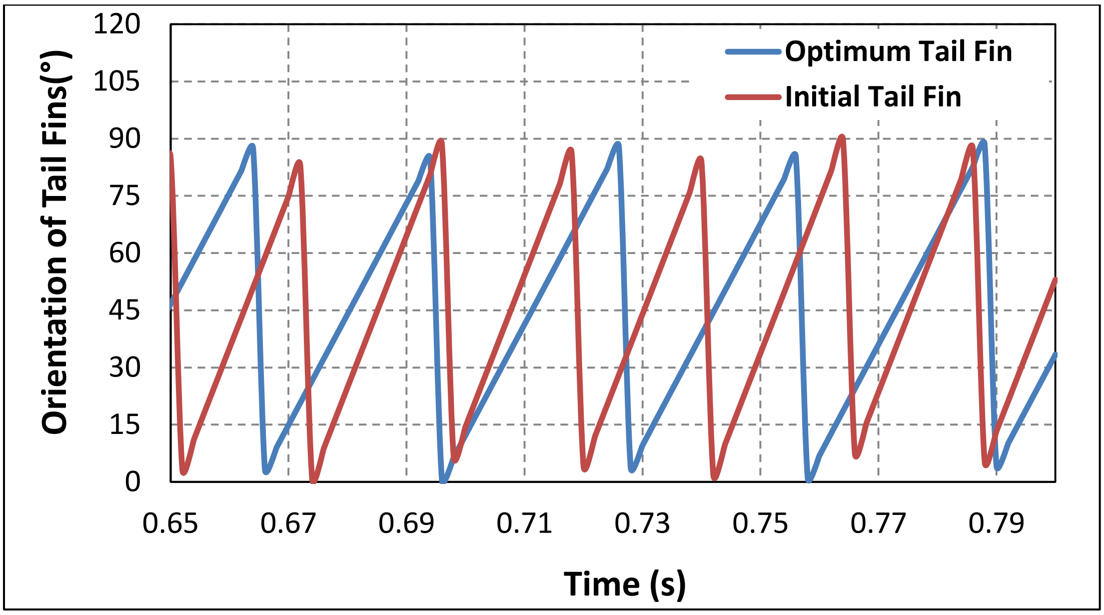


Figure 4-18 Roll Orientation of Tail Fins

It can be seen in the figure that the frequency of the roll motion of the optimum tail fins is larger than the one of the initial tail fins. This means that the roll rate of the optimum tail fins is lower than the one of the initial tail fins.

## 4.4 Steady and Unsteady Flow Field Visualizations

In this part, some steady and unsteady flow visualizations are represented for the flow around the initial and optimum tail fins. Steady flow visualizations are performed to investigate the asymmetric flow generated by the canard fins. Since the flow is supersonic tail fins do not affect the region between the nose and tail fins. Therefore, the flow field up to tail fins is same for M-TCM test case model, initial model with rectangular tail fins and the final model with optimum tail fins. The steady flow visualizations are represented for the model with optimum tail fins.

### 4.4.1 Mach Number Contour for Steady Flow

Mach number contour around the missile in the pitch plane is shown in Figure 4-19. Mach number contour around the canard and tail fin in the plane with a 0.85 missile-diameter offset to the pitch plane is shown in Figure 4-20.

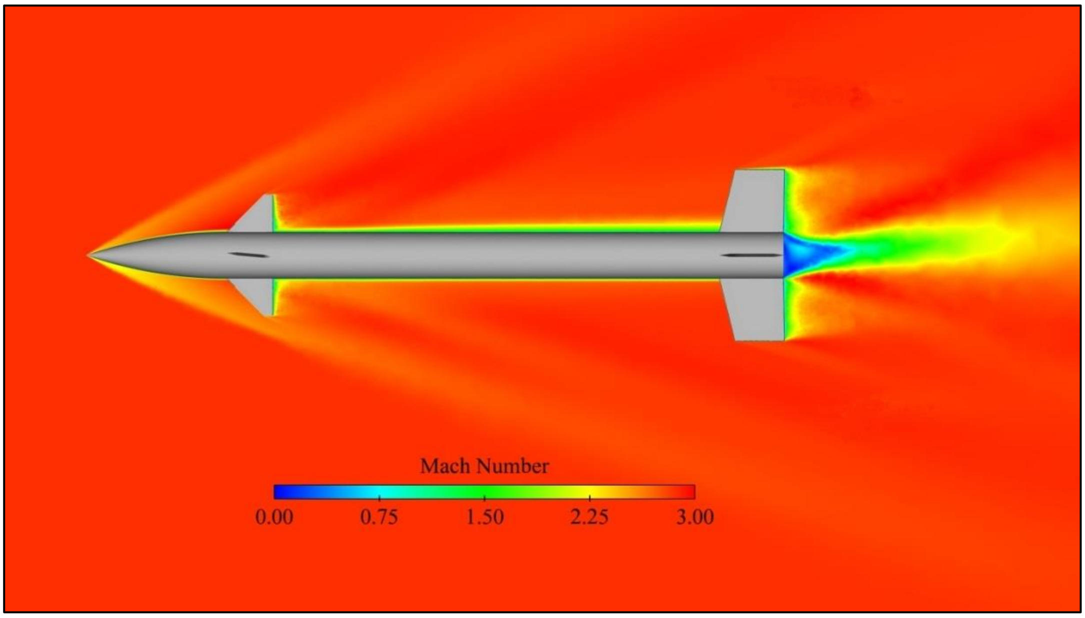


Figure 4-19 Mach Number Contour around the Missile with Optimum Tail Fin

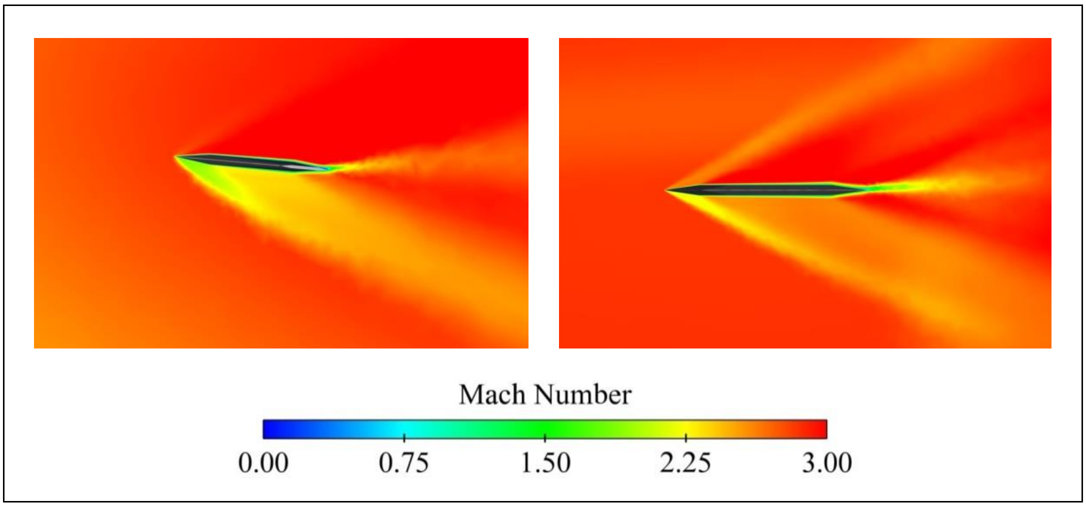


Figure 4-20 Mach Number Contour around Canard (left) and Tail (right)

### 4.4.2 Total Pressure and Vorticity Contour for Steady Flow

Due to the aileron deflection on canard fins, asymmetric flow field develops around the missile. The equivalent angle of attack of the right canard fin when viewed from the nose is larger than the equivalent angle of attack of the left canard fins. This leads to stronger vortices generate from the right canard fin. The vortices can be seen from the total pressure and vorticity contours. The total pressure contour around the missile body is shown in Figure 4-21 and the vorticity contour around the missile body is shown in Figure 4-22. The asymmetric flow due to the vortices generated by canard fins is seen in the figures.

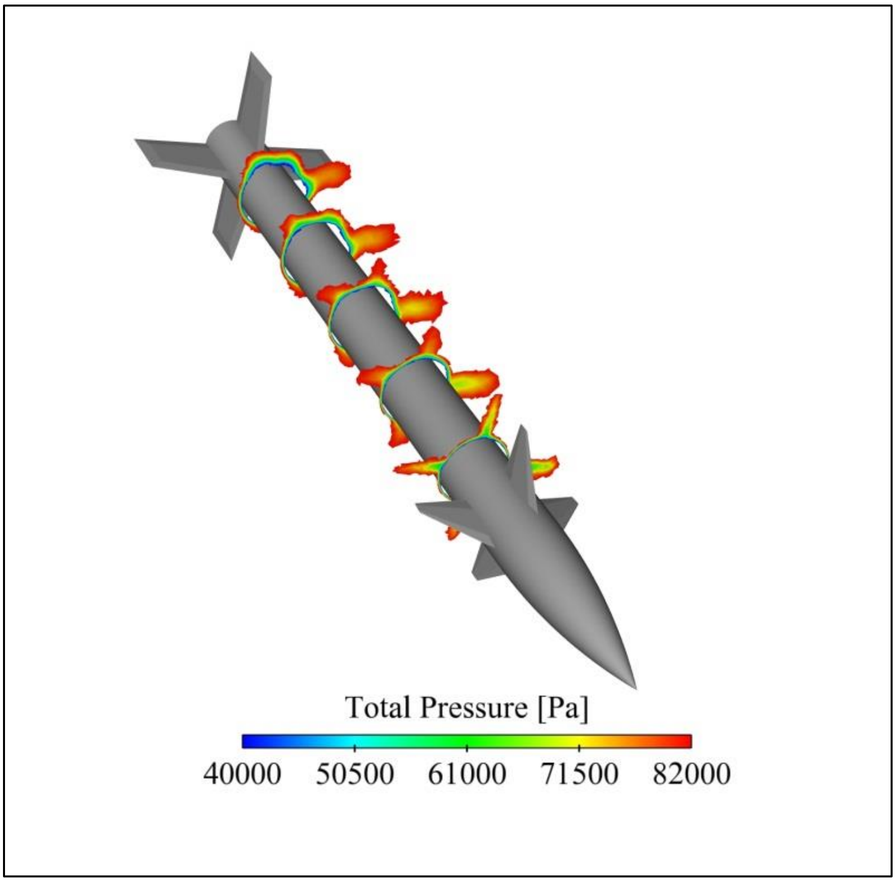


Figure 4-21 Total Pressure Contour around Missile Body

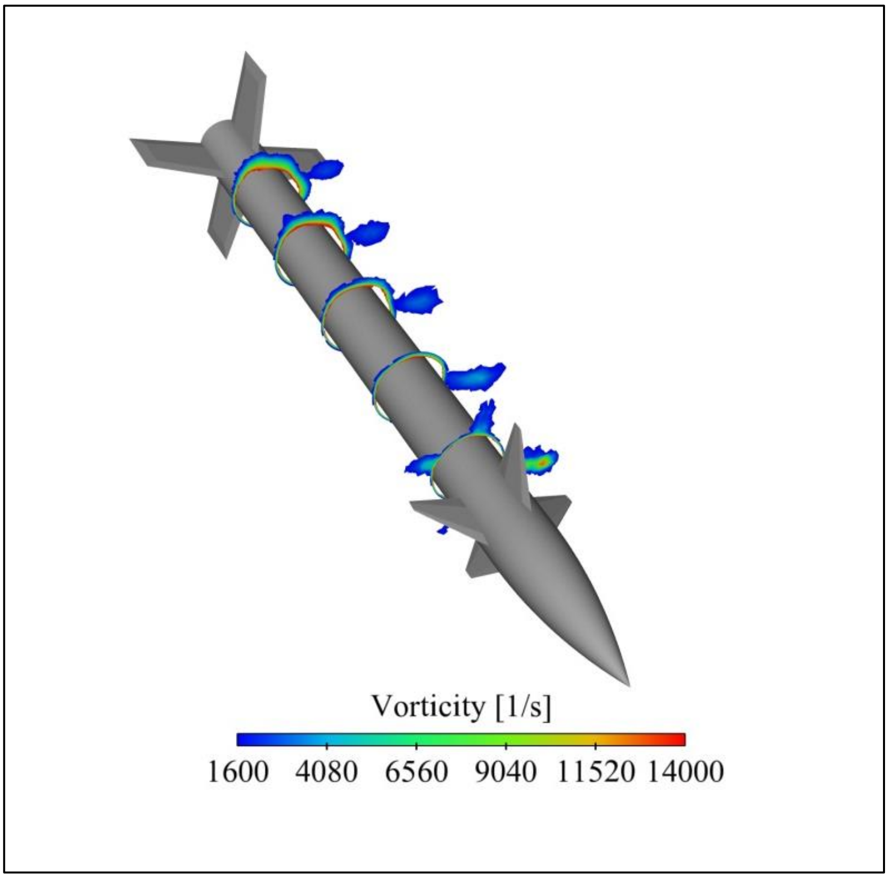


Figure 4-22 Vorticity Contour around Missile Body

### 4.4.3 Total Pressure around Tail Fins for Unsteady Flow

In order to compare the flow fields for the initial rectangular tail fins and optimum tail fins, the solutions at the time of 0.782 are chosen since at this time the tail fin orientations for the initial and optimum models are same as seen in Figure 4-23. Around the tail fins the flow visualizations are performed at the location of 63% of the root chord from the leading edge of the tail fins.

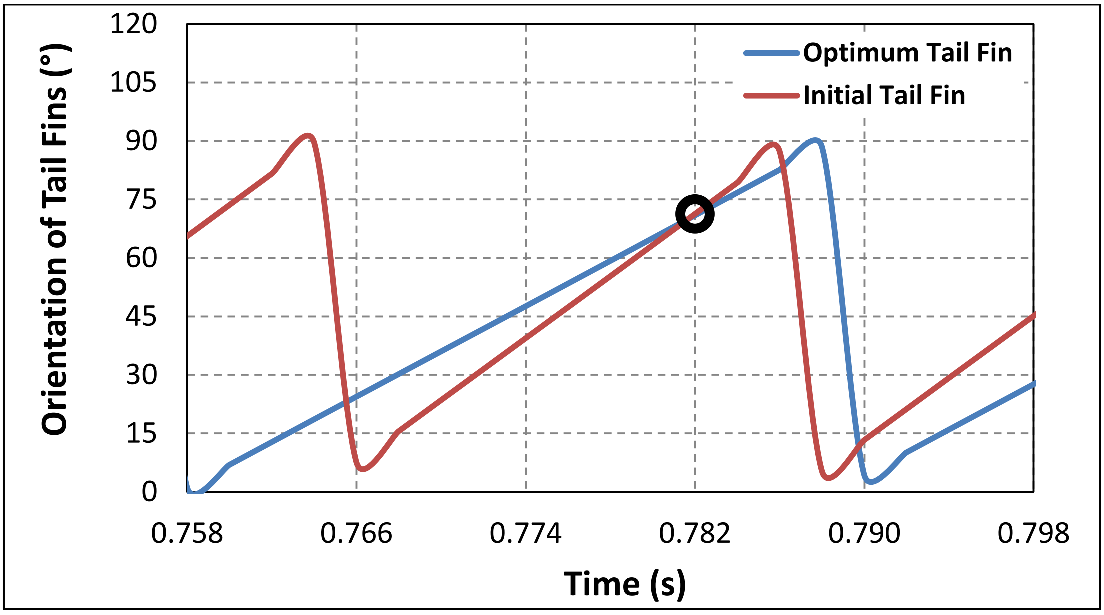

Figure 4-23 Roll Orientations for Initial and Final Tail Fins

At the time of 0.782 s the comparison of the total pressure contours for the initial and optimum tail fin geometries (when viewed from the nose) is represented in Figure 4-24. It can be said from the figure that the vortices generated by the right canard fin when viewed from the nose create larger vortices on the tail tips.

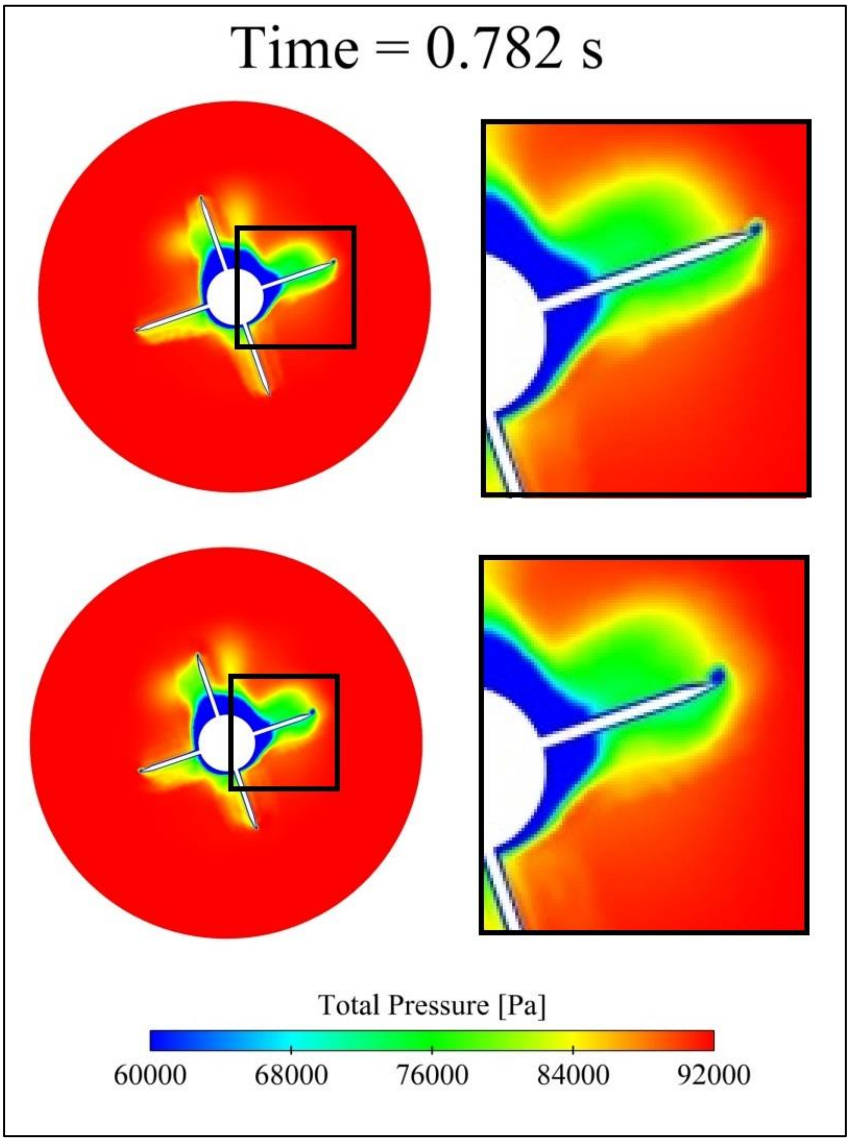


Figure 4-24 Total Pressure Contours of Optimum (top) and Initial (bottom) Tail Fins

### 4.4.4 Streamlines around Tail Fins for Unsteady Flow

For the time interval from 0.758 to 0.786 s, a 90° - period of rotation of the tail fins, the total pressure contours and streamlines around the optimum tail fin geometry are represented in Figure 4-25.

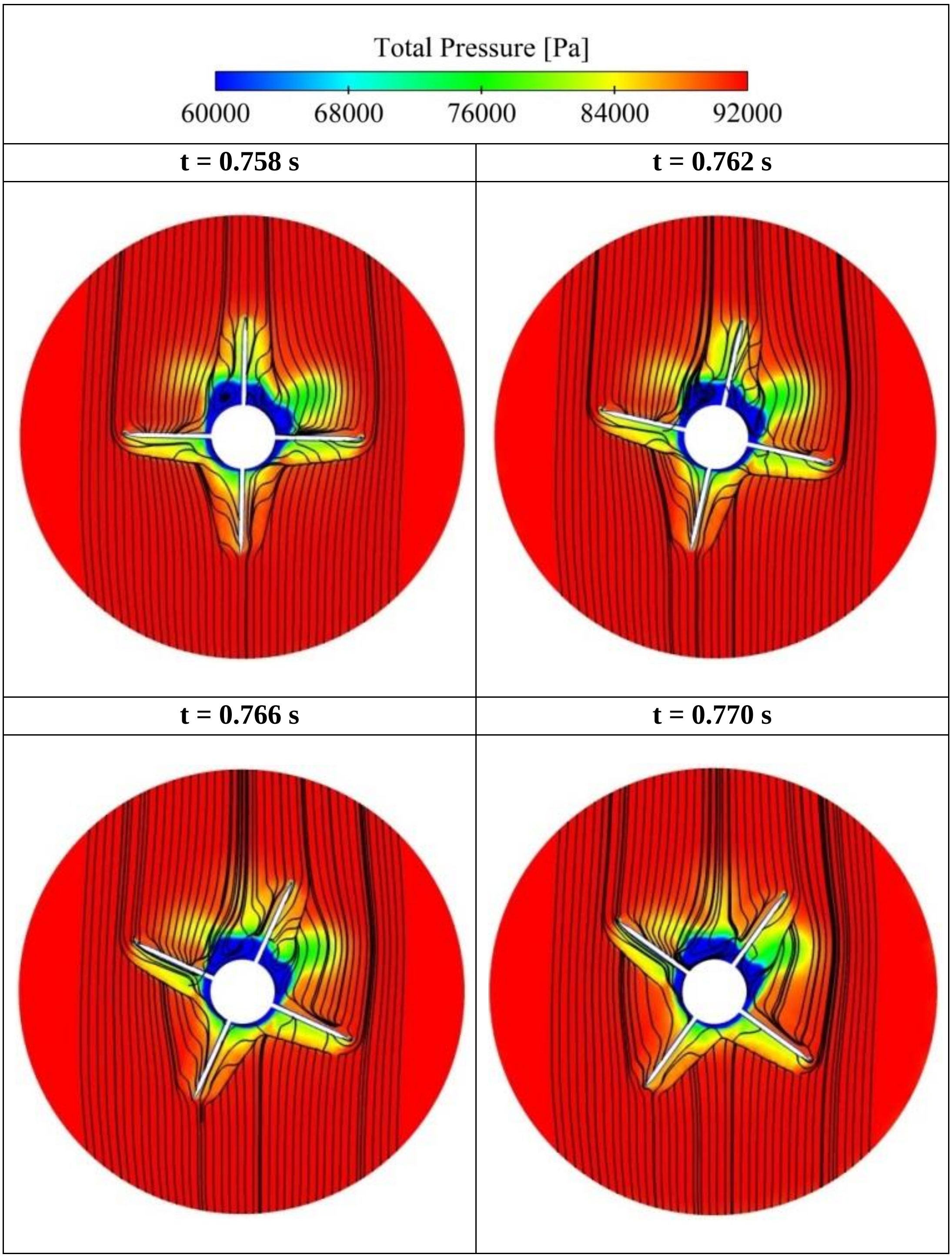


Figure 4-25 Streamlines and Total Pressure Contours around Optimum Tail Fins

| **t = 0.774 s** | **t = 0.778 s** |
|---|---|
| 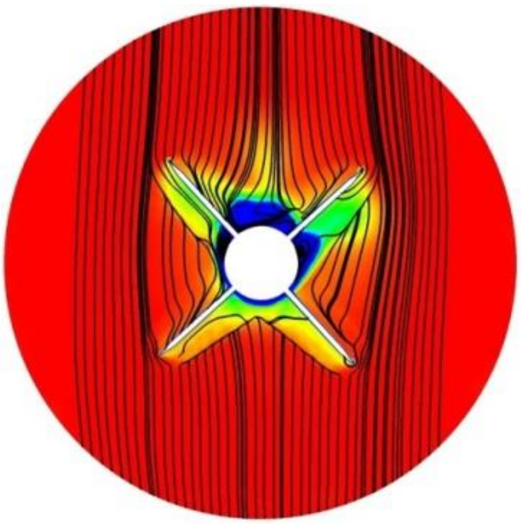 | 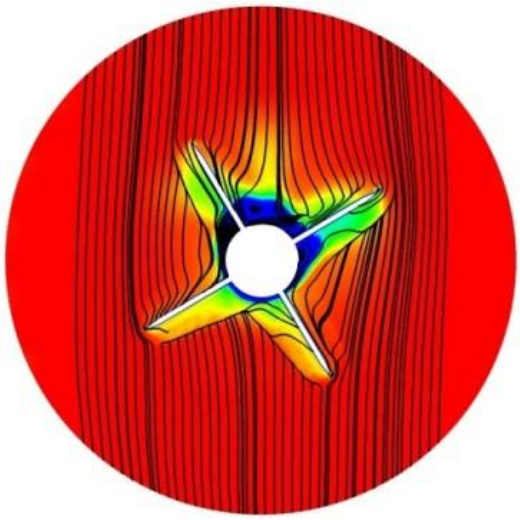 |
| **t = 0.782 s** | **t = 0.786 s** |
| 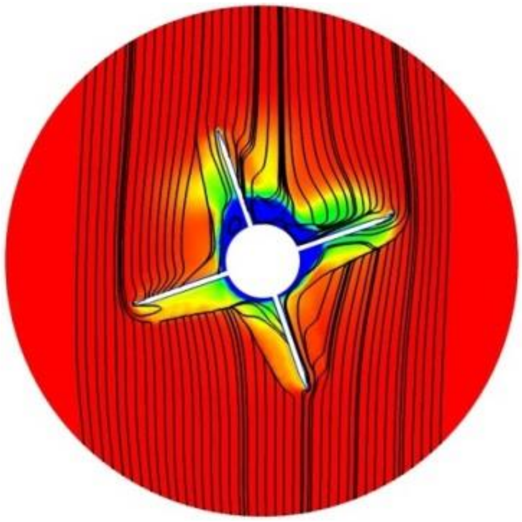 | 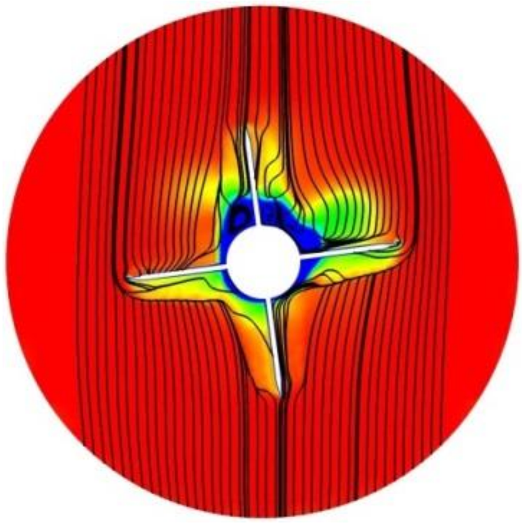 |

Figure 4-25 (continued)

### 4.4.5 Vector Field around Tail Fins for Unsteady Flow

The vector field visualization of the optimum and initial tail fins (when viewed from the back) is represented in Figure 4-26. Similar to total pressure contour the tip vortex region in the optimum tail fin is smaller compared to the one of the initial tail fin.

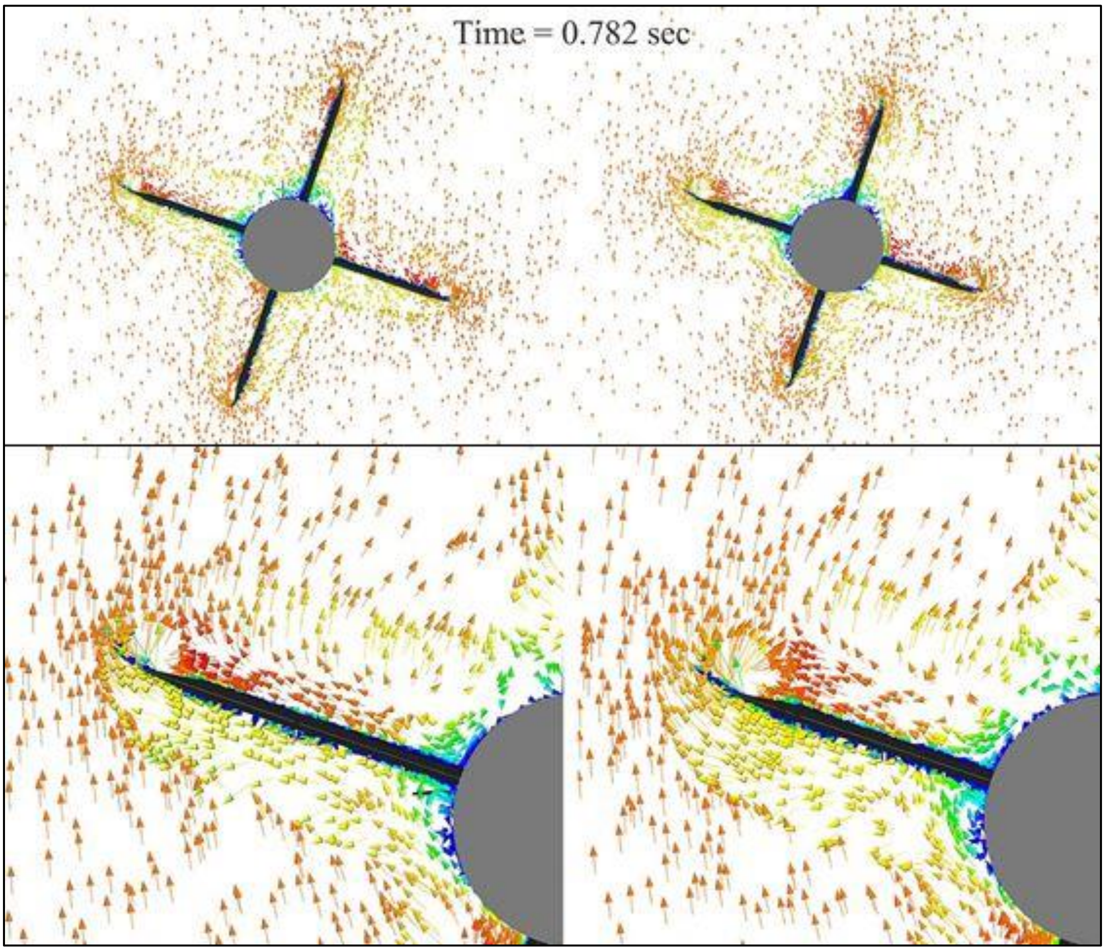


Figure 4-26 Vector Field around Optimum (left) and Initial (right) Tail Fins

# CHAPTER 5

# CONCLUSIONS

In the design process of a canard-controlled missile, the induced roll motion should be taken into account by the designers. In this study, the induced roll characteristics and shape optimization with gradient based method of the free-to-rotate tail fins on a canard controlled missile are investigated. Free-to-rotate tail fin configuration, which is a solution to induced roll problem, is analyzed by RANS solutions and compared with the wind tunnel test data for which are available. The numerical results obtained for two validation cases are, in general, in agreement with wind tunnel data. The roll rates of the tail fin are under predicted by about 8% for the M-TCM test case and 13% for TCM test case, which fall into the 25 rpm uncertainty level of the experimental data.

In the second part of this study, a planform optimization is performed in order to minimize the roll rate of the free-to-rotate tail fins. A gradient based optimization method is used with a discrete line search algorithm. The planform of the free-to-rotate tail fins is optimized successfully starting with a rectangular planform having same lift-curve slope with M-TCM test case model. The optimum tail fin planform reduces the roll rate of the tail fins by about 27% compared to the initial rectangular tail fin and by about 6% compared to the tail fin of M-TCM model. The normal force increases by about 4% without reduction in axial force.

# REFERENCES


[1] T. A. Nygaard, "Aeromechanic Analysis of a Missile with Freely Spinning Tailfins," in *AIAA Applied Aerodynamics Conference*, Orlando, 2003.

[2] L. M. Auman and R. E. Kreeger, "Aerodynamic Charactersitics of a Canard-Controlled Missile with a Free-Spinning Tail," U.S. Army Aviation and Missile Command, Alabama, 1997.

[3] M. A. McDaniel and C. Evans, "The Effect of Tail Fin Parameters on the Induced Roll of Canard-Controlled Missile," in *28th AIAA Applied Aerodynamics Conference*, Chicago, 2010.

[4] A. B. Blair, "Wind-Tunnel Investigation at Supersonic Speeds of a Canard-Controlled Missile With Fixed and Free-Rolling Tail Fins," Langley Research Center, Virginia, 1978.

[5] A. B. Blair, J. M. Allen and G. Hernandez, "Effect of Tail-Fin Span on Stability and Control Characteristics of a Canard-Controlled Missile at Supersonic Mach Numbers," Langley Researc Center, Virginia, 1983.

[6] A. B. Blair, "Wind-Tunnel Investigation at Supersonic Speeds of a Remote-Controlled Canard Missile With a Free-Rolling-Tail Brake Torque System,"

NASA, Virginia, 1985.

[7] D. Lesieutre, J. Love and M. Dillenius, "Prediction of the Nonlinear Aerodynamic Characteristics of Tandem-control and Rolling-tail Missiles," in *AIAA Atmospheric Flight Mechanics Conference*, Monterey, 2002.

[8] S. M. Murman and M. J. Aftosmis, "Cartesian-Grid Simulations of a Canard-Controlled Missile with a Spinning Tail," in *AIAA Applied Aerodynamics Conference*, Orlando, 2003.

[9] A. Inc., *Ansys Fluent User's Guide*, 2011.

[10] İ. B. Celik, "Introductory Turbulence Modeling," West Virginia University, Morgantown, 1999.

[11] R. M. Freund, "The Steepest Descent Algorithm for Unconstrained Optimization and a Bisection Line-Search Method," Massachusetts Institute of Technology, 2004.

[12] S. Corporation, *SolidWorks 97Plus User's Guide*, 1997.

[13] R. R. Heisler and C. L. Ratliff, "Wind Tunnel Model Design and Test Using Rapid Prototype Materials and Processes," The Johns Hopkins University Applied Physic Laboratory, Laurel, 2001.

## APPENDIX A

## OPTIMIZATION STEPS

The second optimization step is represented in Table A-1.

Table A-1 Gradient Vector Calculation for Optimization Step 2

| Optimization Step 2 | | | | | | | | | |
|---|---|---|---|---|---|---|---|---|---|
| | **Geo** | **Delta** | **$\Lambda_{LE}$** | **Ctip** | **b** | **RPM** | **$\Delta C_N$ (%)** | **OBJ** | **GRAD** |
| | **G1-S3** | | 0.007 | 0.883 | 0.762 | 576.5 | 4.39 | 0.29754 | |
| **$\Lambda_{LE}$** | **G2-P1** | 0.133 | 0.140 | 0.883 | 0.762 | 578.4 | 3.59 | 0.29336 | 0.003518 |
| **Ctip** | **G2-P2** | 0.050 | 0.007 | 0.933 | 0.762 | 572.9 | 5.52 | 0.30964 | -0.008133 |
| **b** | **G2-P3** | 0.030 | 0.007 | 0.883 | 0.792 | 541.9 | 5.71 | 0.29749 | 0.000054 |

The line search process in the second optimization is represented in Figure A-1.

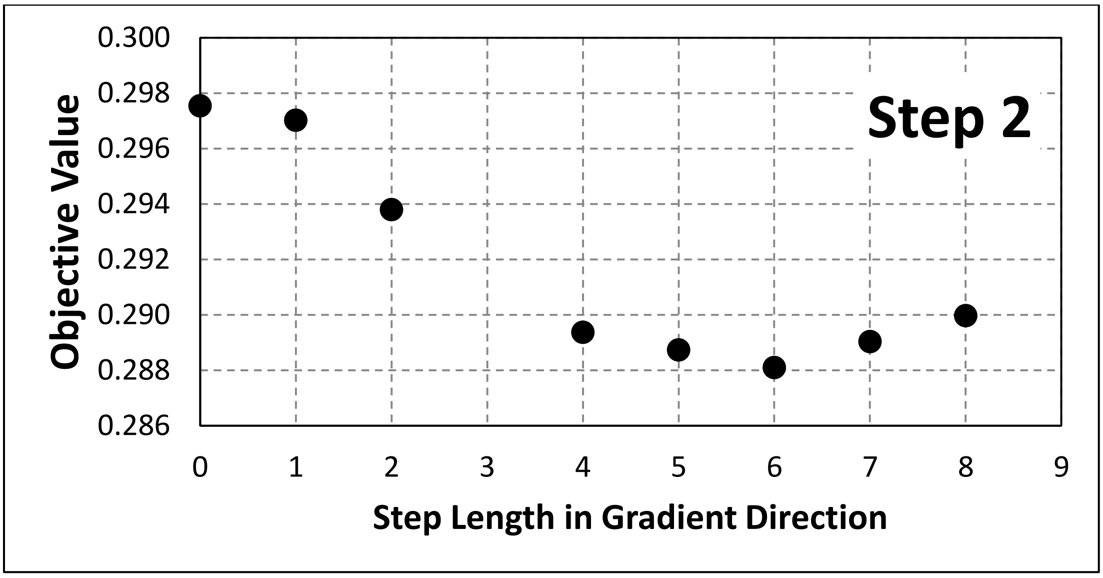


Figure A-1 Line Search in Gradient Direction for Optimization Step 2

The third optimization step is represented in Table A-2.

Table A-2 Gradient Vector Calculation for Optimization Step 3

| Optimization Step 3 | | | | | | | | | |
|---|---|---|---|---|---|---|---|---|---|
| | **Geo** | **Delta** | **$\Lambda_{LE}$** | **Ctip** | **b** | **RPM** | **$\Delta C_N$ (%)** | **OBJ** | **GRAD** |
| | **G2-S6** | | 0.077 | 0.835 | 0.762 | 576.2 | 2.31 | 0.28809 | |
| **$\Lambda_{LE}$** | **G3-P1** | 0.133 | 0.210 | 0.835 | 0.762 | 577.1 | 2.18 | 0.28853 | -0.000367 |
| **Ctip** | **G3-P2** | 0.040 | 0.077 | 0.875 | 0.762 | 581.3 | 4.06 | 0.29742 | -0.007834 |
| **b** | **G3-P3** | 0.030 | 0.077 | 0.835 | 0.792 | 543.3 | 4.26 | 0.27988 | 0.009202 |

The line search process in the third optimization is represented in Figure A-2.

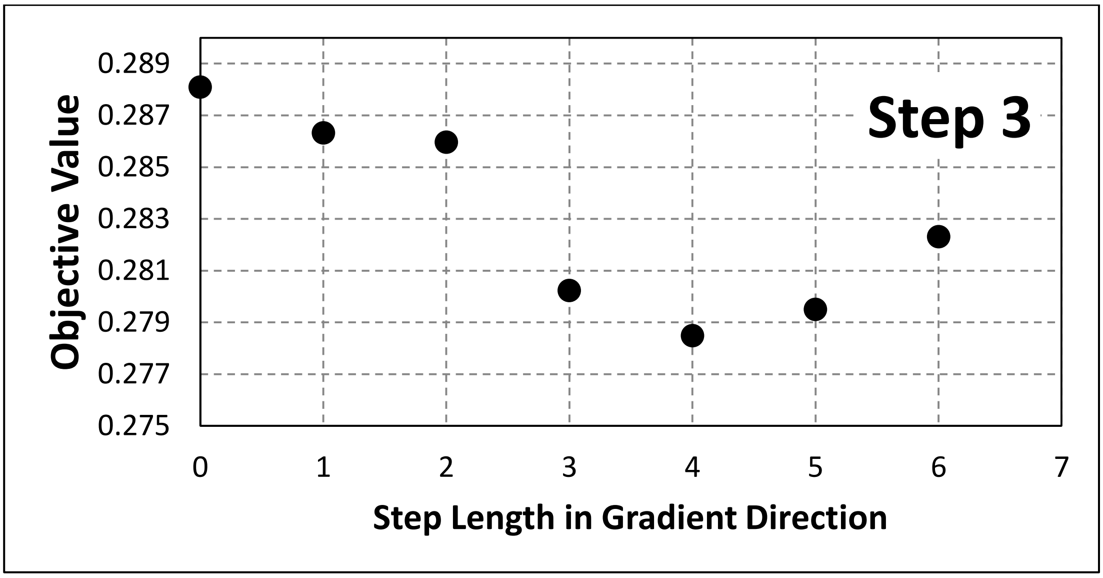


Figure A-2 Line Search in Gradient Direction for Optimization Step 3

The fourth optimization step is represented in Table A-3.

Table A-3 Gradient Vector Calculation for Optimization Step 4

| Optimization Step 4 | | | | | | | | | |
|---|---|---|---|---|---|---|---|---|---|
| | **Geo** | **Delta** | **$\Lambda_{LE}$** | **Ctip** | **b** | **RPM** | **$\Delta C_N$ (%)** | **OBJ** | **GRAD** |
| | **G3-S4** | | 0.072 | 0.803 | 0.799 | 532.7 | 3.95 | 0.27848 | |
| **$\Lambda_{LE}$** | **G4-P1** | 0.100 | 0.172 | 0.803 | 0.799 | 535.2 | 3.96 | 0.27378 | 0.005274 |
| **Ctip** | **G4-P2** | 0.030 | 0.072 | 0.833 | 0.799 | 536.1 | 5.19 | 0.28616 | -0.008599 |
| **b** | **G4-P3** | 0.030 | 0.072 | 0.803 | 0.829 | 494.7 | 5.93 | 0.27834 | 0.000164 |

The line search process in the fourth optimization is represented in Figure A-3.

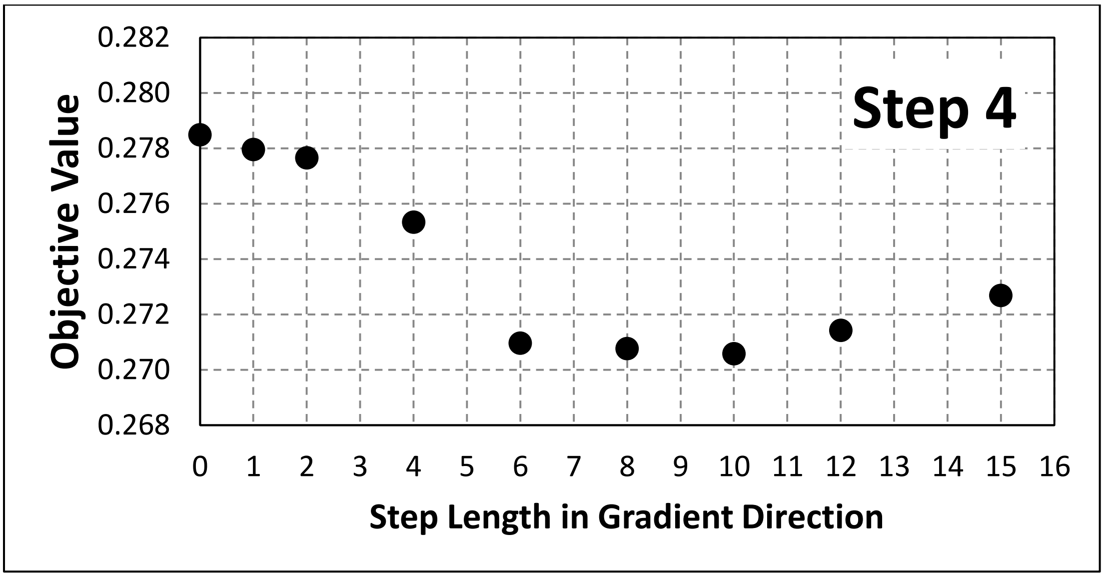


Figure A-3 Line Search in Gradient Direction for Optimization Step 4

The fifth optimization step is represented in Table A-4.

Table A-4 Gradient Vector Calculation for Optimization Step 5

| Optimization Step 5 | | | | | | | | | |
|---|---|---|---|---|---|---|---|---|---|
| | **Geo** | **Delta** | **$\Lambda_{LE}$** | **Ctip** | **b** | **RPM** | **$\Delta C_N$ (%)** | **OBJ** | **GRAD** |
| | **G4-S10** | | 0.248 | 0.717 | 0.800 | 541.2 | 1.94 | 0.27058 | |
| **$\Lambda_{LE}$** | **G5-P1** | 0.100 | 0.348 | 0.717 | 0.800 | 539.7 | 2.38 | 0.26985 | 0.000812 |
| **Ctip** | **G5-P2** | 0.030 | 0.248 | 0.747 | 0.800 | 540.9 | 3.21 | 0.27311 | -0.002833 |
| **b** | **G5-P3** | 0.030 | 0.248 | 0.717 | 0.830 | 504.9 | 4.40 | 0.26185 | 0.009780 |

The line search process in the fifth optimization is represented in Figure A-4.

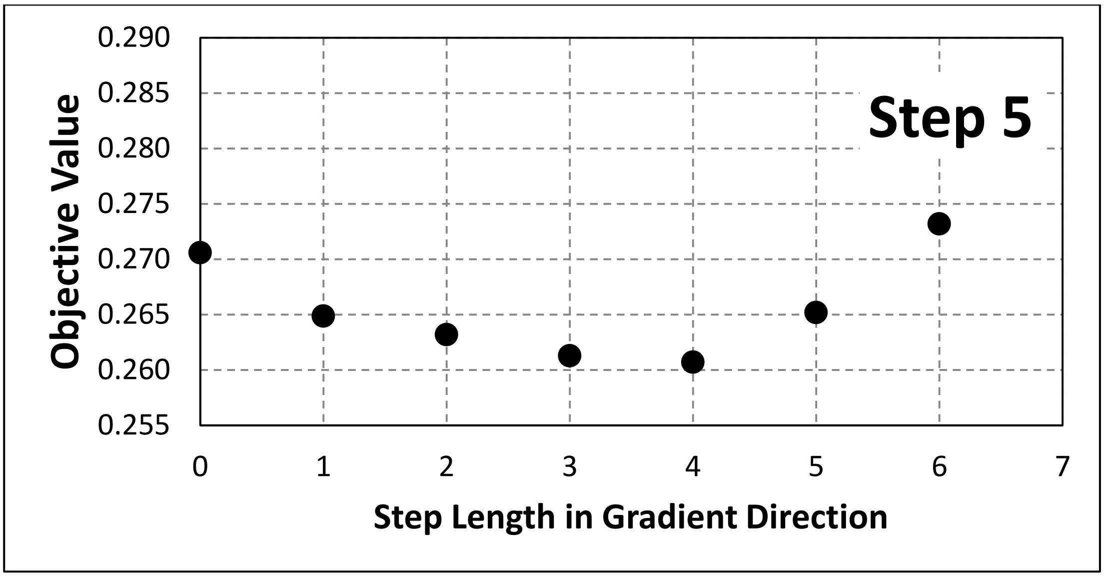


Figure A-4 Line Search in Gradient Direction for Optimization Step 5

The sixth optimization step is represented in Table A-5.

Table A-5 Gradient Vector Calculation for Optimization Step 6

| Optimization Step 6 | | | | | | | | | |
|---|---|---|---|---|---|---|---|---|---|
| | **Geo** | **Delta** | **$\Lambda_{LE}$** | **Ctip** | **b** | **RPM** | **$\Delta C_N$ (%)** | **OBJ** | **GRAD** |
| | **G5-S4** | | 0.259 | 0.706 | 0.840 | 494.7 | 4.08 | 0.26121 | |
| **$\Lambda_{LE}$** | **G6-P1** | 0.100 | 0.359 | 0.706 | 0.840 | 498.7 | 4.68 | 0.26134 | 0.010348 |
| **Ctip** | **G6-P2** | 0.030 | 0.259 | 0.736 | 0.840 | 494.7 | 5.72 | 0.27406 | -0.003900 |
| **b** | **G6-P3** | 0.030 | 0.259 | 0.706 | 0.870 | 464.9 | 6.16 | 0.26841 | 0.002431 |

The line search process in the sixth optimization is represented in Figure A-5.

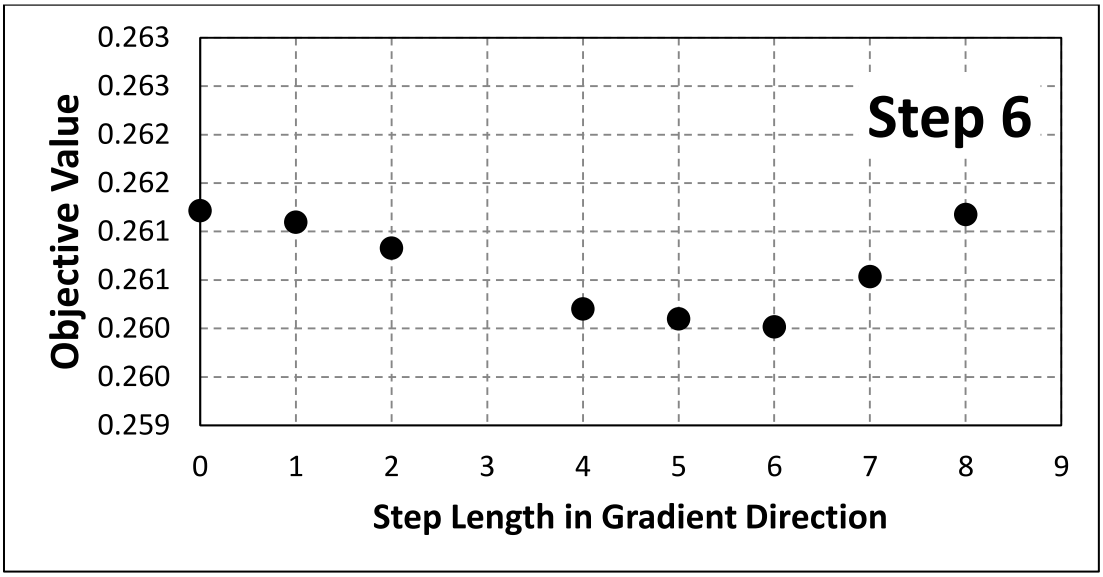


Figure A-5 Line Search in Gradient Direction for Optimization Step 6

# APPENDIX B

## USER-DEFINED-FUNCTION (UDF)

The User-Defined-Function (UDF) implemented to FLUENT for 1-DOF unsteady analyses is presented here. The mass and moment of inertia value of the tail fins are put into UDF. In order to give only roll rotation for free-to-rotate tail fins x-rotation is set to be FALSE and the others are set to be TRUE.

```
DEFINE_SDOF_PROPERTIES(ftr_tail, prop, dt, time, dtime)

prop[SDOF_MASS] = 0.100;

rop[SDOF_IXX] = 0.100;

prop[SDOF_IYY] = 0.100;

prop[SDOF_IZZ] = 0.100;

prop[SDOF_ZERO_TRANS_X] = TRUE;

prop[SDOF_ZERO_TRANS_Y] = TRUE;

prop[SDOF_ZERO_TRANS_Z] = TRUE;

prop[SDOF_ZERO_ROT_X] = FALSE;

prop[SDOF_ZERO_TRANS] = TRUE;

prop[SDOF_ZERO_TRANS] = TRUE;
```